2015

NANOINDENTATION OF A ZINC METAL SOAP MIXTURE FOR USE IN A LASER PRINTER

George A. Nimick
University of Kentucky, gnimick@hotmail.com

STUDENT AGREEMENT:

I represent that my thesis or dissertation and abstract are my original work. Proper attribution has been given to all outside sources. I understand that I am solely responsible for obtaining any needed copyright permissions. I have obtained needed written permission statement(s) from the owner(s) of each third-party copyrighted matter to be included in my work, allowing electronic distribution (if such use is not permitted by the fair use doctrine) which will be submitted to UKnowledge as Additional File.

I hereby grant to The University of Kentucky and its agents the irrevocable, non-exclusive, and royalty-free license to archive and make accessible my work in whole or in part in all forms of media, now or hereafter known. I agree that the document mentioned above may be made available immediately for worldwide access unless an embargo applies.

I retain all other ownership rights to the copyright of my work. I also retain the right to use in future works (such as articles or books) all or part of my work. I understand that I am free to register the copyright to my work.

REVIEW, APPROVAL AND ACCEPTANCE

The document mentioned above has been reviewed and accepted by the student's advisor, on behalf of the advisory committee, and by the Director of Graduate Studies (DGS), on behalf of the program; we verify that this is the final, approved version of the student's thesis including all changes required by the advisory committee. The undersigned agree to abide by the statements above.

George A. Nimick, Student

Dr. Fuqian Yang, Major Professor

Dr. Fuqian Yang, Director of Graduate Studies

NANOINDENTATION OF A ZINC METAL SOAP MIXTURE FOR USE IN A LASER PRINTER

THESIS

A thesis submitted in partial fulfillment of the
requirements for degree of Master of Science
in Materials Science and Engineering
in the College of Engineering
at the University of Kentucky

By

George Alexander Nimick

Lexington, Kentucky

Director: Dr. Fuqian Yang, Professor of Material Science and Engineering

Lexington, Kentucky

2015

ABSTRACT OF THESIS

NANOINDENTATION OF A ZINC METAL SOAP MIXTURE FOR USE IN A LASER PRINTER

At the start of this project, the possible choices of metal soaps had already been narrowed to include some of the zinc soaps used in this project. These zinc soaps are mixtures of zinc stearate and zinc palmitate of varying ratios purchased from a supplier. Zinc soap was chosen as result of its common use in various industries as a lubricant and mold release, which implied potential benefits in an electrophotographic printing system. These potential benefits include, but are not limited to, a more efficient transfer from a photoconductive drum and protection of the drum from mechanical and chemical degradation. Nanoindentation of these soaps was implemented in an effort to characterize each soap mixture and compare how the soap types differed from one another. Each sample was indented under a variety of different maximum loads and at different holding times to observe effects on the modulus, hardness, and, creep. The mechanical properties measured were then used to help distinguish differences between each type and provide an insight as to how or why one mixture may be preferable over another. The data could be utilized in conjunction with further testing to be used in a simulation of an interface of interest.

KEYWORDS: Zinc Stearate, Zinc Palmitate, nanohardness, zinc octadecanoate, zinc hexadecanoate

George Alexander Nimick

7/5/2015

NANOINDENTATION OF A ZINC METAL SOAP
MIXTURE FOR USE IN A LASER PRINTER

By

George Alexander Nimick

Dr. Fuqian Yang
Director of Thesis

Dr. Fuqian Yang
Co-Director of Graduate Studies
7/5/2015

I would like to dedicate this work to my family and friends and the “peanut gallery” at Lexmark. Thank you for all of your support.

ACKNOWLEDGMENTS

While the thesis herein was composed singularly, it was graced with the insights and guidance of many respected individuals. In regards to the primary direction of this thesis, I am indebted to Dr. Fuqian Yang and Dr. Bhaskar Gopalanarayanan who both convincingly encouraged the pursuit of this endeavor and consistently made themselves available for guidance throughout the project's duration allowing for a timely completion. Both advisors are resources of a great wealth of knowledge whose vastness I can only aspire to have one day.

I would like to thank the Thesis Committee, consisting of Dr. John Balk and Dr. Matthew Beck, for their flexibility, insights, and challenging questions that further broadened my perspective and challenged my thinking.

I am very grateful for the strong community at Lexmark International, Inc. and for their unparalleled support, especially Rick Hubert, Julie Jacobs, Jerry Fish, James Semler, Mike Lattuca, Matt Raszmann, Trey Gilliam, Kelly Killeen, Greg Selover, Jim Doeltz, Mary Kay, and others at Lexmark.

I am also very grateful for the support I had from my parents and fiancée, Brooke Kennedy, who consistently provided guidance and support throughout my academic career and helped during trying times.

TABLE OF CONTENTS

ACKNOWLEDGMENTS iii
LIST OF TABLES vi
LIST OF FIGURES vii
Chapter 1: Introduction and Overview 1
1.1 Introduction 1
1.2 Overview of the Thesis 4
Chapter 2: Review of Literature 5
2.1 Introduction 5
2.2 Metal Soaps and Zinc Stearate 5
2.3 Tribology 10
2.3.1 Lubrication 10
2.3.2 Friction 17
2.3.3 Wear 21
2.4 Contact Mechanics 26
2.5 Nanoindentation 34
2.5.1 Nanohardness 35
2.5.2 Contact Area and Indentation Tips 38
2.5.3 Load-Displacement Curves and Contact Stiffness 40
2.5.4 Influencing Factors and Other Considerations 42
2.5.4.1 Area Correction Due to Indenter Geometry 43
2.5.4.2 Thermal Drift 44
2.5.4.3 Other Influencing Factors 45
2.5.4.4 Other Considerations 46
2.6 Surface Measurements 46
2.6.1 Roughness Measurements 50
Chapter 3: Experimental Techniques 53
Chapter 4: Results and Conclusions 58
4.1 Results and Discussion 58
4.1.1 Liquid Chromatography Results 58
4.1.2 Nanoindentation Impressions 59
4.1.3 Force-Displacement Curves 60
4.1.4 Hardness and Combined Modulus 61
4.1.5 X-Ray Diffraction 75

4.2 Conclusions 78
Chapter 5: Future Work 84
Appendix I: Figures 87
Appendix II: Statistical Data 95
REFERENCES 108
VITA 113

LIST OF TABLES

Table 1: Test matrix for the nanoindentation of each zinc soap 57
Table 2: Zinc Stearate to Zinc Palmitate Ratios for Re-melted Samples 58
Table 3: Long spacing of samples using the peak near 6° 2θ as suggested by literature . 83

LIST OF FIGURES

Figure 1: TTT, CTT, TGT, and CGT molecular models where open circles are ascribed carbon or oxygen, and filled circles are hydrogen atoms. They have conformational disorder at the COO end 8
Figure 2: Crystal Structure Models of C16/C18FA-Zn. Weight ratios of Stearic acid in these models are 0%, 30%, 50%, 70%, and 100%. Dot-line circles mean void areas in these models. 9
Figure 3: Schematic representation of the fluid separating two surfaces 13
Figure 4: Mechanism of lubrication by lamellar solids 14
Figure 5: Schematic illustration of mechanisms of frictional energy dissipation..... 21
Figure 6: Long-range attractive forces and short-range repulsive forces acting on an atom or molecules within a liquid or solid. Atom "B" on the surface must move closer to atoms just beneath the surface so that the resulting short-range repulsive force balances the long-range attractions from atoms just beneath and further beneath the surface 28
Figure 7: Schematic of the forces between atoms in a solid as a function of distance away from the center of the atom. Repulsive force acts over a very short distance. Attractive forces between atoms act over a very long distance. An atom at infinity has a higher potential energy than one at the equilibrium position.... 29
Figure 8: Points on the indenter and specimen surfaces that have come into contact during loading. (a) full slip, (b) no slip, (c) partial slip (loading), (d) partial slip (unloading). In (d), reverse slip may occur, leading to residual stresses. 32
Figure 9: Indentation parameters for a) spherical, b) conical, c) Vickers, and d) Berkovich indenters (not to scale) 39
Figure 10: Various stylus types..... 48
Figure 11: Ra - arthimetical mean roughness according to ISO 4287 51
Figure 12: Representation of averaged depth of roughness parameter (Rz) definition according to DIN 4768..... 52
Figure 13: C-Laser DIC image of low force indents on the 56% stearate sample..... 59
Figure 14: C-Laser DIC image of high force indents on the 56% stearate sample 60
Figure 15: Force-displacement curves for the 95% zinc stearate sample at various holding times: (a) 20s, (b) 40s, (c) 100s, (d) 200s, (e) 400s 60
Figure 16: Variation of the reduced moduli with respect to maximum load and different holding times for indentations on a 95% zinc stearate sample. The error bars in the plot signify one standard deviation in either direction..... 64
Figure 17: Statistical contour plot showing the relationship between the maximum applied load and the holding time on the reduced modulus for the 95% zinc stearate sample 65
Figure 18: Variation of the hardness with respect to maximum load and different holding times for indentations on the 95% zinc stearate sample. The error bars in the plot signify one standard deviation in either direction..... 66

Figure 19: Statistical contour plot showing the relationship between the maximum applied load and the holding time on the hardness for the 95% zinc stearate sample. 66
Figure 20: Variation of the contact depth with respect to maximum load and different holding times for indentations on the 95% zinc stearate sample. The error bars in the plot signify one standard deviation in either direction..... 67
Figure 21: Statistical contour plot showing the relationship between the maximum applied load and the holding time on the contact depth for the 95% zinc stearate sample. 68
Figure 22: Statistical contour plot showing the relationship between the maximum applied load and the holding time on the contact depth for the 95% zinc stearate sample. 69
Figure 23: Statistical contour plot showing the relationship between the maximum applied load and the holding time on the contact depth for the 73% zinc stearate sample. 69
Figure 24: Statistical contour plot showing the relationship between the maximum applied load and the holding time on the contact depth for the 56% zinc stearate sample. 69
Figure 25: Statistical contour plot showing the relationship between the maximum applied load and the holding time on the contact depth for the 53% zinc stearate sample. 69
Figure 26: Statistical contour plot showing the relationship between the maximum applied load and the holding time on the reduced modulus for the 95% zinc stearate sample 70
Figure 27: Statistical contour plot showing the relationship between the maximum applied load and the holding time on the reduced modulus for the 73% zinc stearate sample 70
Figure 28: Statistical contour plot showing the relationship between the maximum applied load and the holding time on the reduced modulus for the 56% zinc stearate sample 71
Figure 29: Statistical contour plot showing the relationship between the maximum applied load and the holding time on the reduced modulus for the 53% zinc stearate sample 71
Figure 30: Statistical contour plot showing the relationship between the maximum applied load and the holding time on the hardness for the 95% zinc stearate sample. 72
Figure 31: Statistical contour plot showing the relationship between the maximum applied load and the holding time on the hardness for the 73% zinc stearate sample. 72
Figure 32: Statistical contour plot showing the relationship between the maximum applied load and the holding time on the hardness for the 56% zinc stearate sample. 72

Figure 33: Statistical contour plot showing the relationship between the maximum applied load and the holding time on the hardness for the 53% zinc stearate sample. 72
Figure 34: Modulus vs Max Force and Percent ZnSt 73
Figure 35: Modulus vs Holding Time and Percent ZnSt 73
Figure 36: Hardness vs Max Force and Percent ZnSt..... 73
Figure 37: Hardness vs Holding Time & Percent ZnSt 73
Figure 38: Contact Depth vs Max Force and Percent ZnSt 73
Figure 39: Contact Depth vs Holding Time and Percent ZnSt 73
Figure 40: Normalized XRD of all prepared samples 75
Figure 41: Zoomed in area of Figure 40 76
Figure 42: Comparison of the XRD of the as-received bar and the melted samples of 95% zinc stearate..... 77
Figure 43: Comparison of the XRD of the as-received bar and the melted samples of 73% zinc stearate..... 77

Chapter 1: Introduction and Overview

1.1 Introduction

Throughout the life of an electrophotographic imaging apparatus, several factors contribute to the degradation in imaging quality that include both mechanical and chemical deterioration. A common method for producing images in a laser printer is through the use of an electrically conductive cylinder with a photosensitive coating, commonly known as a photoconductor drum, in combination with a laser and toner. Component durability is often a challenge and one approach to reduce the wear of the photoconductor (PC) drum is to apply particulate masses of metal soap across its surface. These masses are deformed to produce a protective thin film on the PC drum surface in order to maintain the production of high quality images [1, 2]. Several critical interfaces exist that influence the formation of the thin film in this particular system. These include the applicator of the metal soap to the PC drum and the cleaning blade.

The primary objective of this work is to characterize some of the necessary material properties of metal soap mixtures for use in modeling one or more of these interfaces to simulate the interaction of the components in the formation and the maintenance of the protective thin film. The nip of the cleaner blade is considered to be the location of one of the greatest sources of mechanical wear in this particular system [2]. The nip of the cleaner blade is the interface between the active cleaner blade edge and the tangential surface of the PC drum and would be a strong candidate for an interface in which to model some of the interactions that occur.

For an electrophotographic system, the creation of ions is necessary to form a charged layer on the surface of the PC drum, which is critical to the image generation process. In a system where an alternating current (AC) voltage is superimposed on a direct current (DC) voltage and applied in the presence of a PC drum, a large concentration of ions are generated. Although this is necessary, the ions produced are corrosive to the polycarbonate surface of the PC drum and leads to its chemical degradation. According to Ricoh patent US 7383013B2, the chemical deterioration of the surface occurs even without the presence of any mechanical wear. The resulting degradation of the polycarbonate surface occurs as a result of ozone, active oxygen and the bombardment of ions on the surface. This leaves the surface displaying evidence of molecular chain cleavage, which also results in a lesser degree of chain entanglement. The applied thin film reduces the chemical deterioration of the polycarbonate by acting as a barrier against the factors that affect its chemical degradation [2].

Additionally, the PC drum endures a large amount of mechanical wear at the cleaner blade nip. This is not solely a result of the contact of the cleaner blade itself with the PC drum, but in conjunction with the particles that are present at the nip that act abrasively [3]. Several types of particles are present at the nip; the most predominant being toner and its "extra particulate additives" (EPAs). The EPAs typically consist of silica particles ranging in size with the largest typically being approximately 0.1 microns. However, even if 100% of the toner was transferred off of the PC drum surface, the additives would still remain in conjunction with other particles, such as paper dust and carrier particles, and would need to be removed as well [4]. Thus, a mechanical removal system, such as the cleaning blade, is necessary.

In addition to removing particles, the blade is typically used to also “refresh” the surface of the photoconductor drum by continually removing small amounts of the surface as it also becomes chemically degraded [3]. However, with the application of a thin film, the need to abrade the polycarbonate surface of the drum diminishes. Both the PC drum and the cleaner blade are abraded throughout their lifespan. As the cleaner blade is abraded, it cleans less and less effectively, which results in the degradation of the image quality [3]. The application of a thin film of metal soap assists the cleaning mechanism by lubricating the surface of the drum to permit more efficient transfer and to provide a physical barrier between the PC drum and the afore mentioned factors to reduce the amount of wear at the interface. The chemical degradation that typically occurs on the drum surface will then occur on this sacrificial film, which can be sheared and actively replenished [2].

The application of the metal soap is expected to reduce the friction between the PC drum surface and the blade and extend both of their lifespans without impeding the designed print quality. A metal soap was chosen for the application because it fits the criteria as a remedial solution since, according to literature, they are widely known as lubricants and can be solidified to any form or shape to meet space and life requirements among many other properties [5-7]. The objective is therefore, to analyze some of material properties of a specific type of metal soap that consists of zinc stearate and zinc palmitate and analyze the potential differences caused by using different ratios of zinc stearate to zinc palmitate and discuss in a bit more depth its role and importance in the system by way of focusing on specific influential aspects of the system.

1.2 Overview of the Thesis

The following chapters provide background regarding the experimental techniques used, the experimental approach taken and the results that were encountered. Chapter 2 provides a literature review of metal soaps, solid lubricants in general, and highlights of tribology. Additionally, the nanoindentation technique will be described in regards to an overview of the contact mechanics and the extraction of some of the material properties. Chapter 4 subsequently contains the results from nanoindentations performed on various zinc soap mixtures, of which the experimental techniques are discussed in Chapter 3. Finally, in Chapter 5, recommendations for future work are made and how they would be useful in this endeavor.

Chapter 2: Review of Literature

2.1 Introduction

This chapter provides a general overview regarding the topics of metal soaps, solid lubricants, tribology and nanoindentation to provide background and insight to their relevance and importance to the experiments performed by the author that are herein discussed.

2.2 Metal Soaps and Zinc Stearate

Metal soaps are used and found in a variety of conditions. The necessary components are found naturally and can react together to spontaneously form or can be synthesized. Metal soaps are salts that are formed from non-alkali metals of differing valences and a carboxylic acid with an aliphatic tail, or fatty acid [8, 9]. “Traditional” soaps that are used for cleansing are water-soluble surfactants contain a metal cation from the alkali metals group, typically potassium or sodium. These differ in behavior from what is typically classified as a metal soap in that metal soaps are not water-soluble and have popular uses in many applications, most of which are industrial [8]. Since metal soaps are insoluble in water, they have been used as a waterproofing agent by many industries, such as in the construction industry for roads, buildings and the manufacturing of construction materials, as well as by paint, pharmaceutical and textile industries to prevent the

absorption of humidity or moisture in general [8]. However, due to the properties of metal soaps, they have been used for a wide variety of applications beyond their hydrophobic nature. They have been found to be exceptional mold release agents, especially for plastics and rubbers, as well as good lubricants in general. Not only are they used as lubricants in their solitary state, but can be combined with oils to form greases as a result of their ability to thicken certain substances. This property has been used to thicken certain paints and cosmetics, and to form ointments, plasters, and gels. They have also been used as a siccative for paints and inks to promote drying, curing and/or hardening. Small amounts have also been combined with "traditional" soaps to enhance their germicidal and antiseptic nature. This is not to be considered an exhaustive list, as many other uses have been found [8-16].

Fats and oils that are derived from plants and animals are common sources from which the necessary fatty acids are obtained. These fatty acids include, but are not limited to, stearic, palmitic, oleic, linoelic, and ricinoleic acids. As a result, this has been known to cause the formation of soaps naturally or unintentionally. For instance, in artwork that contains non-precious metal "leafs," or paint films contain metal and oil, ionic metal compounds and fatty acid compounds react to form a metal soap spontaneously through an ion exchange, or saponification[8, 10]. Common metals soaps include those containing calcium, zinc, magnesium, copper, and aluminum. Of greatest interest in this paper are the metal soaps of zinc stearate and zinc palmitate. Stearic and palmitic acids are most commonly retrieved from the natural sources of tallow, lard and palm oil [8, 14]. As Gönen et al described in their paper, there are three primary methods in which metal soaps such as these are formed. These include 1) a precipitation process through double

decomposition, 2) a fusion process that involves the direct reaction of carboxylic acid with metal oxides, hydroxides, and carbonates or 3) a direct reaction of metals with molten fatty acids. An example of each reaction is found below. In an industrial setting, the first two methods are typically preferred since, in general, pure metals are not naturally found [9, 15].

$$2C_{17}H_{35}COONa_{(aq)} + ZnSO_4 \cdot 7H_2O_{(aq)} \rightarrow (C_{17}H_{35}COO)_2Zn_{(s)} + Na_2SO_{4(aq)} + 7H_2O_{(l)} \quad (1)$$

$$Zn + 2C_{17}H_{35}COOH_{(l)} \rightarrow (C_{17}H_{35}COO)_2Zn_{(l)} + H_2O_{(g)} \quad (2)$$

$$Zn_{(s)} + 2C_{17}H_{35}COOH_{(l)} \rightarrow (C_{17}H_{35}COO)_2Zn_{(l)} + H_{2(g)} \quad (3)$$

Zinc stearate and zinc palmitate are similar in some regards, in that their aliphatic chains only differ by two methylene groups, with zinc stearate being the larger of the two. Thus, their chemical formulas are $Zn(C_{18}H_{35}O_2)_2$ and $Zn(C_{16}H_{31}O_2)_2$ for zinc stearate and zinc palmitate respectively. This can also be generalized for all of the zinc soaps as $Zn(C_nH_{2n+1}COO)_2$ where n=11, 13, 15, 17, etc. Studies of zinc stearate and zinc palmitate have demonstrated that zinc stearate and zinc palmitate have a natural tendency to crystallize independently and when mixed with each other [17]. This has been visually observed by Sawada and Konaka upon their use of a jet mixing variant of the fusion process to precipitate particles of the soaps. The soaps were observed to be flake-like shaped with relatively high circularity that was maintained as the particles grew in size [17]. Their crystallinity was confirmed through X-ray diffraction by Sawada and Konaka [17]. Barman et al, used the Fourier transform of infrared spectroscopy (FTIR) to obtain

information regarding the conformations and subcell packing of the chains at various temperatures [12]. Other authors have also performed these tests and obtained similar results on these soaps and others that were formed in synthesis processes. These studies have also agreed that the zinc stearate and zinc palmitate form a tetrahedral crystal structure in reference to the location of the zinc atoms [16].

Stearic and palmitic acids are naturally saturated and linear acids. However, as shown by Ishioka, the configuration of the carboxylic group in its bonding to zinc governs the shape of the zinc soap molecule. Zinc stearate and palmitate are typically in an all-trans configuration, which eases the crystallization process, however, it can also be found in one of the forms below which consist of a combination of a trans, gauche and cis configuration, where C=cis, G=gauche and T=trans and the TTT configuration is the all-trans case [18].

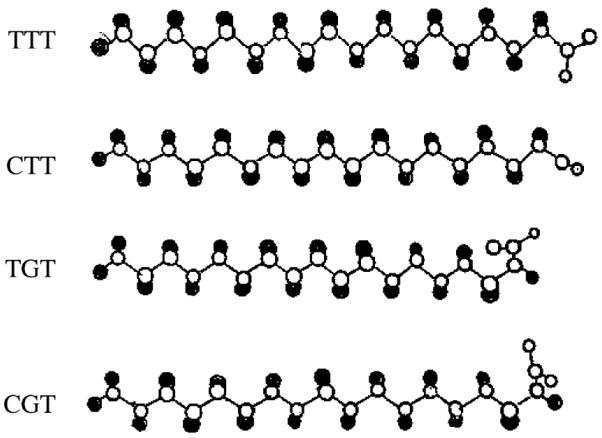

Figure 1: TTT, CTT, TGT, and CGT molecular models where open circles are ascribed carbon or oxygen, and filled circles are hydrogen atoms. They have conformational disorder at the COO end [18].

Furthermore, it has been claimed by Sawada based on gas sorption and XRD data that when zinc stearate and zinc palmitate are combined, their crystal structure remains the

same and only the long spacing changes as a result of the differing chain lengths. As a result, the zinc atoms maintain their general lattice positions and variably-sized voids are created between the chain pairs that are shorter than the longest, most predominant chain pair, depending on the mix ratio of stearate and palmitate soaps [17].

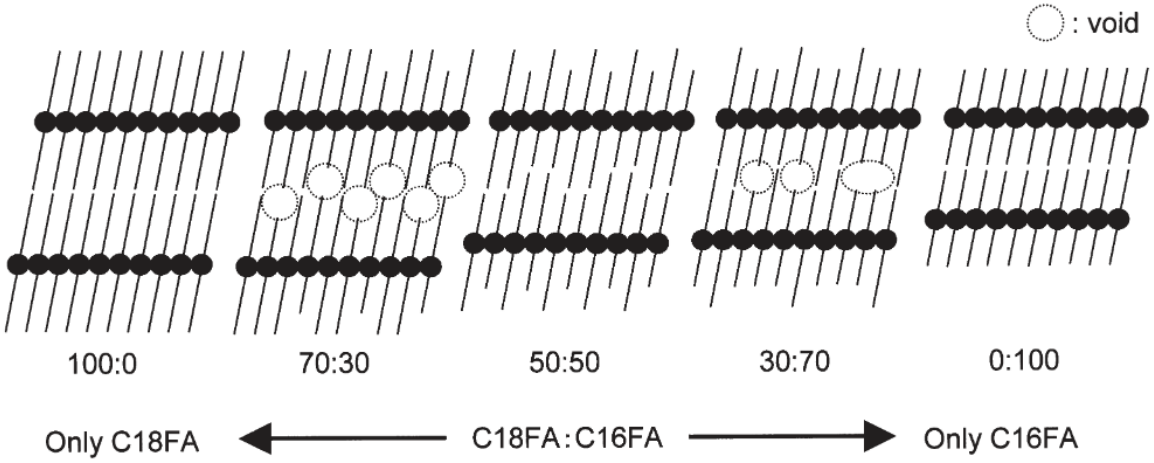

Figure 2: Crystal Structure Models of C16/C18FA-Zn. Weight ratios of Stearic acid in these models are 0%, 30%, 50%, 70%, and 100%. Dot-line circles mean void areas in these models [17].

The combination of zinc stearate and zinc palmitate are of interest in this paper because they have been chosen to be incorporated a laser imaging apparatus as a lubricant and barrier. The zinc soap mixture is widely known as a lamellar solid as can be noted by its frequent use as a lubricant and its many claims in various solid lubricant books and literature. This is likely a result of its crystallographic nature and the type of crystal structure that it forms. The crystallographic nature lends itself to be anisotropic in that it shears easily along the plane between fatty acid chains and does not easily shear perpendicular to the plane of zinc atoms. Thus, this paper seeks to identify possible differences in the mechanical properties between mixtures of various ratios of stearate and palmitate.

2.3 Tribology

The word tribology is derived from the Greek “tribos,” which is translated as sliding or rubbing. Thus, tribology is the study of friction, wear and lubrication [19].

2.3.1 Lubrication

Lubricants are available in a plethora of forms and material properties and, depending on the application, it can be quite a challenge to find or develop a lubricant that satisfies all of one’s needs. Their fundamental purpose is to control friction and wear in a system and as a result their quality is critical as it can determine their performance through life; from the moment of initial application to its desired end. Lubricants are commonly recognized as oils and greases, but can also be in solid form. The choice of lubricant is often guided by the constraints of the application, which is why the material properties of both solid bodies in contact, as well as the lubricant, are crucial in controlling wear [19].

Since the primary type of lubricant had already been chosen for the system at the time that this project had begun, the focus of this paper will not be to validate the choice of lubricant, but to highlight some aspects that typically govern the choice of a lubricant and how they pertain to the lubricant chosen. This includes highlighting and examining the ratios of the two-part metal soap composition.

The lubricant that was selected for this system is a solid lubricant rather than a fluid lubricant. Solid lubricants can be advantageous to certain systems, such as this one,

because of their “cleanliness” and their robustness in comparison to non-solid lubricants, such as oils and greases. Liquid lubricants are often messy in the sense that they can drip or be slung off of the area of interest fairly readily. Additionally, the coefficients of friction that result with the use of a solid lubricant are more stable across a wider range of temperatures and environments when compared with these other lubricant types. However, issues with solid lubricants can involve their limited lifespan, replenishment issues and degradation due to oxidation or aging. Additionally, they are generally poor thermal conductors and do not easily dissipate heat from the interface [6, 19].

Although the use of solid lubricants is primarily a result of their durability and their performance capabilities in cases where traditional lubricants cannot perform, the modern trend has increased their use to minimize the amount of liquid lubricants used, primarily because of environmental concerns. However, currently, there is not a single lubricant that can minimize friction and wear over a range of uses, temperatures or conditions. [6, 7].

Solid lubricants can be classified in numerous ways depending upon what is desired from a lubricant and by the limitations of the system. Most generally, they are classified by whether their structure is lamellar or non-lamellar, but they can also be categorized based on their composition and structures. Examples would be lamellar, soft metals, oxides (mixed or single), carbon-based, organic/polymers, and mixtures [19].

Two key considerations when choosing any type of lubricant is the relative speed of the contact surfaces and the temperature at which the lubricant is expected to operate at. For a liquid lubricant, these have a significant effect on its viscosity. Lubricants with a high viscosity often create thicker films, which results in greater separation between the

contacting surfaces. However, the greater the viscosity, the greater the resulting power losses are. This is a result of the increased amount of energy required to shear it, which also signifies that more heat is generated and subsequently resulting in an increase in the temperature of the contacting bodies. The temperature change can also influence the lubricant's viscosity by reducing the viscosity and thus its ability to properly lubricate. This is more problematic with the use of oils since their viscosity can reduce by approximately 80% with a temperature change of only 25°C. A solid lubricant is typically more stable than an oil under a wide range of conditions, which is why solid lubricants are chosen over fluids for certain applications, including the application at hand [19].

The dynamic or shear viscosity of a lubricant is essentially its resistance to shear flow and is represented as η. The dynamic viscosity can be found by separating two, flat parallel surfaces with a film of thickness h and applying a force, F, to the upper surface. The amount of force required is impacted by the amount of surface area, A, in contact with the film and the velocity gradient through the film. The value of η is in essence the proportionality constant relating the shear stress to the shear rate and can be expressed as shown below:

$$F = \eta A \frac{\partial u}{\partial h} \tag{4}$$

Rearranging:

$$\eta = \frac{F}{A} / \frac{\partial u}{\partial h} = \tau / \frac{\partial u}{\partial h} \tag{5}$$

where τ is the shear stress acting on the lubricant and $\frac{\partial u}{\partial h}$ is the shear rate, or velocity gradient. The kinematic viscosity, v, is a ratio of the dynamic viscosity and the lubricant density, ρ [20].

$$v = \frac{\eta}{\rho} \qquad (6)$$

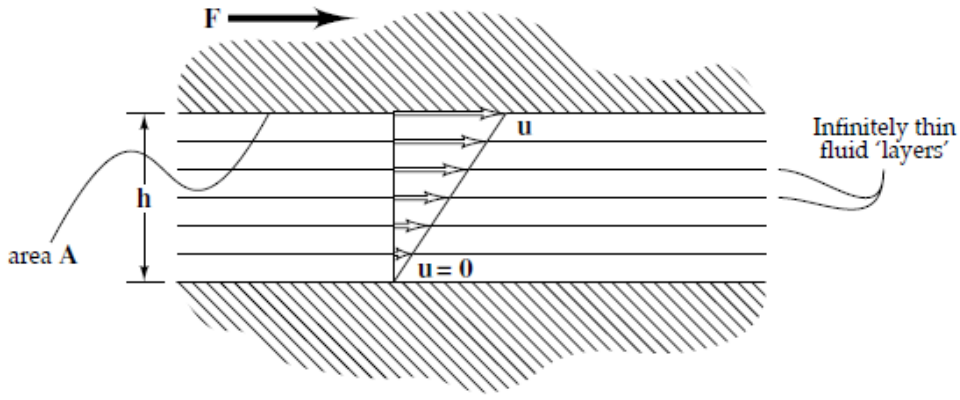

Figure 3: Schematic representation of the fluid separating two surfaces [19].

The mechanism of adhesive wear is fairly common in contacting bodies and is reliant mostly on the adhesion between the bodies and the shear strength parallel to the contact surface. This mechanism is actually exploited in some solid lubricants. Some solids, namely lamellar solids, exhibit anisotropy of their mechanical properties and have a low shear stress along a particular direction or crystallographic plane. The atoms or molecules that lie in the same plane, or lamella, are packed closely together and strongly bonded. The spacing between planes, or lamellae, however, is relatively far apart and the interaction between the paired chains is also relatively weak. Therefore, a lower shear force is required for forces parallel to these planes rather than perpendicular cleavage of layers. Although the continuous shearing of layers of a lubricant is readily visualized by

the concept of the laminar flow of a fluid, this is also somewhat representative of the nature of a lamellar solid in that there is assumed to be a no-slip boundary condition at the interface with the contact surfaces and a shear rate gradient through the lubricant's thickness. Metal soaps, such as the zinc soap mixture of interest, are lamellar solids that behave in this manner [5, 19].

Additionally, strong adhesion between the lubricant and the contact surfaces is greatly desired, as well as a strong tolerance against chemical decomposition or degradation under the desired operating conditions.. Metal soaps, however, do not readily oxidize due to their chemical structure and are primarily dependent on the nature of the shear planes to lubricate effectively.

Through electron diffraction, studies have demonstrated that lamellar solids tend to form preferentially oriented layers such that the lamellae lie parallel to the direction of motion causing low friction [5, 12]. Each lamella can be composed of a single plane one atom thick or several atoms thick, but metal soaps have an aliphatic tail and therfore each lamella consists of several atoms. The strong inter-atomic bonding and packing of a layer is essential for minimizing wear as it provides the large in-plane strength, which is characteristic of the plane of zinc atoms [5, 7, 19].

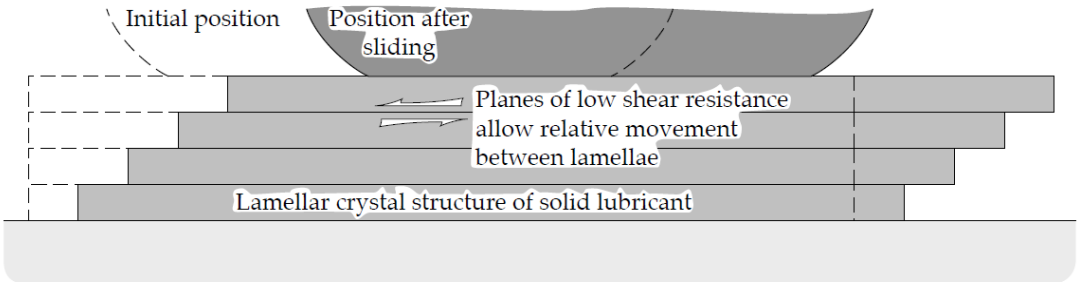

Figure 4: Mechanism of lubrication by lamellar solids [19].

Solid lubricants, and lubricants in general, fill the troughs separating asperities on the same surface and between the contacting surfaces to create a boundary layer or film that separates the two bodies that would otherwise be in contact. Additionally, the “run-in” practice, (discussed in the wear section), facilitates the lubrication of the film by reducing the height of the asperities that the film has to overcome. The strong adhesion to the contact surface and the compliance of the film to the surface contours helps to prevent it from getting pushed out of the interface during extreme pressures.

The deposition or formation of the films can also be critical for a lubricant to be effective. This primarily pertains to the necessary means to ensure proper adhesion of the lubricant to the contact surface. Assuming that the proper adhesion of the lubricant to the surface is not a concern, the studies performed by Deacon and Goodman demonstrated that the application method was not critical when comparing prior lamellae orientation through rubbing or brushing. Eventually, both cases will quickly result in preferential orientation of the lamellae and similar frictions. Solid lubricants can be applied in a variety of methods, including but not exclusively, through sprinkling, brushing, rubbing, burnishing, impregnating, vapor deposition, or through a carrier such as aerosol. The system of interest uses a brush applicator to apply the zinc soap to the PC drum [5, 7, 19, 21].

Plastic deformation of the contact surfaces is still possible even with little to no contact between surfaces. Deacon and Goodman observed instances that indicated that the lubricant successfully distanced the contact surfaces, but transmitted enough pressure to deform the substrate’s prior abrasion lines. This was observed mostly with relatively thin

lubrication films with large applied loads, while the thicker films were thought to be able to disperse the pressure over a larger area resulting in only elastic deformation [5].

Some advantages of solid lubricants are that they are well suited for high load applications. Solid lubricants do not have the tendency to be forced out of the contact interface like fluid lubricants. Additionally, since solid lubricants function by the shearing of the solid, the contact load can facilitate the shearing of the lubricant if the shear strength is not adversely impacted by the normal load. Solid lubricants are also well suited for low speed applications where contact surfaces often penetrate fluid films. As mentioned previously, temperature has a much smaller effect on solids lubricants than non-solid lubricants in that the non-solid ones tend to change viscosity and film thickness very quickly with changes in temperature. In dirty or abrasive environments fluids or greases have a higher propensity of picking up and retaining particles than solid lubricants, which results in abrasive wear. Since solid lubricants do not flow like fluid ones, they are more suitable for intermittent use or with periods of extended storage. Solid lubricants are often lighter weight in comparison to a fluid sump, though replenishment with a solid lubricant can be more of a concern. The zinc soaps being utilized are electrically insulating, which helps specifically in maintaining the ability to retain charge on the surface for printing purposes.

2.3.2 Friction

The phenomenon of friction is generally defined as being the resistance of motion between two objects in contact with one another or the increase in force that assists in inducing and/or maintaining their motion [22, 23]. The topic of friction has been a topic of interest for over hundreds of years, both in the effort to exploit is as well as reduce it [24, 25].

Friction is generally independent of the speed of the motion between objects, as a first order approximation when examining a system at the macroscopic level. It can also be noted that neither the apparent contact area nor velocity appears as a variable in the Amontons' Law relationship, $F_f = \mu L$. This simplified relationship is reasonable provided that there is a moderate load and moderate speed. [19].

Every surface has some degree of roughness and, as a result, the apparent contact area is orders of magnitude larger than the actual contact between the two or more objects. [25]

Today, friction is still an area of interest in the development of emerging products and technologies, especially as it pertains to the extreme ends of the size scales [24]. Friction is utilized frequently every day; most obviously in the brakes of automobiles, in the ability to walk and grasp objects, and in the playing of string musical instruments. Friction can also have undesirable effects in some applications because of the wear that is induced and the energy that is consumed. In this particular instance, the detrimental effects of friction are the ones of interest as they have negative impacts on the components and the quality of the end product.

Friction is typically categorized into static and kinetic friction. As the names imply, static friction is the related to both the resistance and initiation of relative motion between two bodies in contact, whereas kinetic friction pertains to the resistance that occurs between two bodies in continued relative motion or the maintenance of that motion [26]. Static friction is generally greater than kinetic friction and can be thought of as the part of the "activation energy" to permit relative motion between two objects in contact. To some degree the resistive nature of friction is a matter of perspective or application. In regards to sliding, friction would appear to be resistive in nature. However, in regards to a roller imparting rotational motion on another roller, it is through friction that this is possible.

Depending upon the focal point of interest, friction and its effects can be observed on the macroscopic scale or the microscopic scale. For many applications, friction is examined at the macroscopic scale and, therefore, it is typically assumed that the resulting friction processes in the contact area are isotropic and homogeneous in the contact region. These assumptions are generally acceptable since the details of the microscopic interactions do not greatly affect the behavior of the bulk material, depending upon the scale of the objects [23].

When examining a system macroscopically, the energy "losses" that are experienced due to friction are considered to be a conversion from bulk translational energy into thermal energy, with the assumption that there is no wear. The heat is then conducted into the bulk material and can result in an increase in temperature of the surfaces. It is critical to be mindful of this because it can result in phase changes or chemical changes of the surfaces or lubricant film, which can significantly change their behaviors [19]. The

frictional work performed is given by the following relationship, which is essentially Amontons' Law multiplied by the velocity [23].

Examining the contact on a more microscopic level, it can be seen that the actual contact area, is much smaller than what appears to be the contact area macroscopically. Rather than the normal and frictional forces being evenly distributed across the apparent area, they are concentrated at the points that are in contact with one another. This, of course, is due to the inherent roughness of all surfaces and the material properties of the surfaces. Since frictional energy is concentrated at these asperities, this implies the frictional energy is dissipated at these points and, therefore, these asperities experience much higher temperatures than predicted with the simplified contact theory. This is important because of the surface changes that can be induced in the material [19, 23].

Not only is the geometric ‘fitting” and contact of the asperities important, when examining objects in contact at the microscopic level. The attractive force can also be quantified and become critical when considering adhesive contacts. This is especially the case as it pertains to extremely smooth surfaces, soft contact bodies, and/or microscopic systems, such as between a smooth and flexible cleaning blade against a polycarbonate surface in the system at hand [25].

In many cases, the adhesive forces are negligible as a result of the inherent roughness of most surfaces and since there generally is not full contact between the two bodies, the force of adhesion is less than those governing the motion between the bodies. However, in some cases, such as when a smooth body comes into contact with a rough and rigid body, the adhesive force becomes appreciable. Considering such a case, the body will elastically deform to fill in the troughs of the surface roughness.

This is an event that has been macroscopically observed with the cleaner blade and the PC drum surface. Without the presence of a substance or medium between the two working surfaces the edge of the cleaning blade will typically adhere to the surface of the PC drum as the drum rotates. However, if a lubricating medium such as a metal soap is placed in the contact interface, this creates a separation of the two surfaces and allows for relative motion due to the low shear planes.

2.3.3 Wear

Wear and friction are very interrelated and their desired effect on the system can either be proportional or inversely proportional, depending upon the application. For instance, in a polishing or grinding application, both friction and wear are desired. However, in the case of pencil lead, wear is desired, but with minimal friction. For a braking application, the reverse is true; wear is ideally minimized, but not friction [19]. In many cases, including the present one of interest, wear and friction are undesirable and are considered to be one of the major causes of waste and performance loss for this and many other systems [19, 27].

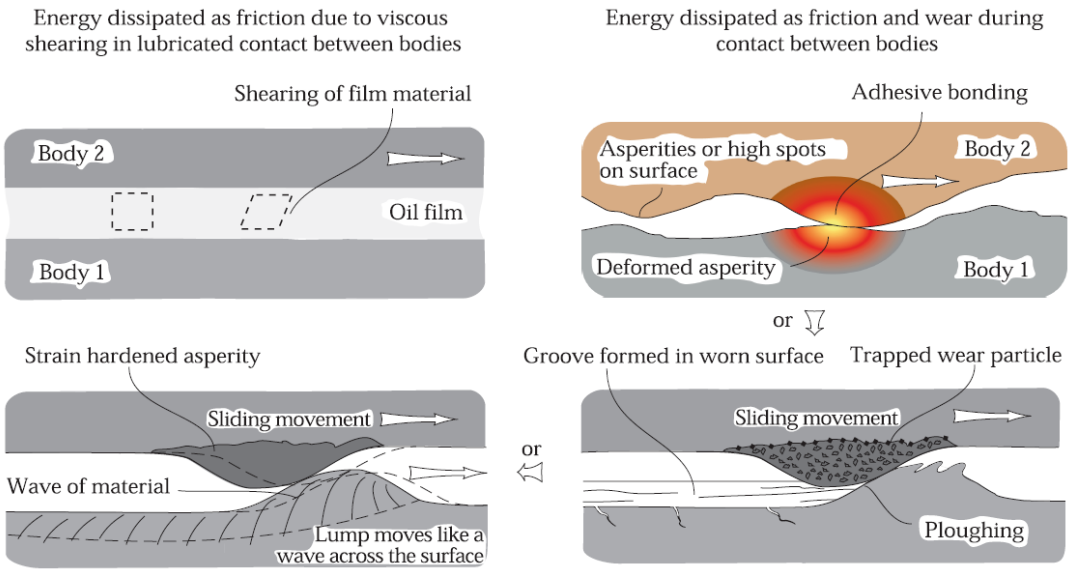

Figure 5: Schematic illustration of mechanisms of frictional energy dissipation [19]

Several mechanisms of wear exist and can be generally categorized into four primary mechanisms of wear that include adhesion, abrasion, fatigue, and chemical. These are all

forms of wear that can occur in this subsystem of the printer and minimized through the use of a metal soap thin film.

Wear due to adhesion usually involves the contact of a few asperities and then an increase in the amount of true contact area as relative motion continues between the two surfaces. Of course, fundamentally, this is a result of the forces of attraction between the atoms in contact, but is also largely influenced by the material selection. A soft material is more likely to comply about the surface features of the interfacing surface due to the nature of its low elastic modulus. As a result, the total adhesion between the two contact surfaces is greater because the attractive forces act on a larger area. This can also occur for stiff materials if the applied load is great enough. The surface asperities for stiff materials are likely to deform under high loads, which enables more contact between the two materials increasing the adhesion. Adhesion can also result in plastic deformation of components while the surfaces are in relative motion with each other. The use of a lubricant, such as a metal soap, at the contact interface is often employed in creating a boundary and to minimize adhesion between the contact surfaces. [19, 28].

'Fatigue wear' generally occurs in an event when the lubricant supplied is only partially effective (i.e. the lubricating film it too thin), and the wear that occurs is generally mild as a result of only partial contact between asperities. As these asperities are exposed to repetitive stresses, such as through impact, bending, or rolling, they experience fatigue and result in creep, surface cracking, or even cracking of the subsurface. For such cases, materials with an adequate fatigue strength and toughness should be utilized [19, 28].

In some instances, particles become trapped in the troughs between asperities, either in the presence or absence of a lubricating film, and can rapidly result in 'abrasive wear' of

one or both interfaces resulting from the grinding or pitting from the abrasive material. Furthermore, the material removed from the contacting surfaces by the abrasive particles can accumulate and become abrasive debris themselves. It is desirable that the contact surface(s) be at least as hard as the abrasive material(s). In general, it is advisable to choose materials with a high yield strength and high fracture toughness to prevent cracks due to fracture or fatigue, but usually a compromise is necessary. Erosion from particles impact is also prominent. For low angle particle impacts, hard and brittle materials are typically suitable, but with impact from high angle particles, great fracture toughness and ductility are more desirable [19, 28].

Surfaces can also be influenced by chemical attack either due to the nature of the bodies in contact or the environment in which the system operates, as in the environment that the PC drum experiences. This is known as ‘corrosive wear’ or ‘oxidative wear’ depending on the chemical nature of the attack on the surface and usually is strongly dependent of the chemical potential of the surface or portions of the surface. Surface defects or impurities, especially in metals, can exacerbate this issue. There are many other types of wear that are not discussed here since the presence of wear will occur with nearly all types of contact between solid bodies. These are some select mechanisms of wear which are desired to be controlled in this system through the use of a zinc metal soap [19].

Certain measures can be taken to prepare contact surfaces for longer lifespans. Sometimes surfaces are “run-in” or “broken-in” by sliding contacting surfaces past each other at light loads to remove the peaks of the asperities or flattening them to smooth the surface. This reduces the coefficient of friction between the surfaces to one that would be

seen in a long-term steady state condition. This can then be combined with a lubricant to further reduce the friction [19].

Material selection or design is critical to the minimization of wear and the general function of parts. It is best to identify the type of potential wear that surfaces of interest would experience so that materials can be chosen accordingly. Of course, it is always best to create a design that minimizes factors that affect wear, but wear some degree of wear is often unavoidable. In industrial situations material selection can often be a difficult task because of the complexity of the system(s) and of all factors that need to be accounted for, including ancillary factors, which can limit the selection. Although material selection is often done empirically, a more systematic approach can reduce time and cost by narrowing the possibilities and reducing the chance of overlooking any obvious factors.

In relatively simple cases, wear resistance can be achieved through the choice of a bulk material. However, surface treatments are often chosen due to their versatility and due to the complexity of systems. A surface treatment can be applied to nearly any material, but the material selection of the coating and its deposition are critical. Surface treatments can be in the form of a coating or an actual "treatment." In both cases of surface materials and bulk materials, material structure, performance, processing and properties all play a crucial role in the characteristics of the material selected. Of course, ancillary factors, such as availability, chemical compatibility, ability to surface finish if required and operating environments also need to be taken into account when choosing a material [28].

A large result of friction is the heat generated which can have a great effect on the friction and wear of the surface. Since the majority of the heat generated from dry contact is conducted through the asperities of the contacting surfaces and since the true contact area is orders of magnitude smaller than the apparent contact area, the heat becomes concentrated at these points. This is also exacerbated if the contact surfaces are poor thermal conductors. Despite extreme conditions, the temperatures generated typically cannot exceed the melting temperature of the bodies. The thermal mounds that result, however, can have significant increases in temperature that can modify the material properties of the surface by modifying the surface microstructuremodification of films, "frictional welding," volatilization, decomposition, or initiation of chemical reactions. Even if melting does not occur, the heat generated can supply enough energy for surface recrystallization to take place by supplying enough energy to promote atomic or molecular mobility so that the atoms or molecules can arrange themselves into larger crystals [19, 21, 23].

2.4 Contact Mechanics

With advancements of industry and manufacturing capabilities, namely the railroad at the time, interest grew regarding the calculation of exact stress values due to the extreme contact stresses that rail wheels and axles often experience and the proximity of these stress values to the yield stress of the steel used. As a result, several contact theories arose and have continued to be developed. In 1882, Heinrich Hertz pioneered the analysis of the contact between two solids. In an effort to derive some relationships, he examined the normal contact between curved bodies each with a different radius of curvature. Several theories were made subsequent to Hertz's theory to improve it and to be more applicable to practical scenarios. Greenwood and Williamson, in 1966, developed a contact theory that described rough surfaces using spherical bumps with equal radii of curvature with asperities that varied according to a Gaussian distribution. It can be noted that that this parallels Hertz's theory when examining the contact between asperities, but expands the nature of the analysis to a greater level in trying to more accurately predict the relationship between the true area of contact and load on a large scale through a more detailed analysis using the inclusion of small scale features. Bridging to the above sections, it was mentioned that every surface has some degree of surface texture/roughness. This perspective is critical because of the importance of being able to accurately and quickly determine the real contact area for a given situation, which is useful for properties such as electrical resistivity at an interface, heat transfer, friction, seals, etc. This is especially important in regards to the work performed as it pertains to

the nanoindentations as well as aspects of the system interfaces that are of interest [25, 29, 30].

Using Hertz's contact theory, the contact area is predicted to vary non-linearly as a function of compressive force where the area could be approximated with the following relationship:[31]

$$A \sim F_N^{\frac{2}{3}} \quad (7)$$

This, however, disagreed with experimental results for randomly rough surfaces where the true contact area is much smaller than the apparent contact area. The experimental results indicated that the relationship between the true contact area and the compressive load is linear. This also supports the basis for Hooke's Law, which will be discussed later. This relationship was also confirmed by Bush, Gibson and Thomas, as well as Persson who utilized Hertz's contact theory, but used different methods for approximating the surface asperities and height distributions to more accurately calculate the real contact area [29, 31].

Although, the above theories demonstrate improvements and adjustments to the Hertzian contact theory, only the fundamentals of his theory will be discussed, since many of the other theories utilize his as a basis [29].

Prior to discussing Hertz's contact theory, a slightly more in-depth view of normal contact will be discussed involving elastic and inelastic deformations at the atomic level. In connection with the previous section on friction and wear in regards to contact at the atomic level, it reasonable to assume that the modulus and strength of a body or material would be dependent upon the nature and strength of the chemical bonds that make it up.

Atoms in a solid experience both attractive and repulsive forces with respect to each other.

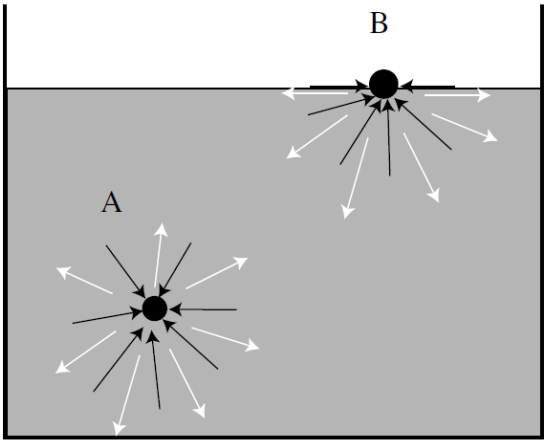

Figure 6: Long-range attractive forces and short-range repulsive forces acting on an atom or molecules within a liquid or solid. Atom "B" on the surface must move closer to atoms just beneath the surface so that the resulting short-range repulsive force balances the long-range attractions from atoms just beneath and further beneath the surface [32].

The repulsive forces are a result of short-range Coulombic forces whereas the long-rang forces are a result of chemical bonds due to the filling or sharing of electron shells and the tendency to be in a lower energy state. A curve of this attraction/repulsion relationship with respect to distance can be seen in a generic curve in Figure 7; of course the actual shape of the curve is dependent upon the actual bond type. However, as can be seen from the curve, there is a near linear relationship between the distance between atoms and the force required to separate or compress atoms together for small displacements. This force-displacement curve, specifically the segment from equilibrium to the maximum force, can be approximated with a portion of a sine function in which the following relationship can be established: [32]

$$F = F_{max} \sin\left(\frac{\pi x}{2L}\right) \qquad (8)$$

where L is the distance from the equilibrium position at the maximum force, or cohesive strength when one single atom is pulled away from another. Using the small angle approximation and considering the maximum force to be constant for a particular material, this can be simplified to

$$F = F_{max}\left(\frac{\pi x}{2L}\right) = \left[\frac{F_{max}\pi}{2L}\right]x = kx \qquad (9)$$

which takes the form of Hooke's Law. This then can be rearranged into the form of stress and strain and modulus. However, as a result of crystallographic defects that commonly appear, materials do not exhibit these theoretical values in their bulk form and actual values are experimentally obtained. With these values, quantities such as strain potential energy can be calculated [32].

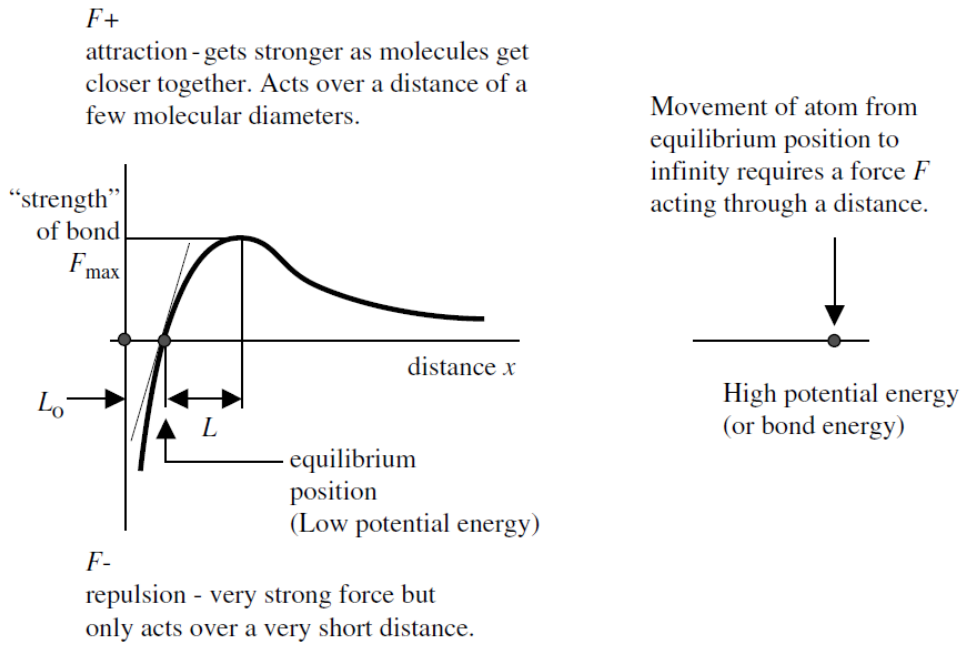

Figure 7: Schematic of the forces between atoms in a solid as a function of distance away from the center of the atom. Repulsive force acts over a very short distance. Attractive forces between atoms act over a very long distance. An atom at infinity has a higher potential energy than one at the equilibrium position. [32]

Scaling this concept back to a more macroscopic perspective, there will be a resultant displacement as a result of an applied load on a body or, in this case, a contact between two bodies. This displacement can be elastic or inelastic depending on the applied load and the strength of the material. Thus, there are two primary relationships of interest that are desired to be satisfied by contact theories which are the force-displacement relationships and the force-contact stress relationship. Continuing with Hertz's contact theory, the assumptions he made upon founding his theory are summarized as follows:

- The surfaces of the contacting bodies are continuous and smooth.
- The bodies are in frictionless and non-adhesive contact and, therefore, only normal pressures are transmitted between the bodies in contact.
- The resulting contact area is small in comparison to the radii of the contacting bodies and, therefore, the strains are small and the surfaces are considered non-conforming. This allows for each surface to be treated as an elastic half-space
- The governing differential equations for the bodies in static equilibrium should agree with the stresses and strains in the bodies. The stresses should approach zero at a large distance from the contact area.
- Integrating the pressure distribution in the contact area is equal to the magnitude of the load acting on the two bodies.

Additionally, it assumed in classical contact mechanics that the materials are isotropic and homogeneous. Using these assumptions, Hertz studied the contact between elastic solids and approximated their surface profiles in the vicinity of contact with quadratic functions. This was an approximation for surfaces with continuous curvature and can, therefore, be changed to something more suitable of the actual contact profile. For a

spherical body indenting a flat surface, he found a relationship between the elastic properties of the contacting bodies, the radius of the contacting body, R, and the applied load, P, to be:

$$a^3 = \frac{3}{4}\frac{PR}{E^*} \quad (10)$$

where a is the radius of contact and E^* is the combined modulus of the contacting materials, or the reduced modulus.

When calculating the stresses that result from contact, Hertz estimated the stresses through a body by calculating the stresses along the surface and axis of symmetry and then interpolating between them. Boussinesq then followed this analysis characterizing the stress fields for point contacts. The analysis of stress fields in elastic-plastic contacts becomes even more complicated as a result of the plastic deformation of both the yielding and the cracking effect [32].

Although friction is neglected for many cases and may be an acceptable assumption, it is still important to understand the role of friction in a contact problem, apart from what has been noted in the section above. In a frictionless case, portions of both contacting bodies are compressed into their respective bodies and points on the surface and within the bodies are permitted to move with respect to each other resulting in internal forces/stresses. However, with the inclusion of a friction condition, incidents of no slip and partial slip occur that influence the behavior of contact. One case is the complete opposite of the frictionless condition in which there is a complete adhesion contact, or no slip. In this case, the points in contact are prevented from moving with respect to each

other as a result of the frictional forces. The alternative cases would then be cases of a partial slip condition that occurs in the loading or unloading case. In these cases, the applied load will cause some points in contact to overcome the frictional force and slip past each other while other points remain adhered to one another. Similarly, this also occurs during unloading. As the applied load is reduced, forces are balanced by internal forces, the applied load and friction. As the applied load is further reduced, a point is reached where the internal stresses overcome the friction at some contact points and allows for slip to occur at these points.

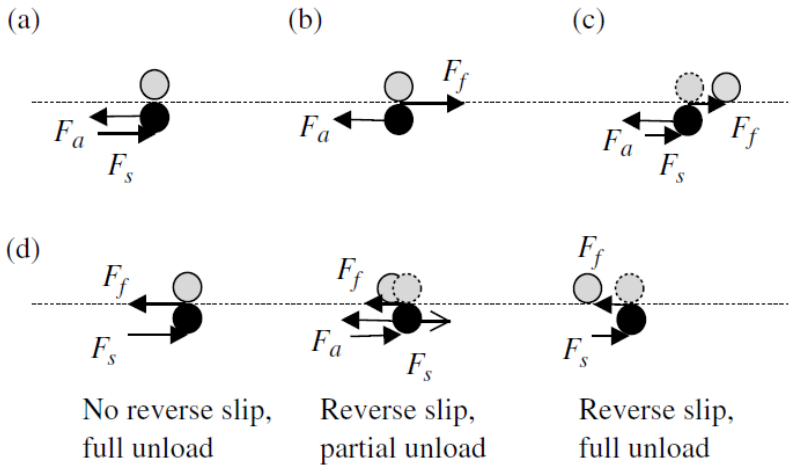

Figure 8: Points on the indenter and specimen surfaces that have come into contact during loading. (a) full slip, (b) no slip, (c) partial slip (loading), (d) partial slip (unloading). In (d), reverse slip may occur, leading to residual stresses. [32]

The contact mechanics described are applicable in both cases of interest as it pertains to the application of a zinc mixture soap and the characterization of its mechanical properties. The application of the metal soap involves the creation of stress fields in itself if we examine the deformation of a particle by the force of an elastomeric blade. If the adhesive force of the particle is greater than that imparted on it by the blade, the particle

will remain on the surface of the PCD and undergo shearing and compression. A large portion of the particle will be sheared off since it cannot fit beneath the blade and the remainder that was adhered to the drum will be compressed as a result of the blade force in the contact area of the blade nip.

2.5 Nanoindentation

As alluded to above, Hertzian contact mechanics is pertinent to finding mechanical properties of materials such as modulus and hardness of a material and is often employed through the use of an indentation test on a material as a result of its speed and simplicity. In the early 1900's, Brinell performed some of the first indentation tests in an attempt to characterize the plastic properties of materials. Soon after, this was adopted by many industries and a variety of different indentation techniques emerged. Indentation tests can now be in a macro-, micro-, and nanoindentation form. Initially, hardness measurements utilized optical imaging to determine the hardness of a material by examining the plastic deformation and the size and shape of the imprint caused by the indenter. However, in the 1970's, it was recognized that the elastic modulus of a material could be acquired from the load displacement curve, which encouraged the development of equipment that can continuously measure the load and displacement of the indenter [32, 33].

The development of the nanoindenter came from the desire to measure the mechanical properties of thin films and surface treatments which microhardness instruments were not capable of. The microindenters are not capable of applying a low enough force that could indent the material without having a measurement that was influenced by the substrate beneath the sample surface. The nanoindentation technique is a very useful one in this regard and a useful technique for measuring mechanical properties in general. It is able to measure loads on the order of nanonewtons and displacements of approximately 0.1nm. This allows for the measurements of very thin films and layers of films, which cannot be

performed by other indentation methods. The nanoindentation instruments are also fairly simple to use and are not costly to run, unlike some characterization equipment.

As mentioned in part above, the primary purpose for using a nanoindenter is to quantify some of the mechanical properties of a material, a small volume of a material or superficial layer of a material. The most common properties that are measured in this fashion are modulus and hardness, though these can only be measured if some information is known about the material and the indenter [32].

2.5.1 Nanohardness

Measurements that are of critical importance in regards to finding these material properties, as well as others, are the displacement of the indenter tip with respect to the sample and the contact area. Using these measurements, Hertzian contact theory can be used to find the properties of interest, most directly in the case of a spherical indenter. As seen in the contact mechanics section, Equation (10) demonstrates the relationship that Hertz encountered between the contact radius, the indenter load and the elasticity of the contact. This is useful in conjunction with the mean contact pressure which is defined as

$$p_m = \frac{P}{\pi a^2} \qquad (11)$$

where P is the normal load and a is the radius of the contact circle. When combined with Equation (10), the mean contact pressure can be re-expressed as follows:

$$p_m = \frac{P}{\pi a^2} = \left(\frac{4E^*}{3\pi}\right)\frac{a}{R} \quad (12)$$

where E^* is a combination of the modulus of the indenter and the sample. As might be suspected, the mean contact pressure if commonly called the 'indentation stress' and the term, $\frac{a}{R}$, is the 'indentation strain'. This alludes to the Hooke's Law stress-strain relationship that is commonly acquired from typical uniaxial compression and tension tests. As a result of how the stress fields in an indentation are confined, the mean contact pressure that is exerted is greater than what is necessary to initiate yielding in a traditional uniaxial test and more readily produces plastic flow as a result of shear stress and the large hydrostatic component.

The mean contact pressure is utilized to find the hardness, H, of a material at the point where its mean contact pressure is constant and the applied load, P, is at a maximum. Thus, this is expressed as:

$$H = \frac{P}{A} \quad (13)$$

where A is the projected area of contact. This measurement of hardness is performed these conditions in an effort to perform a measurement where there is a fully developed plastic zone. The standard definition of hardness for nanoindentation is the Meyer hardness. The Brinell hardness number (BHN) gives a value of hardness based upon the actual area of contact rather than the projected area. This allows for a measurement that is independent of the load and only influenced by the material response.

The hardness of a material also relates to the yield strength of a material through the following approximation

$$H \approx CY \tag{14}$$

where Y is the yield stress of the material and C is the constraint factor that is dependent upon experimental parameters, such as the indenter and specimen types. Relationships have then been seen between the ratio of the material's elastic modulus and yield stress, $\frac{E}{Y}$, in relation to the constraint factor. For instance, materials with a large ratio, such as metals, tend to have a constraint factor of about 3, whereas materials with a low ratio, such as glasses, tend to have a C value of about 1.5 [32].

The condition of full plasticity in the area of consideration is critical in the hardness measurement of a material. Erroneous values of hardness are commonly reported from cases in which full plasticity has not yet developed, which essentially signifies that only the mean contact pressure was measured, since the value was not independent of the applied load. This is best exemplified by the indentation of a very elastic material, such as a rubber specimen. Most of the resulting deformation during an indentation would be elastic and very little plastic deformation, if any would occur. As a result, the mean contact pressure, or the apparent hardness, would be low and representative of the material's resistance to elastic and plastic deformations. However, as a result of the material's high resistance to plastic deformation, the true hardness is actually very high. The true hardness of a material is its resistance to plastic deformation with little to no elastic deformation or, in other words, the energy, U_p, required to plastically deform the indentation volume of material, V.

$$H = \frac{U_p}{V} \quad (15)$$

This can be derived by using the power law form of the load-displacement curve with the assumptions that the displacement of the residual impression is equal to the maximum displacement of the indenter and that the reduced modulus is infinite. This can then be integrated to find the work done on the system. Without showing the derivation, a general representation of the energy required to indent a material for an elastic-plastic case is:

$$U_p = \left(\frac{1}{3}\sqrt{\frac{1}{\pi \tan^2 \alpha}}\right)\frac{1}{\sqrt{H}}P^{3/2} \quad (16)$$

where α is the effective cone semi-angle [32].

2.5.2 Contact Area and Indentation Tips

In order to accurately determine the true hardness value of a material, the area of contact must be known or able to be determined. Rather than using optical techniques to measure the residual impression created by the indenter, the nanoindenter, records the penetration depth and determines the projected the area of the indentation based on the geometry of the indenter and a calibration that is performed. The projected contact area is a direct result of the geometry of the indentation tip that is chosen.

Various indentation tips exist that are utilized for various purposes and vary from sharp to blunt. The most common types of tips used are spherical and pyramidal indenters. In

regards to the pyramidal indenters, the Vickers and the Berkovich tips are the most widely used [34].

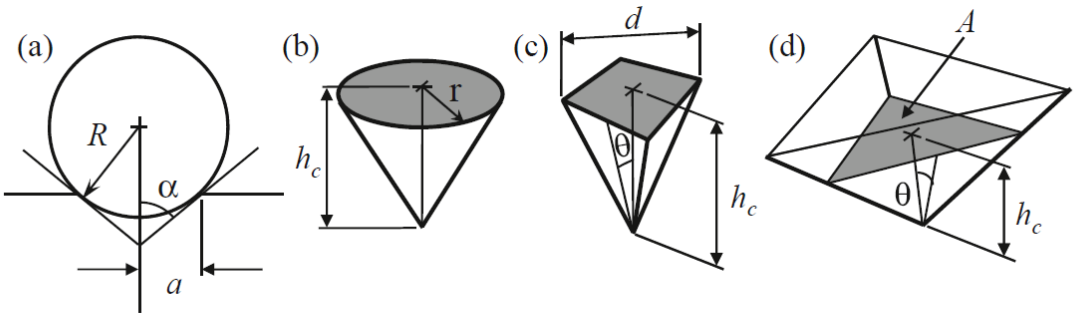

Figure 9: Indentation parameters for a) spherical, b) conical, c) Vickers, and d) Berkovich indenters (not to scale) [34]

Due to their geometry, spherical indenters are directly applicable to the equations presented in the Hertzian contact theory and smoothly transition from elastic to elastic-plastic deformation during the indentation. This geometry is best for soft specimens. One thing to note is that the radius of contact increases more quickly than the indentation depth as the load of the indenter is increased. It is important to recall that when measuring hardness, a fully developed plastic region is required for an accurate measurement, which should be kept in mind when using this tip since it is more likely to remain in the elastic regime [34].

The Berkovich indenter is the most commonly used pyramidal indenter and was the one used in this investigation. It is a three-sided pyramidal indenter tip which has the inherent advantage of being able easily get the three sides to meet at a point. The Vickers indenter is also a pyramidal indenter, but instead has four sides, which is more likely to have a line at the tip rather than a point. The geometry of the original Berkovich tip was such that it had the same actual contact area as the Vickers indenter, but it was changed so that the

face angle is 65.27° giving it the same projected area as the Vickers indenter since the mean contact pressure is used to find hardness, which is a function of the projected contact area [34].

For simplicity, pyramidal indenters are often treated as conical indenters in regards to the calculations performed as a result of the axis-symmetry of conical indenters and more simple nature of their representative equations. Equivalent cone angles are found for conical representation of a pyramidal indenter to exhibit the same projected area as a function of depth.

The projected contact area of the Berkovich indenter is given by:

$$A = 3\sqrt{3}h_c^2 \tan^2\theta \quad (17)$$

where h_c is the contact depth and θ is the face angle of the indenter. Since the face angle is 65.27°, as previously mentioned, the projected contact area is

$$A = 24.494h_c^2 \approx 24.5h_c^2 \quad (18)$$

Equating this to the projected contact area of a conical indenter,

$$A = \pi h_c^2 \tan^2\alpha \quad (19)$$

the effective cone semi-angle, α, can therefore be found to be 70.3° [34].

2.5.3 Load-Displacement Curves and Contact Stiffness

The sequence of a nanoindentation typically involves the approach of an indenter tip to the sample surface, a ramp to a specified load or displacement, a holding period, and an unloading ramp back to zero, all while recording the force and penetration of the indenter. Especially with the use of a sharp pyramidal tip, such as the Berkovich tip, the loading portion of the load-displacement curve takes shape as the specimen undergoes elastic-plastic deformation. What occurs in the holding time that follows is partially influenced by the operator who specifies the duration of the holding time and whether the load or displacement is held at a constant value. During this period creep or relaxation in a material can be observed by recording the changes that occur during this segment. Following the holding period, unloading of the specimen occurs. It was observed by Doerner and Nix that the initial portion of the unloading curve was linear for a wide range of different materials. This is a result of the sample and indenter maintaining contact as the indenter slowly retracts, but maintaining the same contact area. As the contact area decreases, the unloading curve deviates from its linearity and becomes curved [34].

The slope of the linear portion of this segment therefore represents the linear elastic portion of the contact and is, therefore, representative of the contact stiffness, $\frac{dP}{dh}$.

$$\frac{dP}{dh} = 2h_c E^* \sqrt{\frac{24.5}{\pi}} \qquad (20)$$

where E^* is combined elastic modulus of the indenter and specimen and h_c is the contact depth that represents the distance from the contact circle to the point of maximum penetration. The latter value can be found by indentifying the point at which the linear portion of the unloading curve would intercept the displacement axis [34].

The importance of the contact stiffness is that a close approximation of the elastic modulus of the material can be extracted. The contact stiffness provides a value of the reduced, or combined, modulus through the rearrangement of Equation (20). If the poission ratio of the specimen is known, then the elastic modulus of the specimen can then be computed through the following relationship.

$$\frac{1}{E^*} = \frac{(1-v^2)}{E} + \frac{1-v'^2}{E'} \qquad (21)$$

The prime terms indicate the poisson ratio, v', and elastic modulus, E', of the sample and the un-primed terms are those of the indenter [34].

The general method used to find the contact stiffness is the multiple-point unload method. The multiple-point unload method uses the slope tangent to the initial portion of the unloading curve to calculate the contact stiffness by fitting a tangent line to several of the initial unload points. This implies that this slope will not only be influenced by the reduced modulus, but also by the creep and hardness of the material, to some degree. This method is commonly used, especially when Berkovich indenter tips are used [34].

2.5.4 Influencing Factors and Other Considerations

As a result of the inherent scale of nanoindentation, the measurements that are taken through nanoindentation are only surface measurements and need to be treated accordingly before generalizing the results for the entire material or assuming that the behavior of the bulk material behaves in the same manner. Bulk materials often contain

defects that affect its strength and, additionally, depending upon the processing of the material, there could exist a large difference in properties between the outer layer and inner layers(s) in the material. The results from a test can also be influenced by factors, such as dislocations, grain sizes, voids and other near surface defects [34].

2.5.4.1 Area Correction Due to Indenter Geometry

Other factors can also influence the accuracy of the measurements taken such as the indenter geometry. The indenter geometry is assumed to be ideal, but is rarely ever so. As a result, a correction factor is applied which is determined by either a direct method or indirect method of measuring the geometry of the actual indenter. The indenter can either be measured directly via methods, such as atomic force microscopy (AFM) or with scanning electron microscopy (SEM), however it is more common and practical to measure the indenter geometry indirectly by indenting a reference specimen whose elastic modulus and poisson ratio are known. The reference indentations then provide a reduced modulus which can then be used to find the actual projected area from

$$A = \pi \left[\frac{dP}{dh}\frac{1}{2\beta E^*}\right]^2 \quad (22)$$

where β is the geometry correction factor, which is 1.034 for the Berkovich tip. This would then be applied as a ratio with respect to the ideal projected contact area, A_i, to the equation for hardness and reduced modulus to find their respective corrected values [34].

$$H = \frac{P}{A}\left[\frac{A_i}{A}\right] \quad (23)$$

$$E^* = \frac{dP}{dh}\frac{\sqrt{\pi}}{2\beta\sqrt{A}}\sqrt{\frac{A_i}{A}} \quad (24)$$

An indenter with a tip radius that is larger than the ideal tip radius would have ratio of $\frac{A_i}{A}$ greater than one and a smaller tip radius would have a ratio less than one. Although the area correction can be expressed in many forms, it is often represented as a series in the following form

$$A = C_1 h_c^2 + C_2 h_c + C_3 h_c^{1/2} + C_4 h_c^{1/4} + \cdots \quad (25)$$

The first term of the expression presents the ideal area function followed by the correction terms. The deviation of the indenter geometry is more critical for shallow indentation depths and lessens as the penetration depth increases [34].

2.5.4.2 Thermal Drift

Thermal drift is also an influencing factor to the measurements taken. Thermal changes of both the sample and the indenter can cause expansion or contraction in the materials which skews the measurement of the penetration depth of the indenter in the sample. According to a study by Feng and Ngan, the effects of thermal drift on the calculation of the modulus is negligible if

$$t_h \approx \frac{S}{|\dot{P}|} h_c \quad (26)$$

where t_h is the cumulative time from the beginning of the test to the start of unloading, S is the contact stiffness, and $\dot{P}$, is the unloading rate. To correct for this, a low load indent is performed on the sample and maintained at that load to determine the thermal drift. A low load is chosen to minimize the influence of creep in the sample with the thermal drift. A drift rate is then determined and applied to indentation measurement [34, 35].

2.5.4.3 Other Influencing Factors

There are several factors that can affect the data recorded by a nanoindentation instrument, which include the occurrence of material pile-up or sink-in, surface roughness, and rounding of the indenter tip. Other forms of error exist, but these are the most prominent. Depending upon the behavior of the material during indentation sink-in or pile-up of the material can occur. The behavior depends upon the ratio of the elastic modulus and the yield strength, E/Y. If the ratio is high, pile up is likely to occur for a strain hardening material, and if the ratio is low for either a strain-hardening or non-strain-hardening material, sinking-in is more likely. Surface roughness and tip rounding logically play an important role in the measurement of the mechanical properties of the material as both influence the actual contact areas. The surface roughness of a material can effectively increase the contact area between the indenter and the sample, which effectively decreases the measured values, i.e. reduced modulus, etc. The rounding of the indenter tip can influence the indentation results, specifically hardness, of shallow measurements that are on the order of 50nm by reducing its ability to create a fully

developed plastic zone. This will therefore include elastic contact making the measurement more indicative of the mean contact pressure [34].

2.5.4.4 Other Considerations

Nanoindentation can also be used to examine other properties of samples and materials. It can facilitate the estimation of the fracture toughness of materials at a small scale, including on thin films, through the utilization of tips that create high stress concentrations in the contact area. The cube corner indenter, which is three-sided pyramidal indenter, is recommended for estimating the fracture toughness of a material because it is capable of displacing three times as much material as a Berkovich indenter while using the same applied force, due to its geometry. The holding period of a sample can be used to measure the creep or relaxation of a material by maintaining a constant load or strain for a specified holding time. Additionally, if a nanoindenter is equipped with a tangential force sensor, nanoscratch, topography, wear, and friction measurements can be acquired [33, 34].

2.6 Surface Measurements

As alluded to in the tribology and nanoindentation sections, the characteristics of a surface are of great importance in many applications, especially in much of today's technology. One surface characteristic that has been of interest for quite some time for

various reasons is that of surface metrology. Relating to the topics discussed thus far, surface roughness is an important parameter as it pertains to friction and contact mechanics, in that it can give an indication of the true contact area with respect to the apparent contact area and the amount of interlocking between two surfaces. In regards to wear, if the surface topography is measured prior to use and after use, the measurements can be compared to examine the level of wear that occurred and any subsequent patterns that may be apparent.

Surface topography can be measured on a variety of scales and subsequently at different speeds. Prior to the development of modern equipment, the examination of surface finishes was done by "eye" and "thumbnail" and compared against reference surface finishes. This was useful to some degree, but, of course, qualitative. In an effort to gather quantitative measurements that were less subjective, devices were created that measured surfaces through two primary means that mimicked those previously mentioned; either optically or via a stylus. These emerged to keep up with the demands of industry especially in the mass production of optical and machined components [36].

The stylus method was developed soonest and essentially involved the tracing of a stylus across a surface while recording the stylus' movement. In the early twentieth century, two individuals created profilometers that were designed very similarly. The designs included a pivoting arm to which a stylus was attached. On the top of the cantilever, opposite the stylus, was a small mirror. As the stage that carried the sample moved, cantilever with the stylus would, as well, based on the surface features of the sample. This, in effect, caused the mirror to translate. An optical system focused a beam of light on the mirror which would then reflect the light onto photographic paper so that the

movement of the stylus could be recorded. This was the basic design of Gustav Schmalz and was the first commercial profilometer. Dr. P. Tomlinson's was similar, but varied in that it was purely mechanical and it recorded the translated motion of the tip onto smoked glass. There were several issues that arose from this method, as could be expected with the first iteration of any development. Improvements to this technique were developed through the years by various people. These modifications included the oscillation of the tip in order to prevent its bending due to collisions with large surface features [36-39].

Other stylus profilometers are caliper-like in that there are two arms. One arm touches a reference surface and the other touches the sample surface. For some of these instruments, the reference surface is the same as the sample surface with one arm that has a blunt stylus that acts as a mechanical filter and the other arm a sharp stylus that measures the surface features. The stylus for these instruments is generally a sharp, diamond-tipped stylus such that the tip is unlikely to get damaged or deformed. Unfortunately, one disadvantage to these profilometers is that because of the sharp stylus, it is prone to leaving tracks in the surface of the sample, especially those of soft materials. Another disadvantage is that the speed of measurement is limited by the speed of the stylus across the surface of the sample, which is restrictive so that the stylus does not skip over any surface features [37, 40].

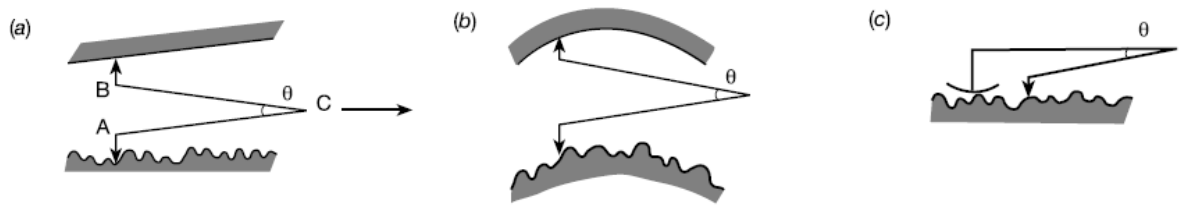

Figure 10: Various stylus types [38]

To overcome some of the issues with contact based profilometry, some non-contact instruments were developed. One such instrument was based off of the scanning probe microscope, which functions based on the field emission current generated between the sharp tip of an electrically conductive probe and an electrically conductive surface based upon their relative separation. This was in conjunction with a control and feedback loop to control the position of the probe. Following advancements with the scanning tunneling microscope (STM) emerged another system for profilometry called the atomic force microscope (AFM). This technique can measure the surface properties of both conductive and non-conductive with extremely high resolution by scanning an "ultra-small probe tip" across the surface and measuring the forces exerted on the tip [38].

The modern AFM is capable of three primary mode variants: contact mode, non-contact mode and tapping mode. Put simplistically, the AFM operates somewhat similarly to Schamlz's profiler using a cantilever, a sharp tip and a relative motion between the sample and tip. The AFM uses a laser beam and diodes to detect the motion of the cantilever/tip. The attractive and repulsive forces are used to govern the motion of the tip. In contact mode, this is the primary signal of measurement, but for the tapping and non-contact modes, the forces are used in the feedback loop to control the tip's proximity to the surface of the sample. AFM's are generally small and can easily be placed on a desktop, but they can also range in sizes large enough to measure large silcon wafers. Most AFM's can only measure an area of about 100 square micrometers. Variants of the AFM allow for other properties to be measured, such as capillary effects, surface chemistry, surface charge, magnetic forces and more [39].

Optical profilometers also measure a sample's surface without contact and can do so rapidly. For this project, a confocal laser scanning microscope (CLSM) was also used to capture images of the indents on the surfaces and to measure the topography of the surfaces in regards to surface roughness. The CLSM focuses a laser beam onto an area of interest on a specimen. A spatial filter, typically consisting of a set of variably-sized pinholes oriented spirographically about an axis on a plate, filters any scattered light from above and below the focal plane of interest. The specimen is scanned vertically in a controlled manner and the maximum intensities for each height are compiled 'tomographic-like' to construct a three-dimensional representation of the specimen surface. Depending upon the capabilities of the microscope, the sample could also be scanned in the *x* and *y* directions and stitched together. The information collected about the topography can then be used to calculate surface roughness parameters that characterize the size of the samples that was imaged. Various improvements and configurations exist depending upon the commercial unit. These typically involve ways to reduce noise in the measurement such as by optimizing mirror reflectivity and placing the laser more distant from sources of vibration and transmitting the laser beam by fiber optic. This method is fairly advantageous due to the speed in which surface measurements can be acquired in comparison to other profilometry methods and due to the fact that it is non-destructive [41-43].

2.6.1 Roughness Measurements

Particular aspects of a surface's topography are important depending upon the application. Therefore, a series of standard roughness values were devised to summarize

and standardize the topographical information of a sample's surface. The arithmetic roughness value, or R_a, is by far the most commonly used and is an arithmetic average of the deviations in height about a center line within a certain evaluation length, see Equation (27). One issue is that surfaces can have considerably different topography, yet have the same R_a value. Despite this, it can be useful to obtain a rough order of magnitude of the roughness and can be combined with other roughness parameters [44].

$$R_a = \frac{1}{lr}\int_0^{lr} |Z(x)|\, dx \qquad (27)$$

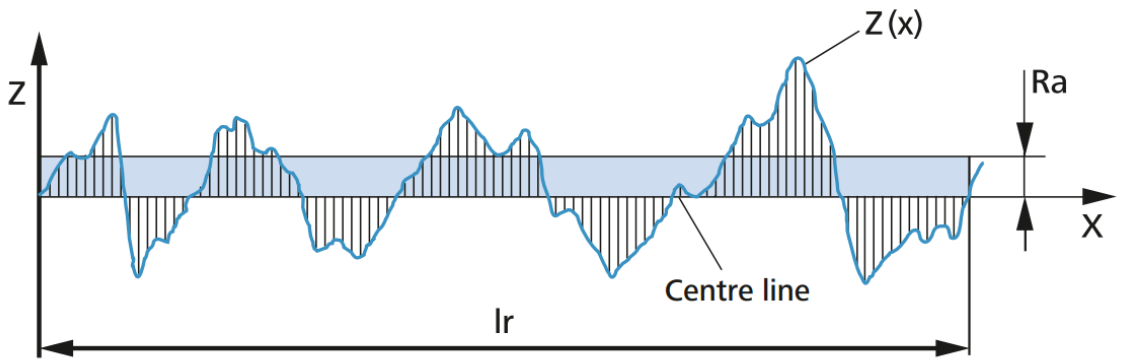

Figure 11: Ra - arthimetical mean roughness according to ISO 4287

The R_q value examines the deviations in the roughness over a the evaluation length, or in essence an indication of the variation in R_a.

$$R_q = \sqrt{\frac{1}{lr}\int_0^{lr} |Z^2(x)|\, dx} \qquad (28)$$

Another common parameter is the R_z parameter that averages the height difference between the lowest and highest points within an evaluation length. Two variants currently exist: R_{zDIN} and R_{zJIS}. The R_{zDIN} parameter takes an average of the highest and lowest

points for each sampling length. This is a Deutsches Instiut für Normung (DIN) and an American Society of Mechanical Engineers (ASME) standard. The R_{zJIS} value is a Japanese Industrial Standard (JIN) and uses the 5 highest and lowest over the evaluation length. Many other parameters exist to characterize the other aspects of the roughness, such as peak counts, profile depths, etc., but these are the most frequently used. Often times these will be combined with an R_k parameter to compare the likelihood of wear over its expected life based on roughness.

$$R_z = \frac{1}{s}\sum_{i=1}^{s} Y_i \qquad (29)$$

Where s is the number of sampling lengths and Y_i represents the difference in height between the maximum and minimum points each sampling length [45].

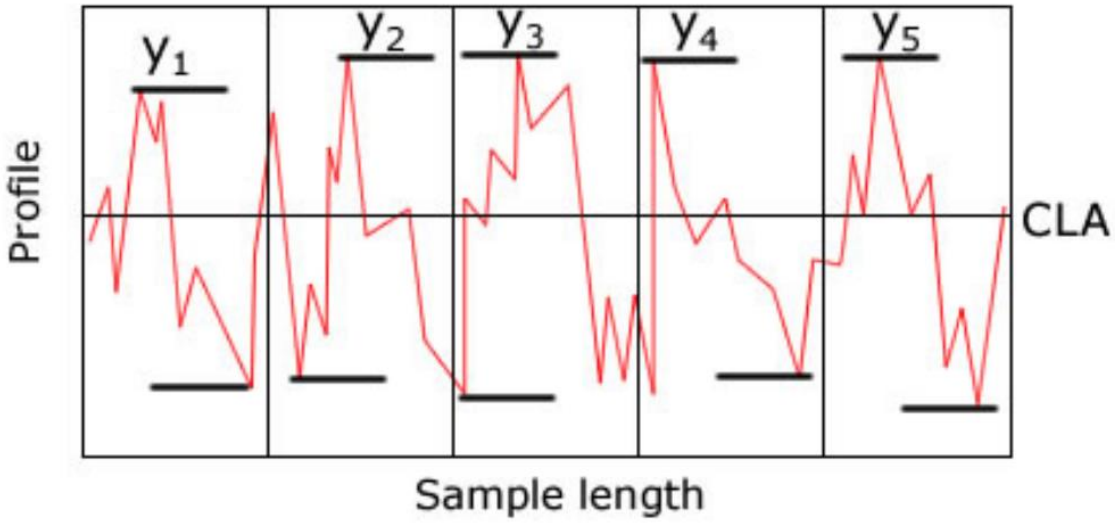

Figure 12: Representation of averaged depth of roughness parameter (Rz) definition according to DIN 4768 [45]

Chapter 3: Experimental Techniques

Samples were created from a selection of metal soap bars that were purchased from a proprietary vendor. Initially, the composition ratio of stearate to palmitate was unknown for each bar purchased. They were claimed to have differing ratios of palmitate and stearate as suggested by the usage rate curves demonstrating distinct rate differences under the same conditions. Additionally, a powder of nearly pure zinc stearate was purchased from a separate vendor to create a reference sample for use as a comparison. The samples were created from the purchased soaps in order to perform several tests including, liquid chromatography (LC), surface roughness, x-ray diffraction (XRD), and nanoindentation.

One of the primary objectives of this investigation is to examine the effect of the stearate to palmitate ratios on the mechanical properties of the selected zinc soaps through nanoindentation. In order to do so, each sample needed to be a solid of a reasonable size, each prepared in a similar fashion, have a top and bottom surface that are nominally parallel to one another, and have a surface roughness that would minimally influence the results. The first set of samples met the first three requirements in that they were of a reasonable size, both for handling with respect to the indentation depths and quantities, and in that they had fairly parallel surfaces from being injection molded in an approximately cuboid mold with low dimensional variation and controlled cooling times. However, the surface roughness was on the same order of magnitude as the indentation depths that were used, the exact process being unknown, and there was a significant amount of variation between indents of the same condition.

As a result, various samples were created in an attempt to meet these conditions, e.g. by melting the materials to form a puck and use surface tension for a level surface and by placing a clean glass side above the liquid (or soon to be liquid surface). These attempts were observed to have failed, likely as result of the samples' crystallization and due to the contraction of the samples as they cooled.

The samples that were utilized were formed by melting the material in a segment of a tube placed on a small tray. An aluminum tube was cut to an arbitrary length of approximately 30mm, which was chosen based on the fitment in the Hysitron TriboIndenter and for its ability to hold enough metal soap that would subsequently be able to melt and form adequately sized "pucks." The tube had an inner diameter of 21mm and an outer diameter of 23.4mm. After being cut to size, each tube was sanded on opposing sides and deburred in an effort to make the ends reasonably smooth and parallel to one another. The tubes were subsequently cleaned and wiped with isopropyl alcohol (IPA) along with a segment of a glass slide and a small aluminum tray measuring 44.3mm in diameter and with a height of 13mm.

The glass slide was placed on the base of the aluminum container and the tube was then placed atop the slide. In a few instances, the edges of the tray were folded inward to prevent the tube from sliding around and off of the glass slide; this had been seen to happen as the zinc soap permeated between the tube and slide. The tubes were filled to the greatest extent possible with fragments of one mixture of zinc soap. The amount of mass added to the tubes was somewhat arbitrary. As previously mentioned, the quantity was primarily chosen so that the resulting pucks were of a size that could be easily handled and would be less likely to fracture. Due to the brittle nature of the soap, thin

samples were very prone to cracking during the cooling process and from handling. The thicker samples cracked as well but remained somewhat intact, which allowed them to be handled better and provide a large enough surface area on which the indentation could be performed. Additionally, during the melting process, the metal soap had a tendency to permeate between the glass slide and tube causing a loss of mass from inside the tube. Thus, a sufficient amount of material was needed such that the resulting mass within the tube was "adequate."

To perform the melt, the samples were placed on the metallic base of a conventional oven. The oven's temperature was adjusted to 128 °C by ramping to the temperature in the course of about an hour. The temperature was not observed to have exceeded 131 °C and pressure was recorded to be between 28.8 and 29 inHg. The temperature was maintained for an hour after it was observed that the samples had melted. The samples were then carefully cooled and allowed to partially solidify on a metal shelf prior to being moved to a lab countertop, likely made of epoxy resin, where it completed equilibrating to ambient temperature.

One sample was made from a purchased pulverized metal soap and required more time to melt, likely due to its powder form and the reduced heat transfer. This sample also did not have an ideal surface texture upon solidification and was, therefore, re-melted. This method of melting and cooling was successful in creating a smooth and reflective surface on the side of each sample that melted onto the glass slide, to which will be referred to as the "top" of the tube and sample. The opposite side of these samples was then adhered to the tube using either a two-part epoxy resin or cyanoacrylate so that the metal soap remained in position. Shortly after applying the adhesive, the sample was flipped over so

that the adhesive did not leach down and coat the sample surface. The samples were then prepared for the nanoindentation by adhering three steel discs to the "base" of the tube with epoxy-resin, so that the sample would better remain in position on the magnetic stage as the stage traversed.

A test matrix of nanoindentations was performed on each sample that incorporated a prescribed loading time, holding time, maximum force and unloading rate. The maximum forces ranged from 1000μN to 5500μN and the holding time was varied between 20 seconds and 400 seconds. The remaining parameters were held constant. Each test condition was repeated 12 times on the same sample for a total of 240 quasi-static nanoindentations per sample. This test matrix can be seen in Table 1 below.

The nanoindentation was performed using the Berkovich indenter tip, (Hysitron TI-0039), which has a tip radius of ~100nm when new. A calibration was performed by indenting a polycarbonate reference sample to establish an area function for the tip's projected area.

From these samples, the actual stearate to palmitate ratio for each was determined through a liquid chromatography (LC) test to verify that the compositions of each sample were indeed different. The surface roughness of each sample was determined using CLSM to examine several spot sizes in the vicinity of the nanoindentations and to confirm approximate contact depth.

The samples that were created for the nanoindentations were slightly recessed below the edge of the aluminum tube. A separate set of samples were similarly created by preparing the samples in an aluminum tray, excluding the glass slide and aluminum tube. An XRD

test was performed on this second set of samples in an effort to avoid any difficulties capturing low angle X-rays that might have been impeded from the lip of the aluminum tube. The XRD data was collected to compare the crystallinity of the samples with respect to each other, the original bars and with data from literature.

Table 1: Test matrix for the nanoindentation of each zinc soap

Cell Number	Loading Time (s)	Max Load (μN)	Holding Time (s)	Unloading Rate (μN/s)
1	5	1000	20	200
2	5	1000	60	200
3	5	1000	100	200
4	5	1000	200	200
5	5	1000	400	200
6	5	2500	20	200
7	5	2500	60	200
8	5	2500	100	200
9	5	2500	200	200
10	5	2500	400	200
11	5	4000	20	200
12	5	4000	60	200
13	5	4000	100	200
14	5	4000	200	200
15	5	4000	400	200
16	5	5500	20	200
17	5	5500	60	200
18	5	5500	100	200
19	5	5500	200	200
20	5	5500	400	200

Chapter 4: Results and Conclusions

4.1 Results and Discussion

4.1.1 Liquid Chromatography Results

The ratio of zinc stearate to zinc palmitate in each sample was determined by a liquid chromatography (LC) test, which confirmed that the samples each, indeed, did have a distinct zinc stearate to zinc palmitate ratio, as suggested by the vendor. Table 2 below shows the resulting ratios that were found from the re-melted samples created for the tests.

Table 2: Zinc Stearate to Zinc Palmitate Ratios for Re-melted Samples

Stearate	to	Palmitate
53	:	47
56	:	44
76	:	27
95	:	5

The sample in the last row with 95% zinc stearate was purchased from a different vendor than the rest and is the sample that was purchased as a powder and the closest to being nearly 100% of either type of zinc soap.

4.1.2 Nanoindentation Impressions

The residual impressions of the nanoindenter shown in Figure 13 and Figure 14 were imaged using an optical confocal microscope using differential interference contrast with circularly polarized light. The appearance of the surfaces differed from sample to sample in regards to the grain boundary definition and some of the surface defects present. However, in regards to the indentations, their features were similar between samples in that the low force indentations created a well defined plastic region and that the high force indentations did not seem to have a large amount of pile-up nor visible cracking at the corners. The two images below are of indentations on the 56% stearate sample.

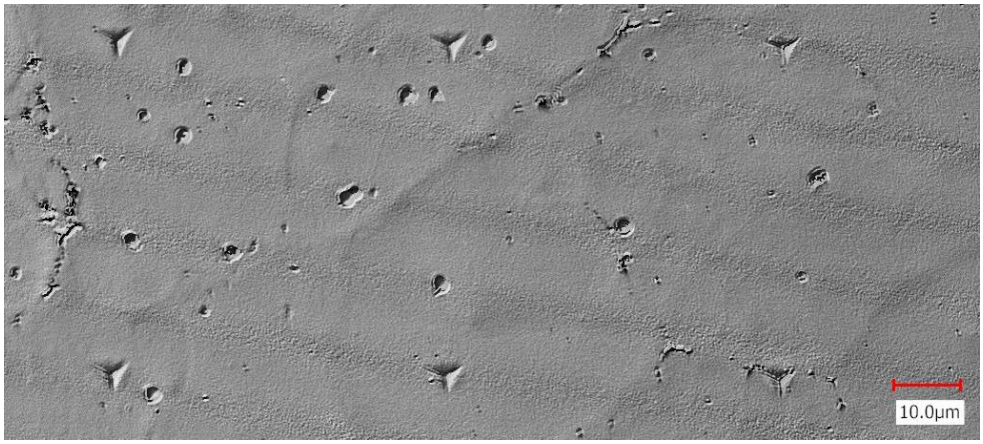

Figure 13: C-Laser DIC image of low force indents on the 56% stearate sample.

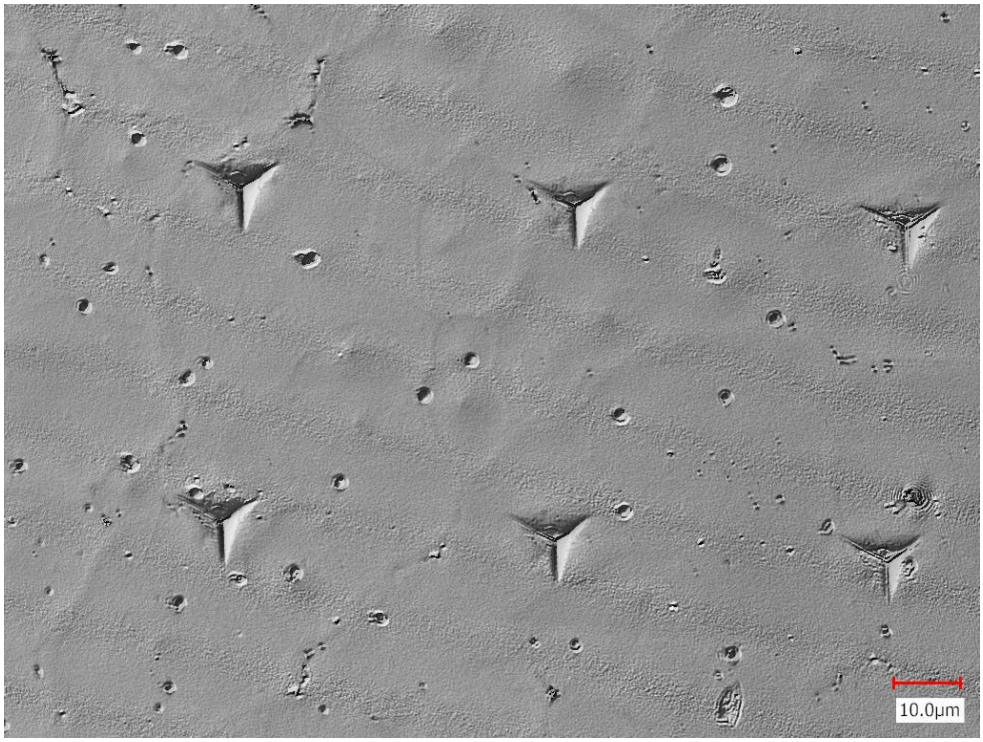

Figure 14: C-Laser DIC image of high force indents on the 56% stearate sample.

4.1.3 Force-Displacement Curves

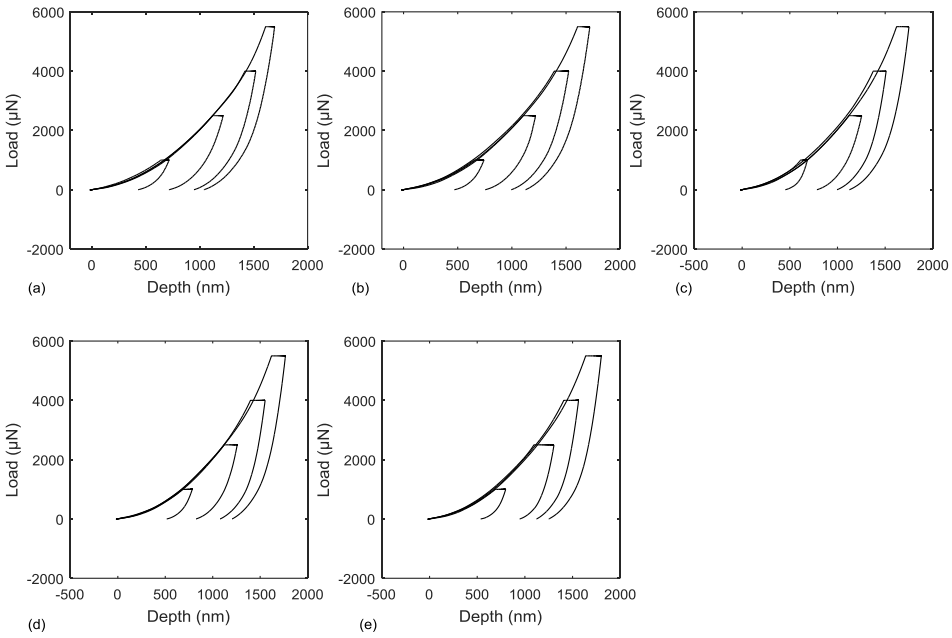

Figure 15: Force-displacement curves for the 95% zinc stearate sample at various holding times: (a) 20s, (b) 40s, (c) 100s, (d) 200s, (e) 400s

The resulting loading-unloading curves from the nanoindentation of the 95% zinc stearate (and 5% zinc palmitate) sample are shown in Figure 15 (a)-(e). It can be seen that the loading curves for a given holding time overlap one another. Since this portion of the curve represents the elasto-plastic deformation that occurs within the sample, the consistency that is indicated by the overlap of this portion of the curve suggests that the energy required to deform the sample was fairly constant between indents of the same holding time, but different maximum force. Additionally, the loading and unloading curves are smooth and continuous and do not appear to have any discontinuities. The force-displacement curves of the other samples appear very similar to Figure 15 in this regard and, although not shown here, the majority of the force-displacement curves of a single condition on a single sample overlapped each other also suggesting that the material surface and subsurface for each sample was homogeneous for the indentations under consideration.

4.1.4 Hardness and Combined Modulus

The values of the reduced modulus and the hardness for each indentation were calculated using the TriboScan software program by Hysitron in conjunction with the area function of the tip. The area function of the Berkovich tip was found to be

$$A = 42.488h_c^2 + 13552h_c + 0.1172h_c^{1/2} + 0.049187h_c^{1/4} + 0.049187h_c^{1/8} + 0.45051h_c^{1/16} + 2.2261h_c^{1/32} \quad (30)$$

after calibrating it against a reference sample of polycarbonate. Ideally, the value of the first coefficient should be near that of an ideal indenter, which for a Berkovich tip is 24.5. As mentioned, no indenter is perfect and therefore it is recommended that this constant be within ± 5 with as few subsequent terms as possible. Comparatively, the area function presented in Equation (30) deviates from this significantly in that the coefficient exceeds the recommended bounds and the polynomial exhibits a high degree of freedom. Considering that a Berkovich tip is a common indenter tip and that this particular one has been utilized for a while, it is logical this large coefficient would be reflective of this. As long as the area function accurately represents the actual projected area of the tip, the results should not be impacted greatly. Additionally, indentations that are more shallow, on the order of 50-100nm, are more susceptible to being influenced by an irregular tip [34]. Since the indentations performed were in the range of 600-1700nm, a fully developed plastic region was able to be developed, leaving the potential blunting of the tip of minimal concern.

If the tip was damaged, this would likely result in the area function poorly representing the actual area of the indenter tip, though the deeper indentations from the test may be less affected. An investigation of the tip condition will be pursued to see in what way it deviates from an ideal tip. If the tip is chipped or damaged in some sort of manner, the damage likely occurred prior to the testing because a calibration was performed prior to the testing of each sample and the coefficients marginally varied. Thus, even if the magnitudes are skewed as a result of tip damage, since the tip condition remained

constant for all the samples, the trends that were observed should be representative of the actual trends that exist inter-sample and intra-sample.

Beginning with the 95% zinc stearate sample, the mechanical property data was subsequently compiled and a statistical analysis was performed to determine whether there was a statistically significant influence of the holding time and maximum applied load on the modulus. Using a 95% confidence interval, it appears that both the holding time and the maximum load have a statistically significant impact on the modulus. The R^2 value for the initial model, however, was fairly low, approximately 64%. A Box-Cox plot was then created in an attempt to find a better model to fit the data. Despite a transformation of the data, the residual remained low. Looking at the residual plot, one point distinctly had a larger residual, which was the average modulus at 1000μN and 100s holding time. Upon the exclusion of this point, the R^2 value increased to about 88% indicating a better fit of the data. Additionally, the maximum load seemed to have the greater impact than that of the holding time. An example of this relationship can be seen in Figure 16 which shows the trend of the modulus with respect to the maximum load at each holding time. Although the trend regarding the increase in the reduced modulus with respect to holding time is a bit more difficult to discern than that of maximum load, it can be seen that, in general, the modulus does increase with an increase in holding time.

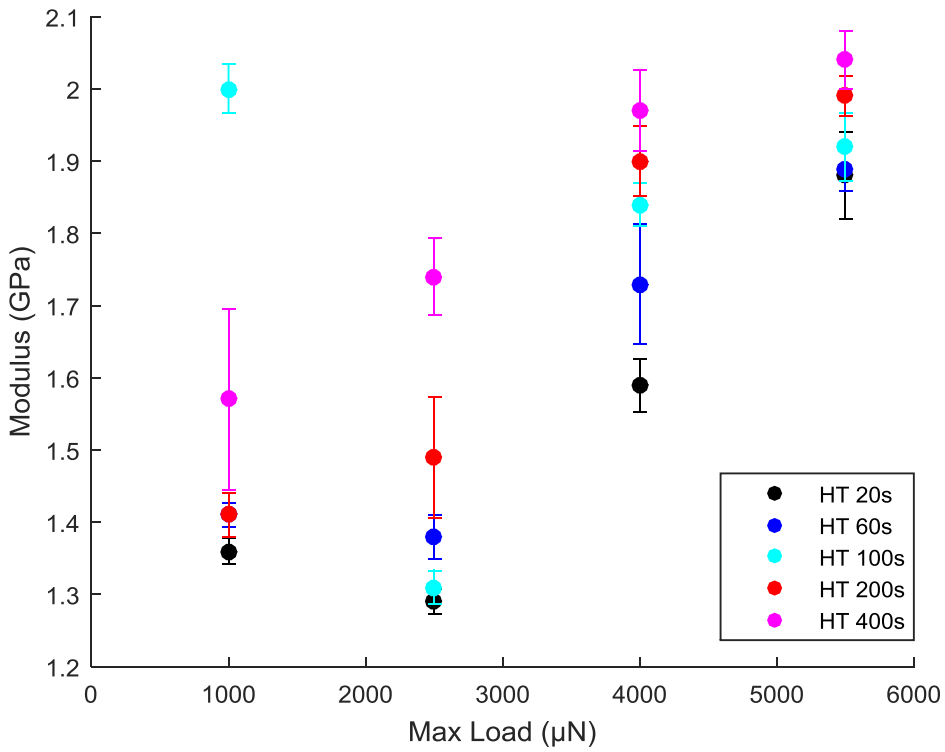

Figure 16: Variation of the reduced moduli with respect to maximum load and different holding times for indentations on a 95% zinc stearate sample**.** The error bars in the plot signify one standard deviation in either direction.

Using a statistical contour plot, such as the one shown in Figure 17, the influence of the maximum load and holding time on the reduced modulus can be seen more clearly. The contour plot demonstrates that the greatest reduced modulus is achieved when both the applied maximum load and holding time are maximized for the tested range.

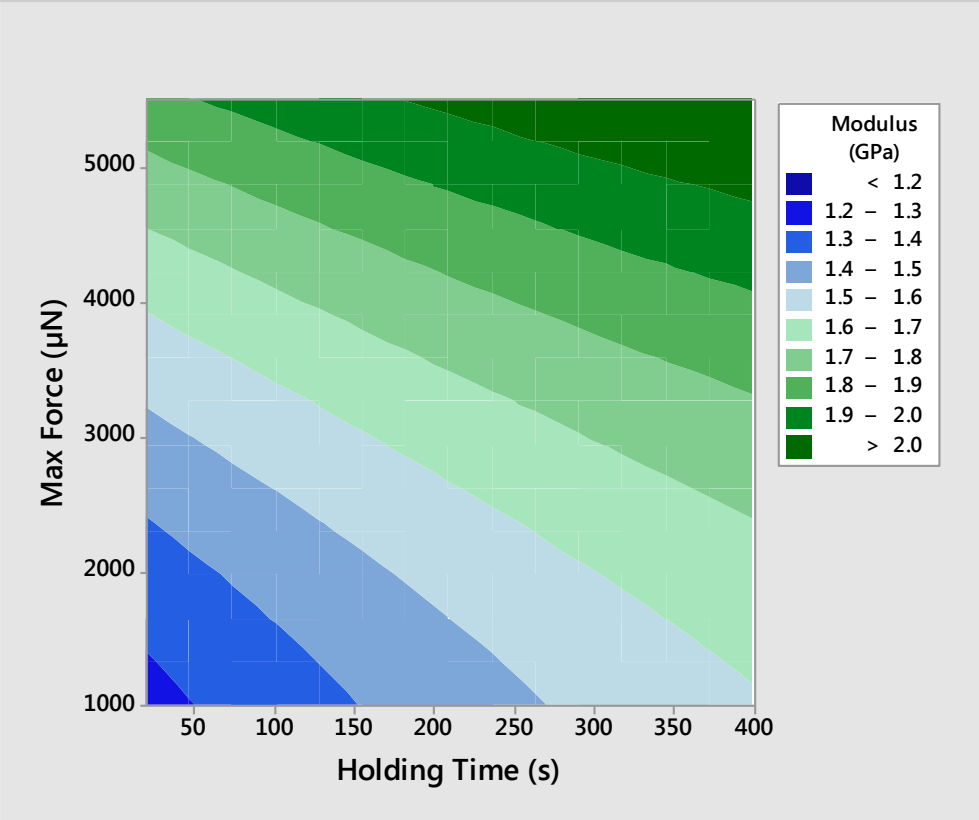

Figure 17: Statistical contour plot showing the relationship between the maximum applied load and the holding time on the reduced modulus for the 95% zinc stearate sample.

A similar trend is seen in regards to the hardness of the 95% zinc stearate sample. A statistical analysis shows that both the maximum applied load and holding time of the indentations have a noteworthy effect on the hardness of the sample with an R^2 value of approximately 89%. In this case, an increase in the maximum applied load also results in a higher hardness. However, the inverse relationship exists between the hardness and the holding time in that as the holding time increases, the hardness decreases. These relationships can be seen in the plot in Figure 18.

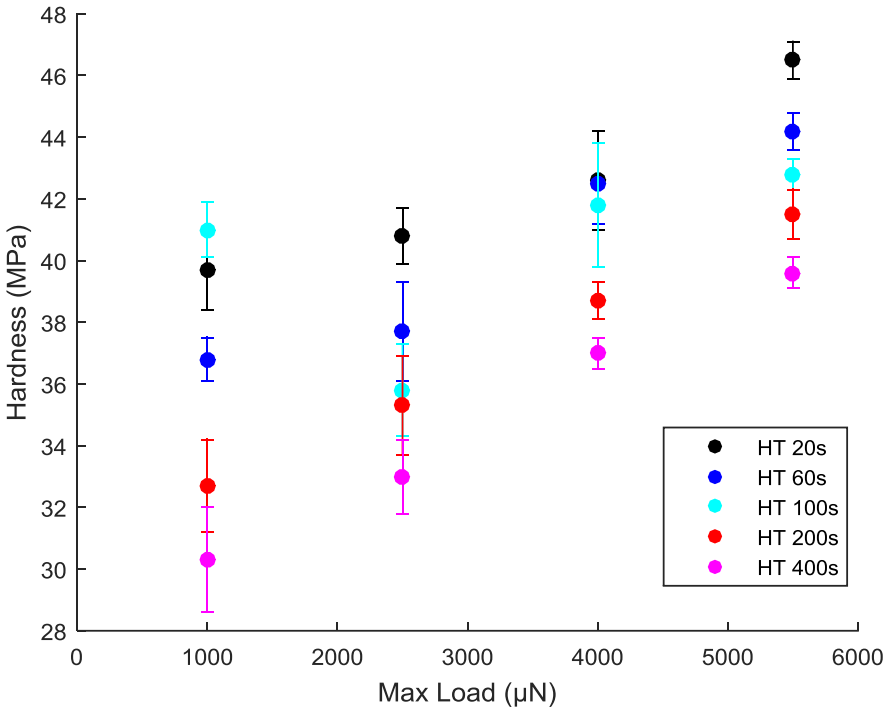

Figure 18: Variation of the hardness with respect to maximum load and different holding times for indentations on the 95% zinc stearate sample. The error bars in the plot signify one standard deviation in either direction.

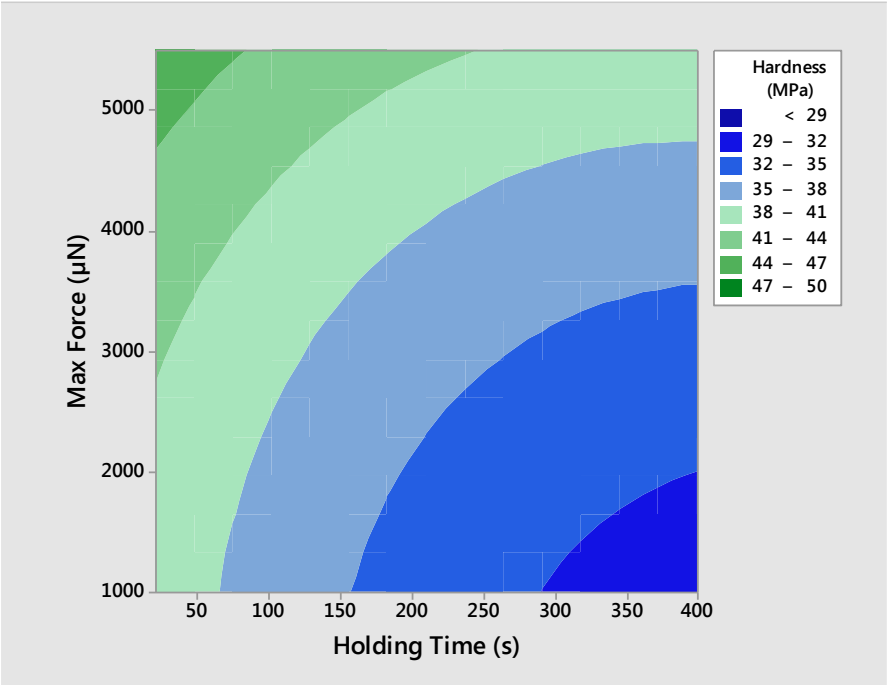

Figure 19: Statistical contour plot showing the relationship between the maximum applied load and the holding time on the hardness for the 95% zinc stearate sample.

Additionally, the contact depth is also strongly connected to the applied maximum force and the holding time. As can be seen in Figure 20 and Figure 21, as the maximum applied force and the duration of the holding time increase, the contact depth also increases. As the contour plot demonstrates, the influence from the maximum force is the greatest factor.

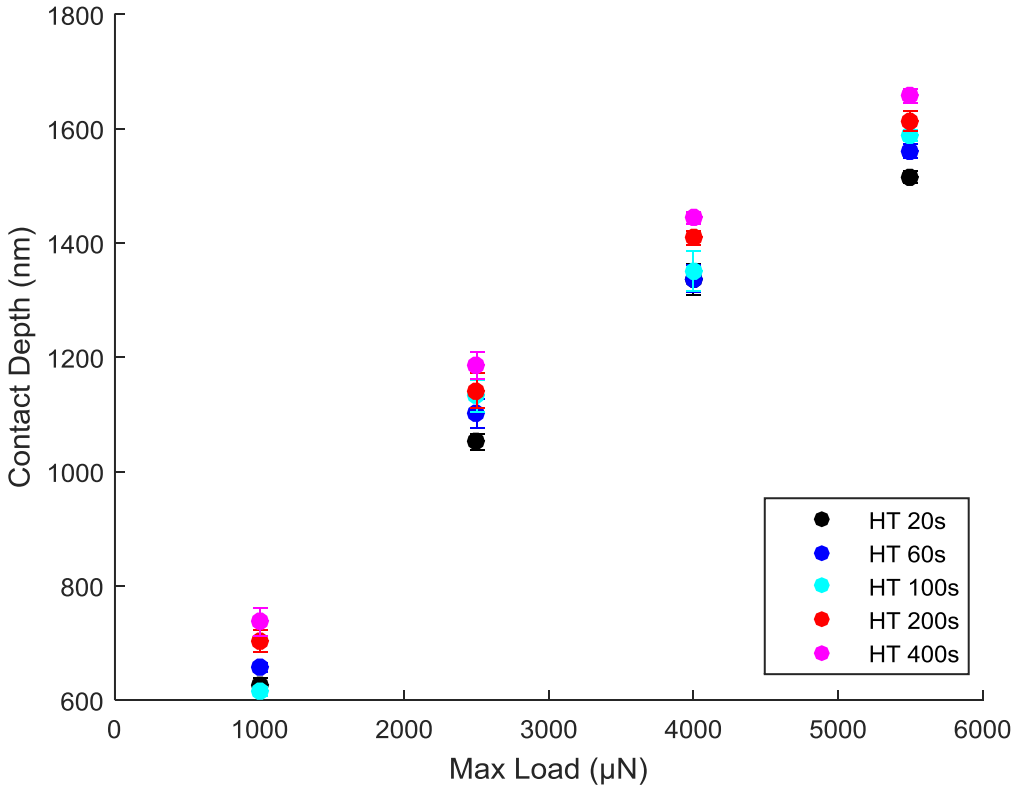

Figure 20: Variation of the contact depth with respect to maximum load and different holding times for indentations on the 95% zinc stearate sample. The error bars in the plot signify one standard deviation in either direction.

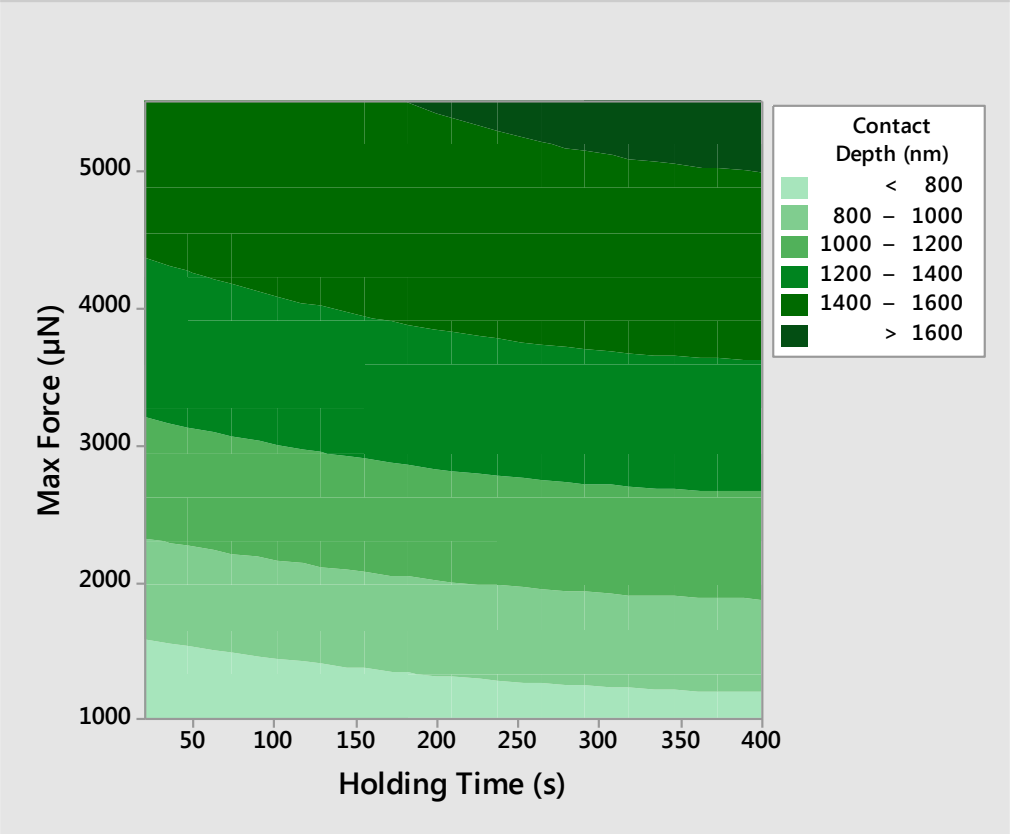

Figure 21: Statistical contour plot showing the relationship between the maximum applied load and the holding time on the contact depth for the 95% zinc stearate sample.

During the holding period of the indentations on this sample, the contact depth was plotted with respect to the time with both axes zeroed to the beginning of the holding time. It was seen that the contact depth increased as a function of the holding time during this period, which indicates that creep occurred. Unfortunately, due to time constraints, the time constants for the creep were not calculated making it difficult to discern whether or not a trend exists between magnitudes of the maximum load and holding time on creep in the sample. There does not seem to be any clear visual cues that either the change in holding time or maximum load result in higher or lower creep rate. The supporting figures can be seen in the appendix.

In regards to the other three samples, they also behaved similarly to the 95% zinc stearate sample. In regards to contact depth, all of the samples had the greatest contact depth at the greatest maximum load and at the largest holding time. The maximum applied force was also the largest influence, which can be seen from the contour plots in that the bands of contact depth seem to stretch out with a minimal slope for each maximum load.

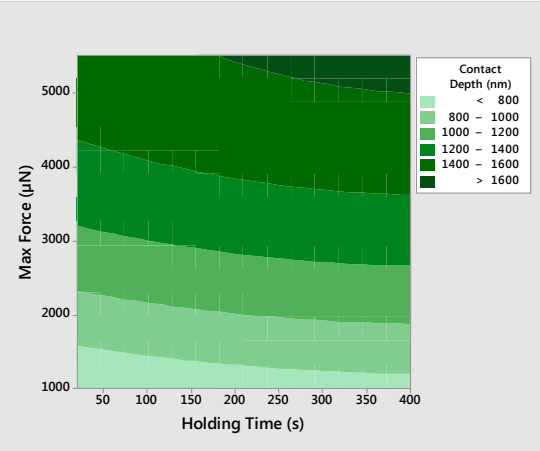

Figure 22: Statistical contour plot showing the relationship between the maximum applied load and the holding time on the contact depth for the 95% zinc stearate sample.

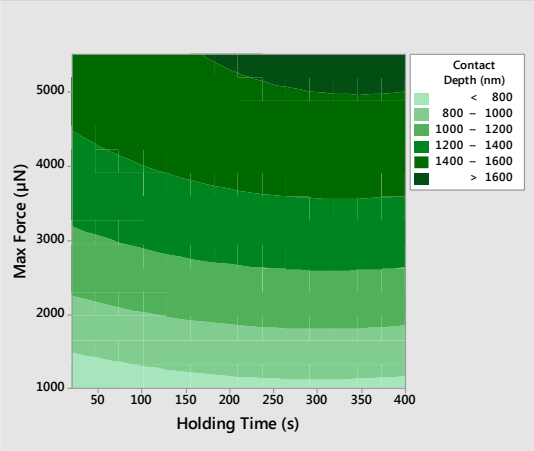

Figure 23: Statistical contour plot showing the relationship between the maximum applied load and the holding time on the contact depth for the 73% zinc stearate sample.

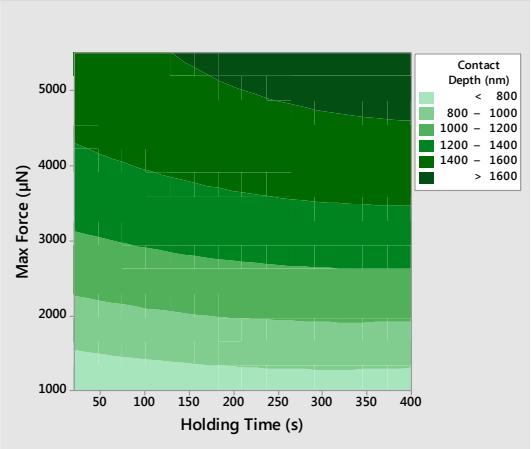

Figure 24: Statistical contour plot showing the relationship between the maximum applied load and the holding time on the contact depth for the 56% zinc stearate sample.

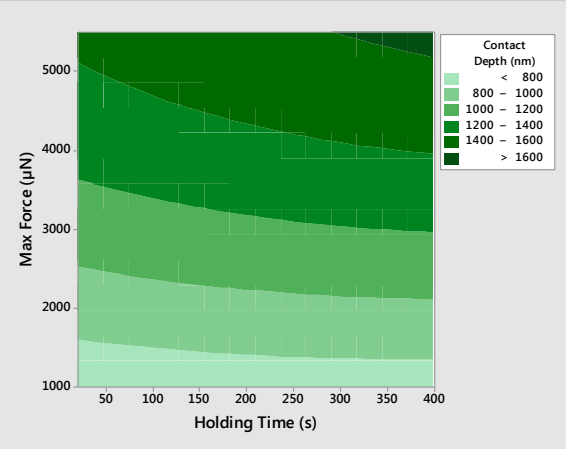

Figure 25: Statistical contour plot showing the relationship between the maximum applied load and the holding time on the contact depth for the 53% zinc stearate sample.

Likewise, the reduced modulus for all of the samples shows a general trend in which the greatest modulus is observed at the maximum applied load and holding time and the minimum is found at the other extremum. The two middle compositions, the 73% and 56% zinc stearate samples, behaved slightly differently from the other two. These two samples exhibited less of a change in modulus as the two parameters were varied and had more of a "flat modulus" range. This was especially the case for the 56% zinc stearate sample, which had the least modulus change of them all.

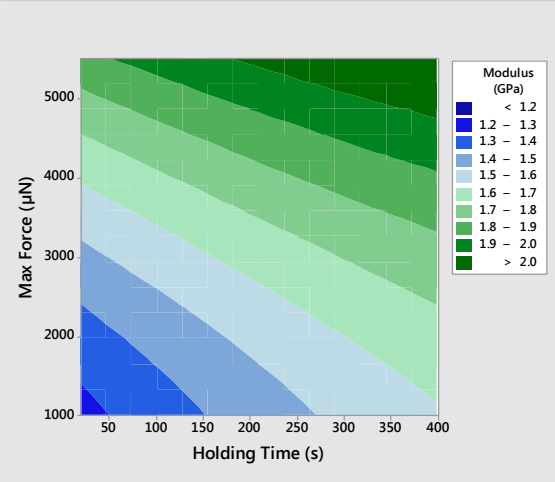

Figure 26: Statistical contour plot showing the relationship between the maximum applied load and the holding time on the reduced modulus for the 95% zinc stearate sample.

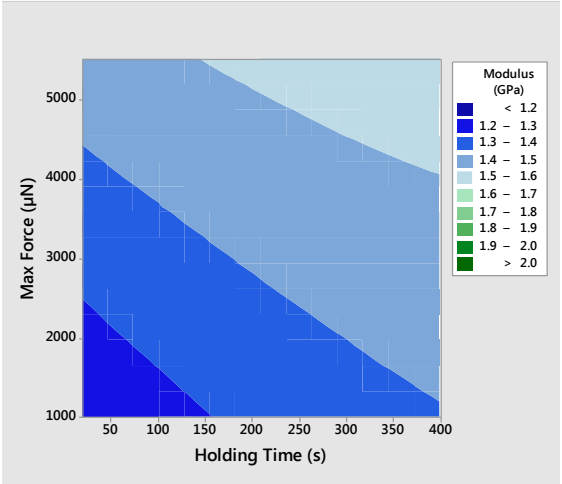

Figure 27: Statistical contour plot showing the relationship between the maximum applied load and the holding time on the reduced modulus for the 73% zinc stearate sample.

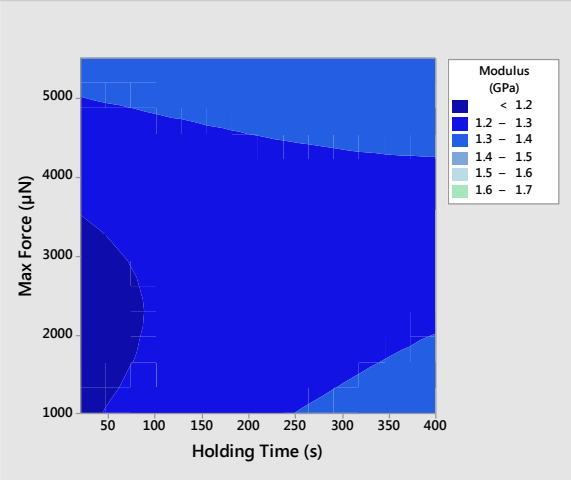

Figure 28: Statistical contour plot showing the relationship between the maximum applied load and the holding time on the reduced modulus for the 56% zinc stearate sample.

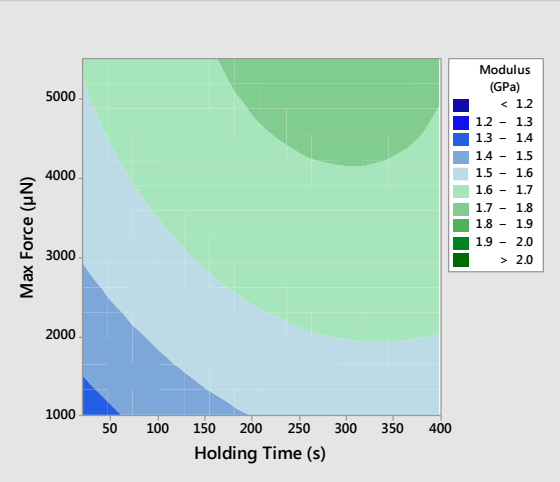

Figure 29: Statistical contour plot showing the relationship between the maximum applied load and the holding time on the reduced modulus for the 53% zinc stearate sample.

The trend observed regarding the influence of the parameters on hardness was also observed for the remaining samples. As before, the hardness consistently increased with the maximum applied and decreased as the holding period increased, leaving the maximum hardness values at the highest maximum applied force and the lowest holding time. Additionally, the range of hardness values under these conditions was fairly consistent across samples.

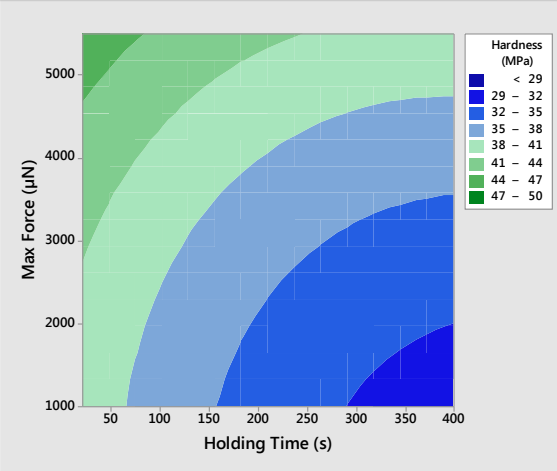

Figure 30: Statistical contour plot showing the relationship between the maximum applied load and the holding time on the hardness for the 95% zinc stearate sample.

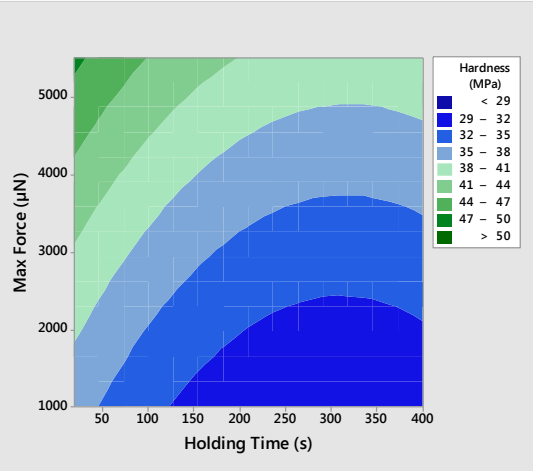

Figure 31: Statistical contour plot showing the relationship between the maximum applied load and the holding time on the hardness for the 73% zinc stearate sample.

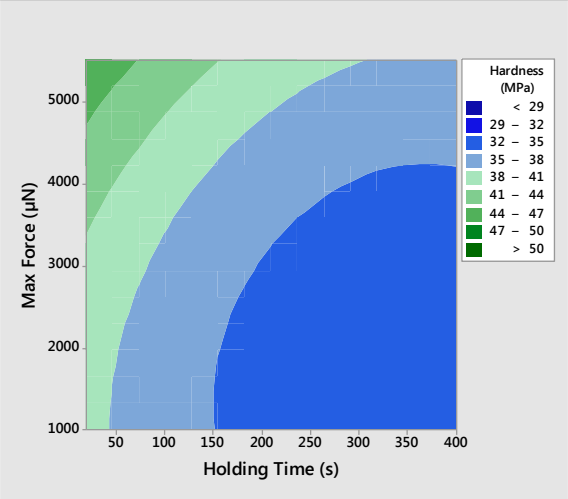

Figure 32: Statistical contour plot showing the relationship between the maximum applied load and the holding time on the hardness for the 56% zinc stearate sample.

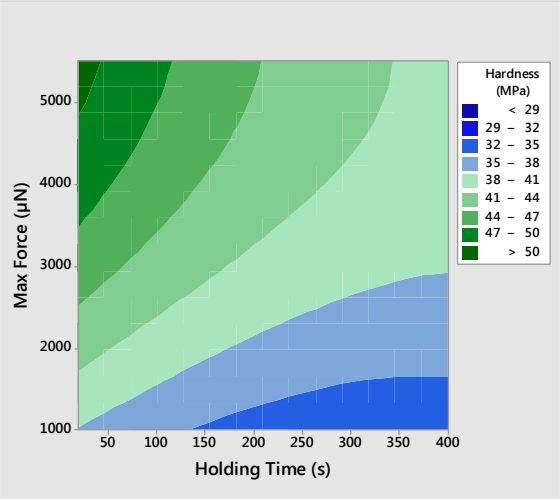

Figure 33: Statistical contour plot showing the relationship between the maximum applied load and the holding time on the hardness for the 53% zinc stearate sample.

In regards to the relationship between samples, it does appear that the composition has a statistically significant influence on the modulus and hardness as can be seen from the following plots. In all of the charts below, there appears to be a quadratic relationship between the composition and dependent variables of interest.

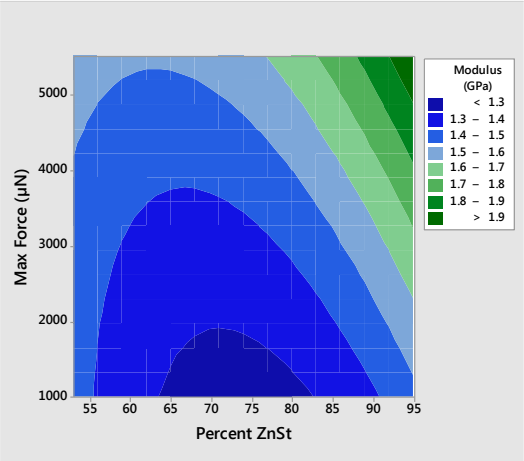

Figure 34: Modulus vs Max Force and Percent ZnSt

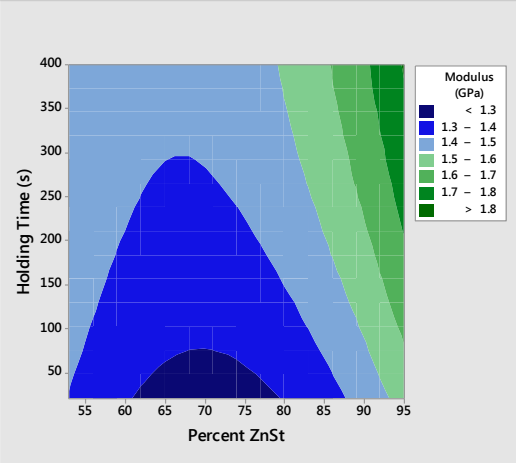

Figure 35: Modulus vs Holding Time and Percent ZnSt

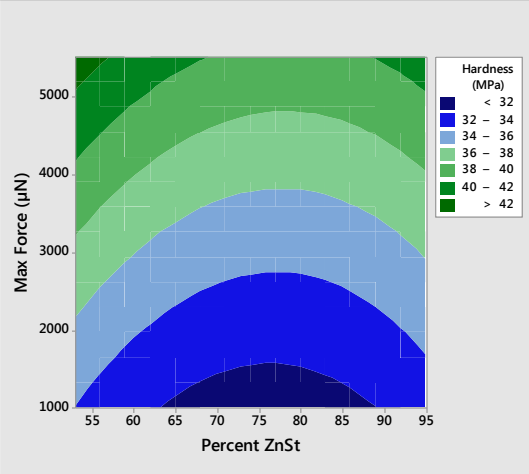

Figure 36: Hardness vs Max Force and Percent ZnSt

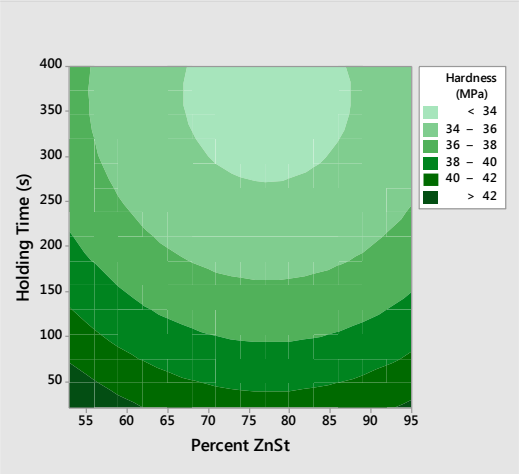

Figure 37: Hardness vs Holding Time & Percent ZnSt

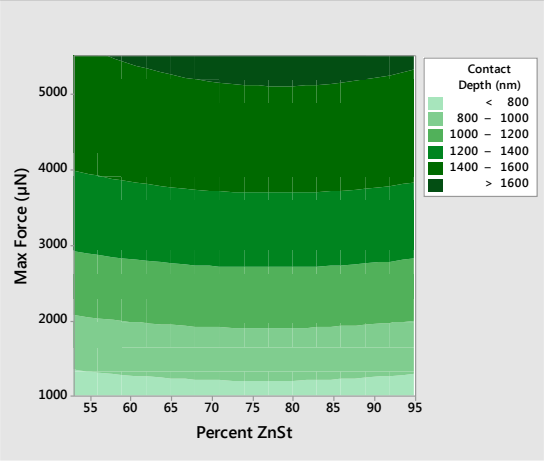

Figure 38: Contact Depth vs Max Force and Percent ZnSt

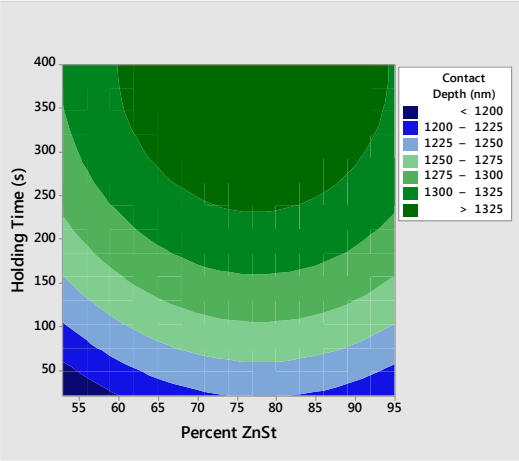

Figure 39: Contact Depth vs Holding Time and Percent ZnSt

The creep plots displaying the change in contact depth with respect to time for the remaining samples are not shown here, but the same observation made for the 95% zinc stearate sample applies to the rest. In summary, a distinct trend was not readily discernible from the contact depth versus time plots, however, the data could be used to determine the time constant for each creep plot so that the time constants could be compared and trends could be more easily observed.

4.1.5 X-Ray Diffraction

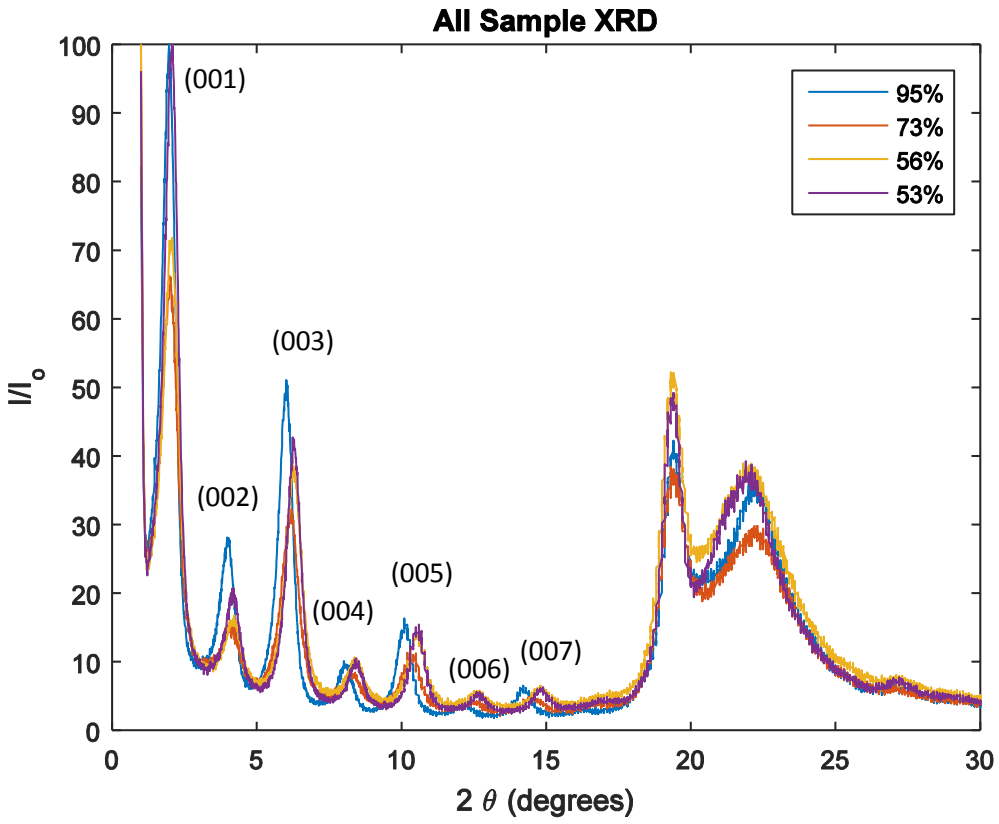

Figure 40: Normalized XRD of all prepared samples

As shown in Figure 40, the XRD of the samples showed that each exhibited peaks that were comparable to one another as discussed by Robinet et al, especially in the indicated ranges of 3 to 10° and 20 to 30° 2θ. No clear distinctions were seen in the 20 to 30° 2θ range and the peaks were of low intensity and the peak width of that region was fairly broadened. Slight shifts were seen between most of the curves in the first cluster of peaks, namely between the compositions that varied the most. If we examine a closer view of the region, as shown in Figure 41, it becomes visible that the peaks of the 53% and 56% zinc stearate samples have peaks that align most closely. Conversely, the other

two compositions of zinc soap have peaks that are shifted slightly to the right with respect to this pair.

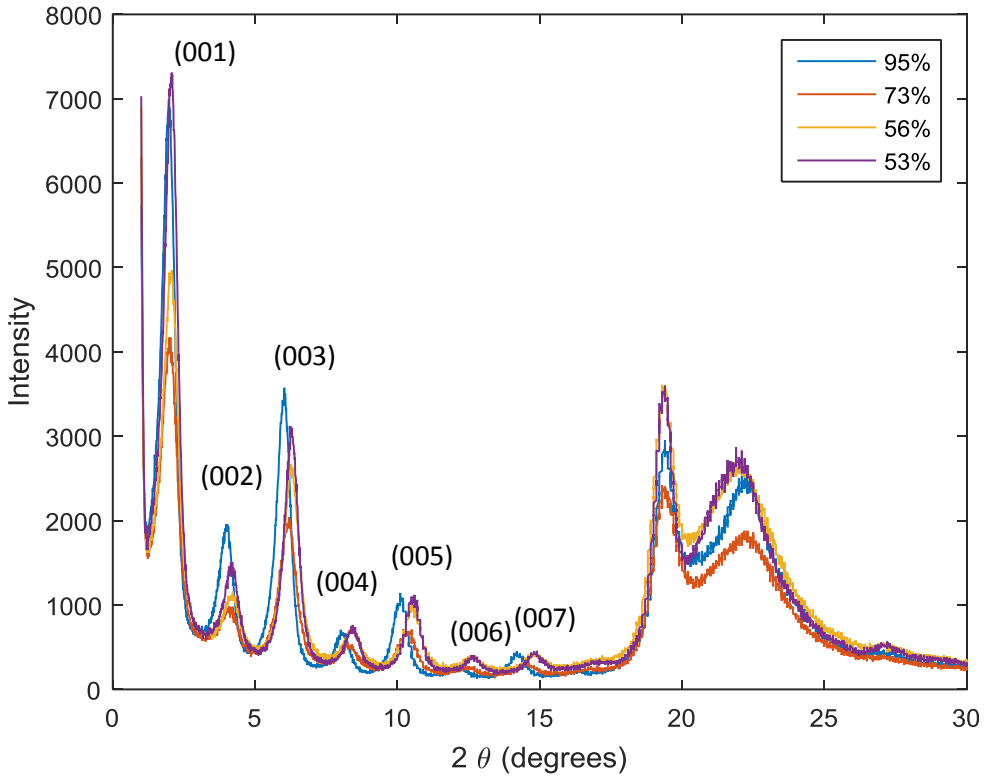

Figure 41: Zoomed in area of Figure 40

A comparison of the XRD of a couple of samples was made with respect to results from the same material in bar form. The figures showing the comparison of the 56% zinc stearate sample and the 73% zinc stearate sample are shown below. As can be seen in both plots, the peaks for the same material align well despite their processing difference. The peaks for the bar also are more well-defined and have a greater intensity and more peaks are seen for the XRD of the bar than are seen in the XRD of the sample.

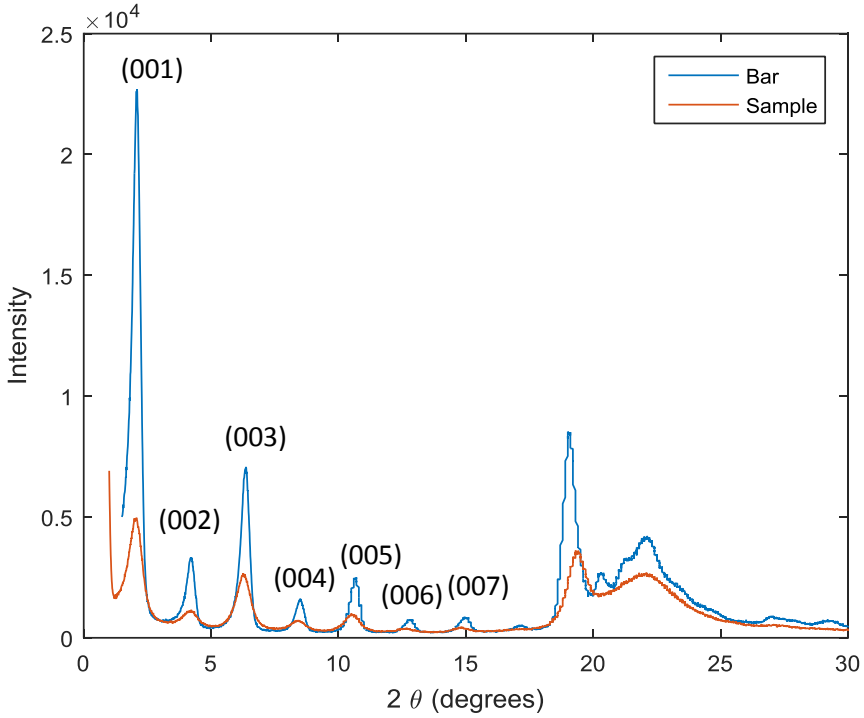

Figure 42: Comparison of the XRD of the as-received bar and the melted samples of 95% zinc stearate

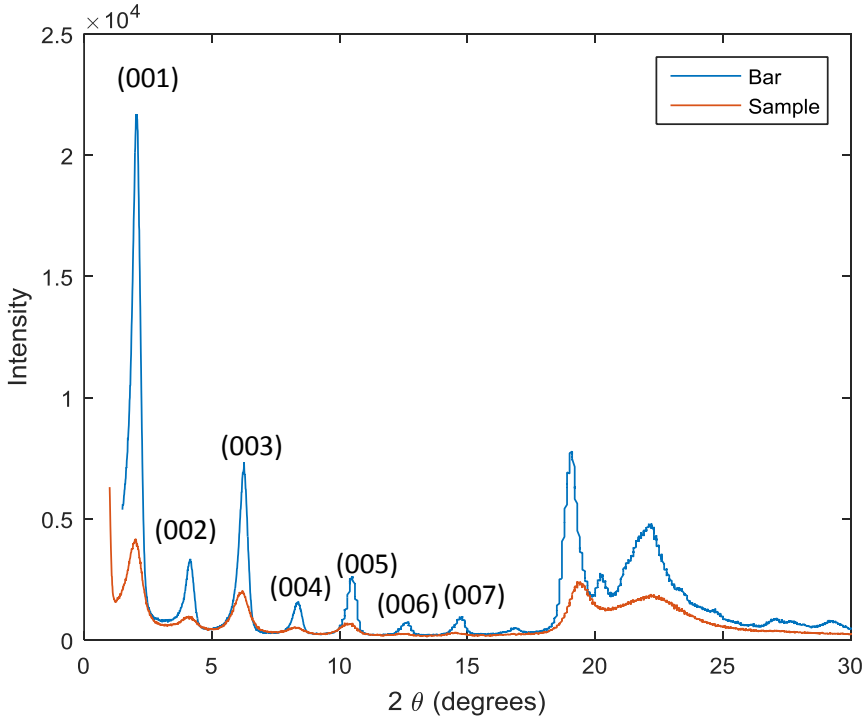

Figure 43: Comparison of the XRD of the as-received bar and the melted samples of 73% zinc stearate

4.2 Conclusions

The uniformity of the loading and unloading curves, as exemplified by Figure 15, for each sample indicates that the surface and sub-surface structure are fairly homogeneous in the region tested. The elasto-plastic, or loading, region of each curve aligned very well with indents in other locations and under different loading conditions indicating that the elastic and plastic behavior of the material was very consistent along with the energy required to deform it. The smoothness and lack of discontinuities in these curves allude that defects, fracturing, and pressure-induced phase changes were not present in the depth range tested, which would otherwise be present in the curve as "pop-ins," "pop-outs," "shoulders," or sudden horizontal lines in the loading or unloading regions [46, 47].

The general trend of an increasing modulus with increasing holding time for all of the samples suggests that the strain is an influencing factor. As can be seen in Figure 26 through Figure 29, the contact depth increases as a result of both maximum force and holding time. The application of a load on the material, especially in a very localized region, imparts a localized stress which induces plastic strain of the material. This effectively also densifies the material, which is reasonably susceptible to densification as a result of the formation process and nature of the crystal structure. Upon examining microscope images of the nanoindentations, it appears that the majority of the indentations fell within a single grain and that the grains were generally large enough to accommodate them. Densification is therefore thought to occur within the crystal structure itself. As a result of this densification, the stiffness of the region also increases, which increases the reduced modulus. However, as mentioned before, the there was no

indication of a pressure-induced phase change as a result of the indentations since there were not any discontinuities visible on the force-displacement curves. This, to some degree supports the claim that the surface tested was not amorphous, since it is plausible that the pressure induced could change a region from amorphous to crystalline. This evidence is not sufficient in itself, since if it is amorphous this would only signify that a pressure induced phase change did not occur. More evidence leading to this claim is presented throughout this section.

This densification hypothesis supports the trend of increasing hardness as a result of increasing maximum load in that the densification also likely results in strain hardening of the material. Since the true hardness is a measure of the resistance to plastic deformation and strain hardening creates resistance to further plastic deformation, it is logical that this would increase the hardness as the maximum load is increased. The decrease in the measured value of hardness, however, as a function of holding time is likely to be a result of creep. As could be seen from the contact depth versus time plots, the contact depth increased as the holding time increased, signifying the occurrence of creep. Since the measure of hardness is calculated using the projected contact area at the maximum load, the value is affected since creep increases the contact area at this load. Assuming that strain hardening is the driving mechanism, this would not occur if the samples were amorphous, which, again, indirectly supports the claim of poly-crystallinity.

As mentioned before, there appears to be a nonlinear relationship of the zinc stearate to zinc palmitate ratio in relation to the measured values. Although based on the collected data, this trend appears to be statistically significant, it is important to keep in mind that

only four compositions are reported here. Although a conclusion cannot be confidently drawn here, it is interesting to note that the sample nearest to 50% zinc stearate and the samples nearest to pure zinc stearate behaved differently than that other two compositions. This behavior might be in accordance with the crystal structure as discussed by Sawada and Konaka, but a deep investigation would be necessary to confirm this hypothesis. The paper from Sawada and Konaka claims that the compositions that are nearer to 50% zinc stearate and 100% zinc stearate have a tendency to lack voids in their crystal structure whereas the compositions in between 50% and 100% are more likely to inherently contain voids within the crystal structure due to the uneven balance between the two different metal salts as can be seen in Figure 2 [17]. This leaves the potential for voids to be created by the aligning of the shorter chains, or the palmitate chains, and stearate to palmitate chains since the long spacing is likely driven by the longest coupling of the stearate to stearate chain since it has the greater composition compared to the palmitate. It is possible that the increased probability of voids in the "intermediate" compositions, those between purity and 50%, lower the overall modulus of the soap, which would be consistent with the results.

As could be observed from Figure 34 through Figure 39, the quadratic relationship is seen for nearly every parameter. If indeed it is possible to observe the more "nano" effects of the crystal structure over the microstructure of the material, it could also be thought that the voids decrease the crystals resistance to plastic deformation and, therefore, would have a lower hardness than the structures with fewer or no voids. This relationship might be able to be seen in the plots of the creep behavior, but again it is difficult to confidently justify this statement without finding the creep time constants.

However, this relationship could be inferred from Figure 39 of the contact depth versus holding time and composition plot since the largest contact depth would be achieved at the end of the holding period.

Upon examining the XRD patterns, the first thing to note is that there are seven well defined peaks below the 20° 2θ range, which is in accordance with the study by Robinet and Corbeil [9, 10]. In the 20° to 30° 2θ range, the peak definition is greatly lacking for the samples, but is more distinguished for the bars.

The XRD patterns of the original bars were than compared those to the melted samples, which showed that the peaks of the melted samples aligned very well with those of the manufactured bar of the same composition despite the processing difference. This indicates that the degree of internal stress was the same in both cases despite one being created under the pressure of injection molding and the under in ambient pressure. Additionally, as can be seen in Figure 42 and Figure 43, the width of each comparable peak for both the prepared sample and the bar spanned the same 2θ range, but the intensity and definition of their peaks differed. The samples had shorter and less defined peaks than the bars did, and using Scherrer's equation it can be found that the bars have a smaller full width at half maximum than the bars, indicating a smaller crystal size. This was expected as a result of the way the melted samples were cooled. Since the edges of the melted samples cooled fairly rapidly, the surface likely consists of several smaller crystals. The surface of each samples also has a distinct difference in appearance when compared to its center and is clearly seen through the cross-section near the surface. The surface appears somewhat translucent on the surface and, when looking at the cross-section, it gradually transitions to a much more opaque appearance in the center. The fact

that there are peaks that align with the bars and XRD patterns from literature, affirms that there is some degree of crystallinity indicating that the samples could not be completely amorphous, if amorphous at all. The other noticeable distinction between the manufactured bars and the melted samples was the appearance of additional peaks and sharper peaks from manufactured bar in comparison to the melted samples in the 20° to 30° 2θ range. Additionally, as mentioned before, there does appear to be observable grain boundaries evident on the surface, again supporting its crystalline nature.

When comparing the prepared samples against each other, it can be seen that the peaks shift slightly with respect to each composition. This is also in accordance with literature which indicates that the group of peaks below 20° 2θ range are representative of the long spacing of the of the crystal [9, 10, 12, 13, 16, 17]. The long spacing of the crystal corresponds to the separation of the planes of zincs, which is directly related to the length of the fatty acid chains. As indicated by the paper by Sawada and Konaka, the long spacing also changes with the varied ratio of stearate and palmitate, as described before and shown in Figure 2 [17]. The shifts in the peaks agree with these claims with the near purity sample having peaks with the lowest 2θ value and the 53% zinc stearate sample with the largest 2θ value, though the 53% and 56% stearate peaks overlap fairly closely. This implies that the 95% zinc stearate sample should have the largest long-spacing and the 53% zinc stearate sample should have the shortest. The d-spacings are listed in Table 3 and shows that the they decrease with decreasing percent zinc stearate, in accordance to the claim by Sawada and Konaka [17]. This is fairly remarkable considering that the stearate and palmitate only differ by two methylene groups.

Table 3: Long spacing of samples using the peak near 6° 2θ as suggested by literature

Percent ZnSt	d-spacing (Ang)
95	43.9
73	42.9
56	41.9
53	41.5

Chapter 5: Future Work

As demonstrated by the x-ray diffraction results and other corroborating evidence, the bars and the samples that were created are both likely crystalline which supports that metal soap is likely lamellar, since a lamellar solid would have a crystalline structure. Although more evidence would need to be gathered to ultimately prove this, the evidence that has been gathered thus far aligns with the claims made by literature [9, 10, 12, 13, 16, 17]. To further demonstrate its lamellar nature, it is recommended that future work be done to acquire data corresponding to its behavior under shear. As mentioned in the lubricant section, the particles that would be deposited on the PC drum would be need to self-align in a preferred orientation allowing for shear to occur on the least resistive planes, and would likely do so. Observing the behavior of these samples and/or those of the manufactured bars would hopefully display that relatively low values of shear stresses are required to shear the materials against themselves indicating their benefit as a solid-lubricant. It would also be of interest to measure the shear stress as a function of load to see if there is any variation.

Additionally, the seemingly high reduced modulus that these samples exhibit is likely beneficial to the ultimate goal of using this as a protective medium to the PC drum. As mentioned before, lamellar solids tend to require more force to cleave the soap perpendicular to their lamellae. With the fracture toughness related to the ratio of the elastic modulus and the hardness, it is possible that these soaps have a high fracture toughness and are able to protect the drum surface by preventing penetration of the film

layer. The use of the nanoindenter to determine the fracture toughness of these metal soaps would help in corroborating this claim.

A greater examination of the creep and compliance information would likely be beneficial as often the printers exhibit stagnation periods. Performing the creep tests in a variety of different temperatures and humidities would also contribute to this. These would all tie back to being able to utilize this information in a representative model of an interface of this system, namely the applicator or cleaning blade interfaces. Furthermore, these tests could also be performed on samples or films that have been placed in an alternating current electric field to observe the effects this would have on the mechanical properties of the film.

A compression test of the bar or representative sample would also assist in correlating between the behavior of the bulk material and the results from the nanoindentation. Although, since the particles deposited are on the order of the indentation, the nanoindentation results are likely to be more closely representative of what occurs at the interfaces of interest.

Although this has not been thoroughly investigated, the bars have been seen to exhibit some notable internal porosity. This has been casually observed by the collection of toner particles in what appears to be micro-voids in the bar and on the surface microtome samples of the bars. This is speculated to be a result of the injection molding process, although this could be a result of "loose" fragments falling out of place to create cavities during use or handling. This could be investigated through the comparison of the density of re-solidified samples and the bars. This would also likely cause a distinct difference in the compression test of the bulk material with respect to the nanoindentation of the soap.

It would also be of great benefit to the creation of a model if the poisson ratio of the material were found. This would allow for values, such as the elastic modulus to be calculated from the data collected through nanoindentation.

Appendix I: Figures

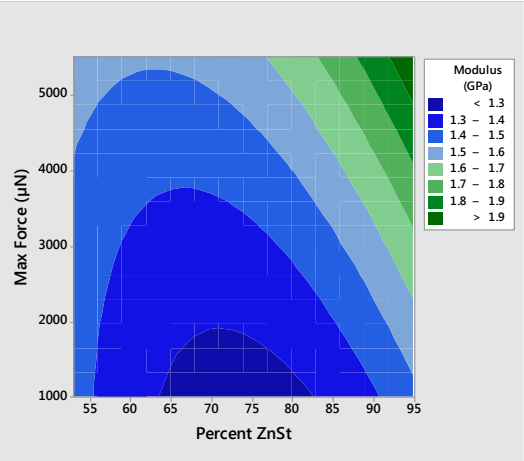

Figure 44: Modulus vs Max Force and Percent ZnSt

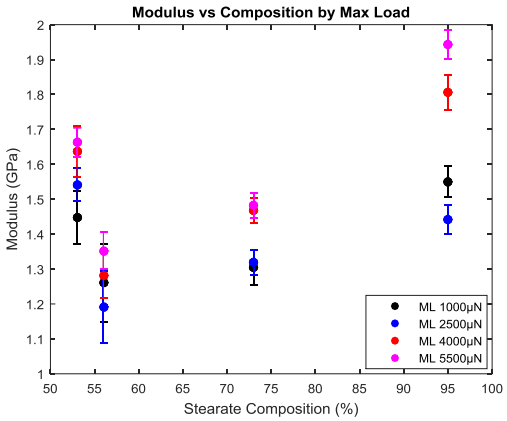

Figure 45: Modulus vs Max Force and Percent ZnSt

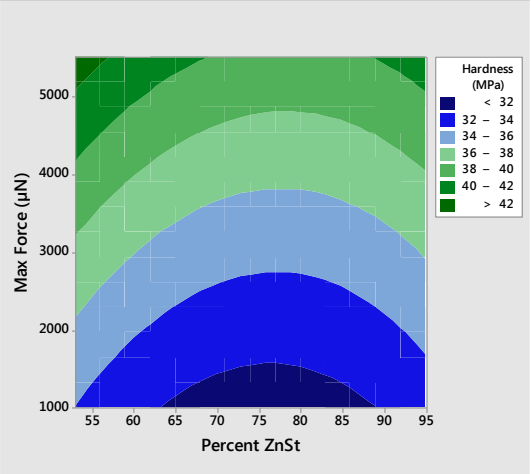

Figure 46: Hardness vs Max Force and Percent ZnSt

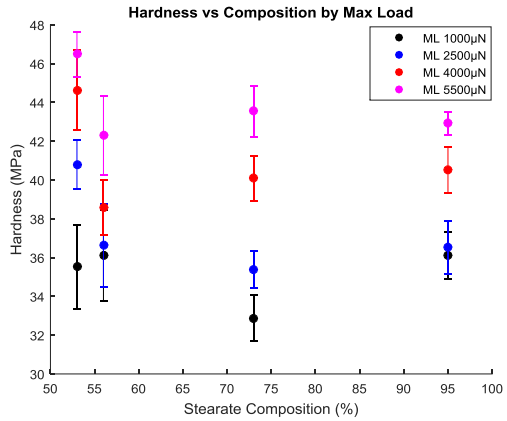

Figure 47: Hardness vs Max Force and Percent ZnSt

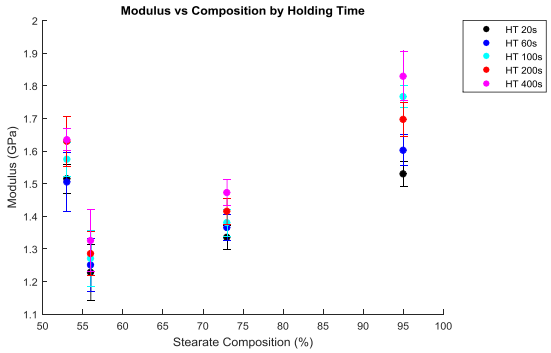

Figure 48: Modulus vs Holding Time and Percent ZnSt

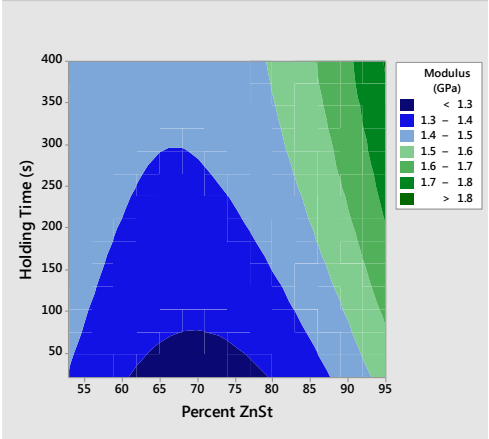

Figure 49: Modulus vs Holding Time and Percent ZnSt

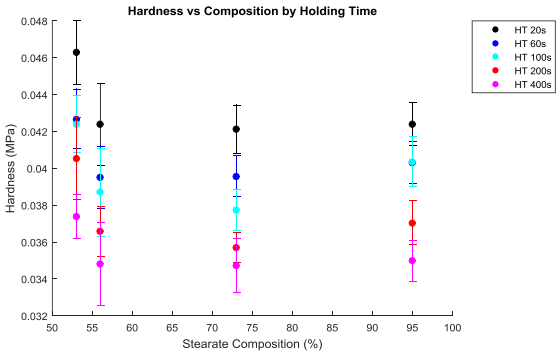

Figure 50: Hardness vs Holding Time and Percent ZnSt

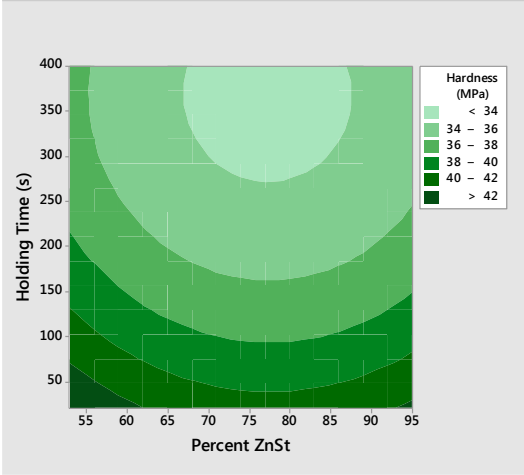

Figure 51: Hardness vs Holding Time and Percent ZnSt

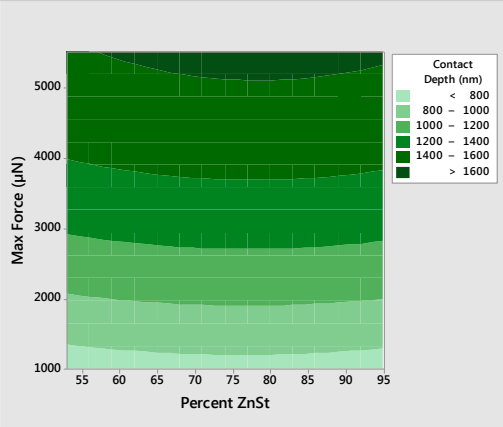

Figure 52: Contact Depth vs Max Force and Percent ZnSt

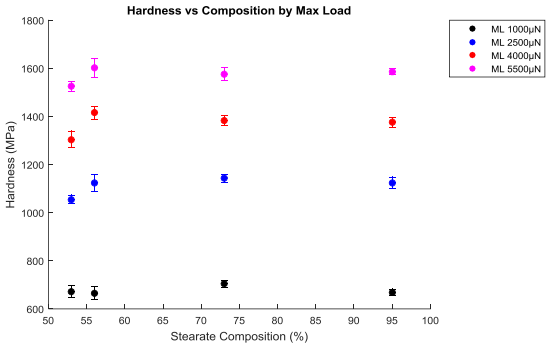

Figure 53: Contact Depth vs Max Force and Percent ZnSt

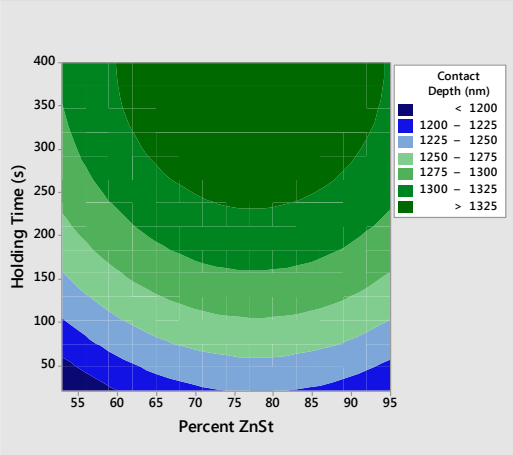

Figure 54: Hardness vs Holding Time and Percent ZnSt

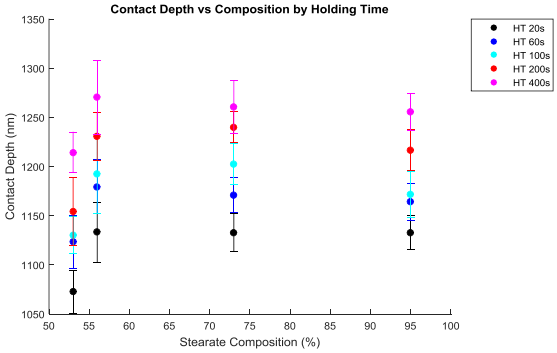

Figure 55: Hardness vs Holding Time and Percent ZnSt

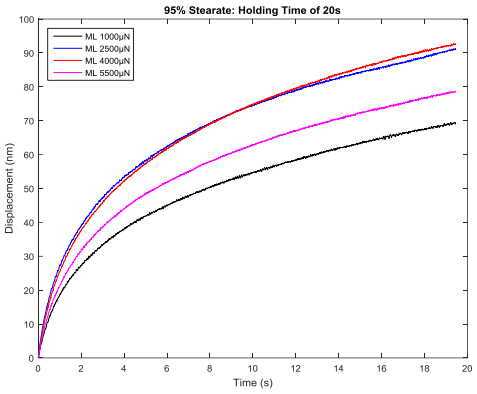

Figure 56: Creep vs Time for a Holding Time of 20s for the 95% Stearate Sample

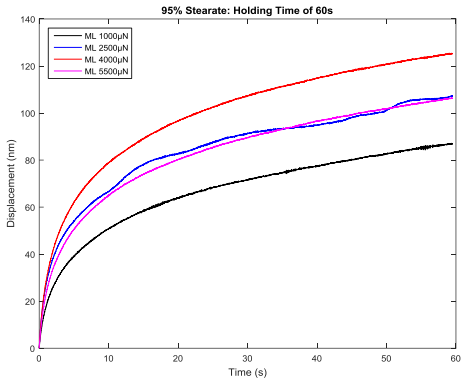

Figure 57: Creep vs Time for a Holding Time of 60s for the 95% Stearate Sample

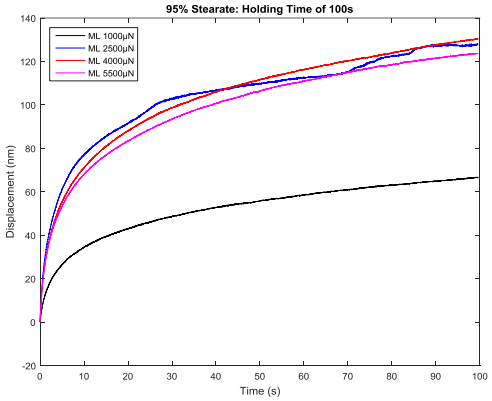

Figure 58: Creep vs Time for a Holding Time of 100s for the 95% Stearate Sample

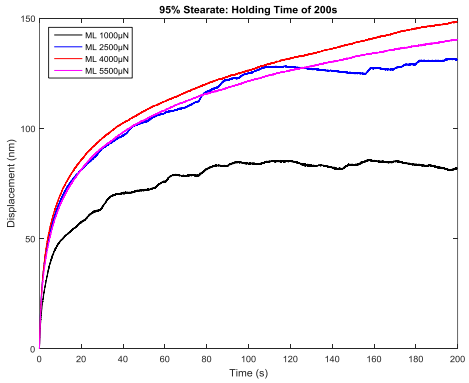

Figure 59: Creep vs Time for a Holding Time of 20s for the 95% Stearate Sample

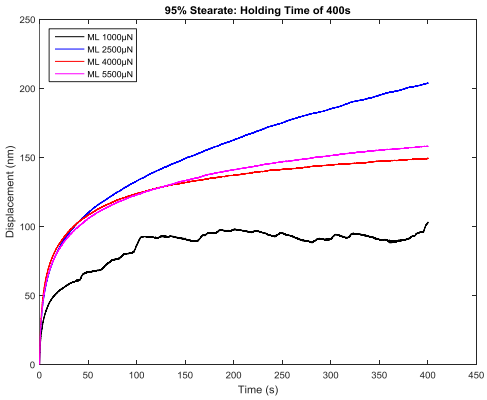

Figure 60: Creep vs Time for a Holding Time of 400s for the 95% Stearate Sample

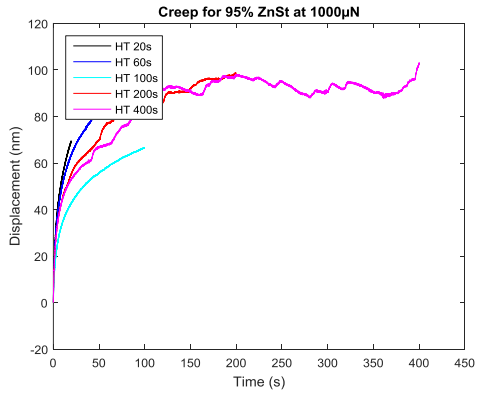

Figure 61: Creep vs Time for a Max Load of 1000 μN for the 95% Stearate Sample

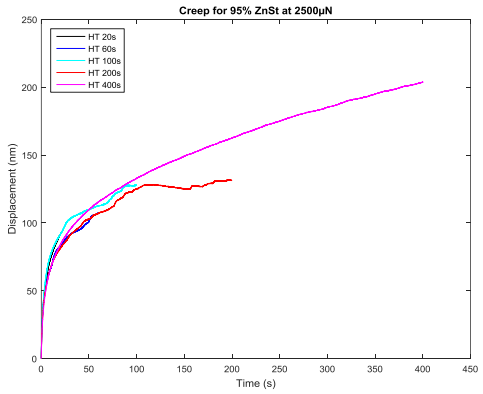

Figure 62: Creep vs Time for a Max Load of 2500 μN for the 95% Stearate Sample

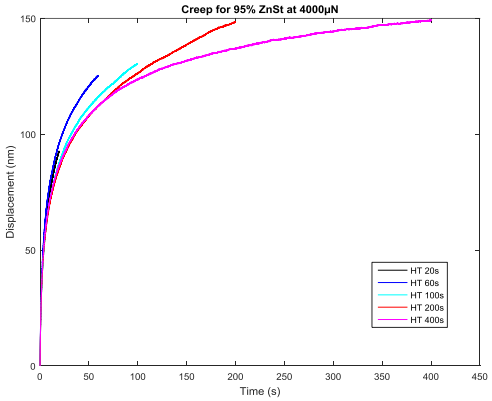

Figure 63: Creep vs Time for a Max Load of 4000 μN for the 95% Stearate Sample

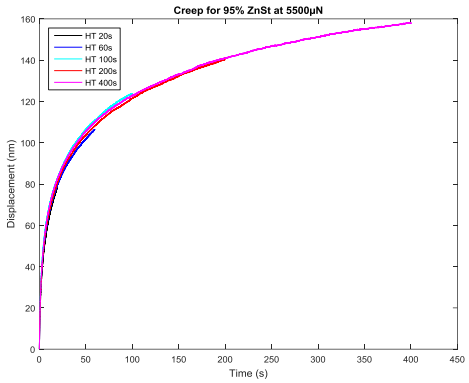

Figure 64: Creep vs Time for a Max Load of 5500 μN for the 95% Stearate Sample

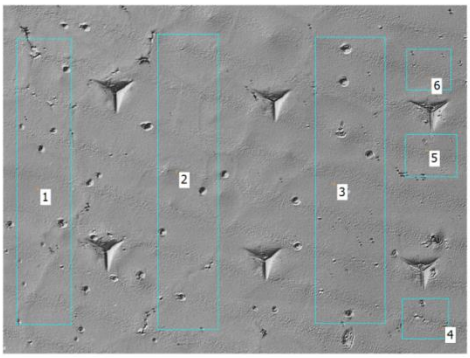

	Rp	Rv	Rz	Ra	Rq	Rsk	Rku	Rδc	Rmr	Rmr(c)	Comment	Rδc ref. mr	Rδc Com...	Rmr ref....	Rmr lvl....	Rmr(c) c...
Seg.1	0.9um	0.4um	1.3um	0.0um	0.0um	-1.1168	32.1535	0.0um	50.00%	0.03%		25.00%	75.00%	50.00%	0.0um	0.6um
Seg.2	0.6um	0.5um	1.1um	0.0um	0.0um	-1.4746	28.3684	0.0um	50.00%	0.15%		25.00%	75.00%	50.00%	0.0um	0.6um
Seg.3	0.2um	0.6um	0.8um	0.0um	0.0um	-1.9825	21.1912	0.0um	50.00%	99.58%		25.00%	75.00%	50.00%	0.0um	0.4um
Seg.4	0.2um	0.3um	0.5um	0.0um	0.0um	-0.2077	9.4923	0.0um	50.00%	76.24%		25.00%	75.00%	50.00%	0.0um	0.3um
Seg.5	0.2um	0.2um	0.4um	0.0um	0.0um	0.1124	2.9652	0.1um	50.00%	54.82%		25.00%	75.00%	50.00%	0.0um	0.2um
Seg.6	0.2um	0.1um	0.3um	0.0um	0.0um	0.4958	3.7665	0.0um	50.00%	0.12%		25.00%	75.00%	50.00%	0.0um	0.2um
Seg.7																
Seg.8																
Seg.9																
Seg.10																

	Rp	Rv	Rz	Ra	Rq	Rsk	Rku	Rδc	Rmr	Rmr(c)	Comment
Total	2.4um	2.0um	4.4um	0.2um	0.2um	-4.1733	97.9370	0.3um	300.00%	230.94%	
Max.	0.9um	0.6um	1.3um	0.0um	0.0um	0.4958	32.1535	0.1um	50.00%	99.58%	
Min.	0.2um	0.1um	0.3um	0.0um	0.0um	-1.9825	2.9652	0.0um	50.00%	0.03%	
Ave.	0.4um	0.3um	0.7um	0.0um	0.0um	-0.6956	16.3228	0.0um	50.00%	38.49%	
Std. DV	0.3um	0.2um	0.4um	0.0um	0.0um	0.8898	11.5625	0.0um	0.00%	40.51%	
3sigma	0.8um	0.5um	1.1um	0.0um	0.0um	2.6695	34.6875	0.0um	0.00%	121.52%	

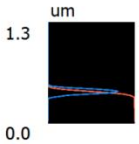

BAC/ADF(#1)

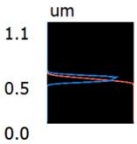

BAC/ADF(#2)

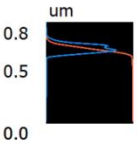

BAC/ADF(#3)

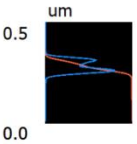

BAC/ADF(#4)

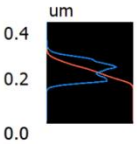

BAC/ADF(#5)

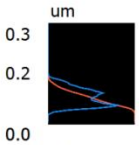

BAC/ADF(#6)

JIS B0601:2001(ISO 4287:1997)
Cutoff : Roughness λs None, λc None

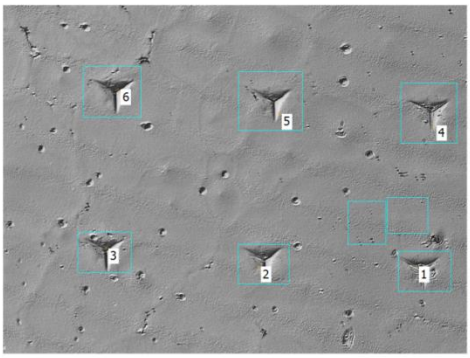

	Rp	Rv	Rz	Ra	Rq	Rsk	Rku	Rδc	Rmr	Rmr(c)	Comment	Rδc ref. mr	Rδc Com...	Rmr ref....	Rmr lvl....	Rmr(c) c...
Seg.1	0.2um	0.5um	0.7um	0.1um	0.1um	-2.4636	10.2971	0.1um	50.00%	94.16%		25.00%	75.00%	50.00%	0.0um	0.3um
Seg.2	0.1um	0.7um	0.8um	0.1um	0.1um	-2.7673	12.5491	0.1um	50.00%	96.77%		25.00%	75.00%	50.00%	0.0um	0.4um
Seg.3	1.0um	0.8um	1.8um	0.1um	0.1um	-2.6768	13.7079	0.1um	50.00%	2.32%		25.00%	75.00%	50.00%	0.0um	0.9um
Seg.4	0.3um	0.7um	1.0um	0.1um	0.1um	-3.1732	14.9275	0.1um	50.00%	94.16%		25.00%	75.00%	50.00%	0.0um	0.5um
Seg.5	0.8um	0.7um	1.5um	0.0um	0.1um	-3.5015	23.3929	0.1um	50.00%	7.41%		25.00%	75.00%	50.00%	0.0um	0.7um
Seg.6	0.2um	0.9um	1.0um	0.1um	0.1um	-3.4567	18.5266	0.1um	50.00%	97.86%		25.00%	75.00%	50.00%	0.0um	0.5um
Seg.7																
Seg.8																
Seg.9																
Seg.10																

	Rp	Rv	Rz	Ra	Rq	Rsk	Rku	Rδc	Rmr	Rmr(c)	Comment
Total	2.6um	4.3um	6.9um	0.3um	0.6um	-18.0392	93.4010	0.4um	300.00%	392.68%	
Max.	1.0um	0.9um	1.8um	0.1um	0.1um	-2.4636	23.3929	0.1um	50.00%	97.86%	
Min.	0.1um	0.5um	0.7um	0.0um	0.1um	-3.5015	10.2971	0.1um	50.00%	2.32%	
Ave.	0.4um	0.7um	1.1um	0.1um	0.1um	-3.0065	15.5668	0.1um	50.00%	65.45%	
Std. DV	0.3um	0.1um	0.4um	0.0um	0.0um	0.3950	4.2963	0.0um	0.00%	42.89%	
3sigma	1.0um	0.3um	1.2um	0.0um	0.0um	1.1850	12.8889	0.0um	0.00%	128.66%	

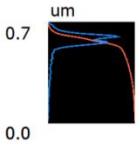

BAC/ADF(#1)

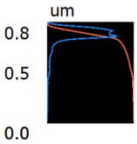

BAC/ADF(#2)

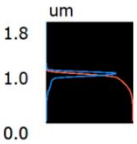

BAC/ADF(#3)

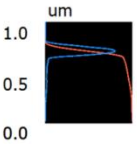

BAC/ADF(#4)

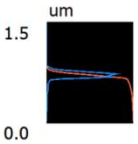

BAC/ADF(#5)

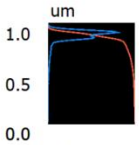

BAC/ADF(#6)

JIS B0601:2001(ISO 4287:1997)
Cutoff : Roughness λs None, λc None

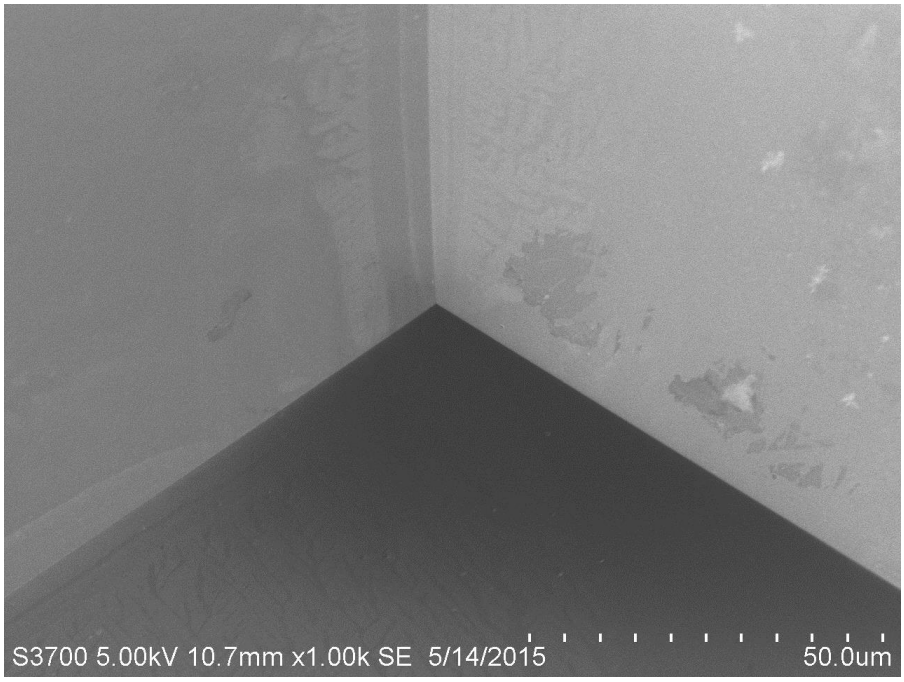

Figure 65: SEM Image of Berkovich Tip

Appendix II: Statistical Data

Response Surface Regression: Contact Depth versus Holding Time, Max Force for 95% Stearate

Model Summary

S	R-sq	R-sq(adj)	R-sq(pred)
27.564	99.55%	99.39%	99.27%

Coded Coefficients

Term	Effect	Coef	SE Coef	T-Value	P-Value	VIF
Constant		1295.4	14.1	91.83	0	
Holding Time	120.27	60.14	8.67	6.93	0	1.01
Max Force	904.28	452.14	8.9	50.81	0	1.16
Holding Time*Holding Time	-47.6	-23.8	16	-1.48	0.16	1.01
Max Force*Max Force	-273.9	-137	13.9	-9.88	0	1
Holding Time*Max Force	5	2.5	11.6	0.22	0.831	1.16

Regression Equation in Uncoded Units

Contact Depth = 265.0 + 0.574 Holding Time + 0.3756 Max Force
- 0.000660 Holding Time*Holding Time - 0.000027 Max Force*Max Force
+ 0.000006 Holding Time*Max Force

Fits and Diagnostics for Unusual Observations

Obs	Contact Depth	Fit	Resid	Std Resid	
3	614.5	665	-50.4	-2.09	R

Response Surface Regression: Modulus versus Holding Time, Max Force for 95% Stearate

Model Summary

S	R-sq	R-sq(adj)	R-sq(pred)
0.182924	64.43%	51.72%	31.73%

Coded Coefficients

Term	Effect	Coef	SE Coef	T-Value	P-Value	VIF
Constant		1.6889	0.0936	18.04	0	
Holding Time	0.2572	0.1286	0.0576	2.23	0.042	1.01
Max Force	0.4732	0.2366	0.0591	4.01	0.001	1.16
Holding Time*Holding Time	-0.148	-0.074	0.106	-0.69	0.499	1.01
Max Force*Max Force	0.2767	0.1384	0.092	1.5	0.155	1
Holding Time*Max Force	0.0332	0.0166	0.0767	0.22	0.832	1.16

Regression Equation in Uncoded Units

Modulus = 1.430 + 0.00141 Holding Time - 0.000081 Max Force
- 0.000002 Holding Time*Holding Time + 0.000000 Max Force*Max Force
+ 0.000000 Holding Time*Max Force

Fits and Diagnostics for Unusual Observations

Obs	Modulus	Fit	Resid	Std Resid	
3	2	1.501	0.499	3.11	R

Response Surface Regression: Hardness versus Holding Time, Max Force for 95% Stearate

Model Summary

S	R-sq	R-sq(adj)	R-sq(pred)
1.5889	89.32%	85.51%	81.08%

Coded Coefficients

Term	Effect	Coef	SE Coef	T-Value	P-Value	VIF
Constant		36.441	0.813	44.81	0	
Holding Time	-7.312	-3.656	0.5	-7.31	0	1.01
Max Force	7.837	3.919	0.513	7.64	0	1.16
Holding Time*Holding Time	3.095	1.547	0.925	1.67	0.117	1.01
Max Force*Max Force	2.228	1.114	0.799	1.39	0.185	1
Holding Time*Max Force	1.757	0.878	0.667	1.32	0.209	1.16

Regression Equation in Uncoded Units

Hardness = 40.44 - 0.0439 Holding Time - 0.00012 Max Force
+ 0.000043 Holding Time*Holding Time + 0.000000 Max Force*Max Force
+ 0.000002 Holding Time*Max Force

Fits and Diagnostics for Unusual Observations

Obs	Hardness	Fit	Resid	Std Resid
3	41	36.78	4.22	3.03

Response Surface Regression: Modulus versus Holding Time, Max Force for 95% Stearate Excluding Outlier

Model Summary

S	R-sq	R-sq(adj)	R-sq(pred)
0.105189	88.14%	83.58%	74.23%

Coded Coefficients

Term	Effect	Coef	SE Coef	T-Value	P-Value	VIF
Constant		1.6702	0.0539	30.96	0	
Holding Time	0.2883	0.1442	0.0332	4.34	0.001	1.01
Max Force	0.5712	0.2856	0.0351	8.13	0	1.12
Holding Time*Holding Time	-0.0423	-0.0211	0.062	-0.34	0.739	1.01
Max Force*Max Force	0.1304	0.0652	0.0546	1.19	0.254	1.01
Holding Time*Max Force	-0.0343	-0.0172	0.0446	-0.39	0.706	1.12

Regression Equation in Uncoded Units

Modulus = 1.181 + 0.001135 Holding Time + 0.000052 Max Force

- 0.000001 Holding Time*Holding Time + 0.000000 Max Force*Max Force
- 0.000000 Holding Time*Max Force

Response Surface Regression: Contact Depth (nm) versus Holding Time (s), Max Force (µN) for 73% Stearate

Model Summary

S	R-sq	R-sq(adj)	R-sq(pred)
21.622	99.70%	99.59%	99.42%

Coded Coefficients

Term	Effect	Coef	SE Coef	T-Value	P-Value	VIF
Constant		1325.9	11.1	119.82	0	
Holding Time (s)	122.57	61.29	6.8	9.01	0	1.01
Max Force (µN)	865.9	432.95	6.98	62.03	0	1.16
Holding Time (s)*Holding Time (s)	-100.6	-50.3	12.6	-4	0.001	1.01
Max Force (µN)*Max Force (µN)	-278.1	-139.1	10.9	-12.78	0	1
Holding Time (s)*Max Force (µN)	30.38	15.19	9.07	1.67	0.116	1.16

Regression Equation in Uncoded Units

Contact Depth (nm) = 305.4 + 0.793 Holding Time (s) + 0.3635 Max Force (µN)
- 0.001394 Holding Time (s)*Holding Time (s) - 0.000027 Max Force (µN)
*Max Force (µN) + 0.000036 Holding Time (s)*Max Force (µN)

Response Surface Regression: Modulus (GPa) versus Holding Time (s), Max Force (μN) for 73% Stearate

Model Summary

S	R-sq	R-sq(adj)	R-sq(pred)
0.040465	87.64%	83.22%	76.61%

Coded Coefficients

Term	Effect	Coef	SE Coef	T-Value	P-Value	VIF
Constant		1.4224	0.0207	68.68	0	
Holding Time (s)	0.1323	0.0662	0.0127	5.2	0	1.01
Max Force (μN)	0.1939	0.0969	0.0131	7.42	0	1.16
Holding Time (s)*Holding Time (s)	-0.0321	-0.0161	0.0236	-0.68	0.506	1.01
Max Force (μN)*Max Force (μN)	-0.0023	-0.0011	0.0204	-0.06	0.957	1
Holding Time (s)*Max Force (μN)	-0.0378	-0.0189	0.017	-1.11	0.285	1.16

Regression Equation in Uncoded Units

Modulus (GPa) = 1.1572 + 0.000679 Holding Time (s) + 0.000054 Max Force (μN)
- 0.000000 Holding Time (s)*Holding Time (s) - 0.000000 Max Force (μN)
*Max Force (μN) - 0.000000 Holding Time (s)*Max Force (μN)

Fits and Diagnostics for Unusual Observations

Obs	Modulus (GPa)	Fit	Resid	Std Resid	
6	1.23	1.3015	-0.0715	-2.03	R

Response Surface Regression: Hardness (MPa) versus Holding Time (s), Max Force (μN) for 73% Stearate

Model Summary

S	R-sq	R-sq(adj)	R-sq(pred)
0.70043	98.58%	98.08%	97.21%

Coded Coefficients

Term	Effect	Coef	SE Coef	T-Value	P-Value	VIF
Constant		34.824	0.358	97.14	0	
Holding Time (s)	-6.963	-3.481	0.22	-15.8	0	1.01
Max Force (μN)	10.852	5.426	0.226	24	0	1.16
Holding Time (s)*Holding Time (s)	6.308	3.154	0.408	7.74	0	1.01
Max Force (μN)*Max Force (μN)	1.057	0.529	0.352	1.5	0.156	1
Holding Time (s)*Max Force (μN)	-0.554	-0.277	0.294	-0.94	0.361	1.16

Regression Equation in Uncoded Units

Hardness (MPa) = 35.348 - 0.05291 Holding Time (s) + 0.001869 Max Force (μN)
+ 0.000087 Holding Time (s)*Holding Time (s) + 0.000000 Max Force (μN)
*Max Force (μN) - 0.000001 Holding Time (s)*Max Force (μN)

Response Surface Regression: Contact Depth (nm) versus Holding Time (s), Max Force (μN) for 56% Stearate

Model Summary

S	R-sq	R-sq(adj)	R-sq(pred)
14.6207	99.88%	99.84%	99.77%

Coded Coefficients

Term			Effect	Coef	SE Coef	T-Value	P-Value	VIF
Constant				1323.51	7.48	176.87	0	
Holding Time (s)			127.6	63.8	4.6	13.87	0	1.01
Max Force (μN)			948	474	4.72	100.43	0	1.16
Holding Time (s)*Holding Time		(s)	-67.34	-33.67	8.51	-3.96	0.001	1.01
Max Force (μN)*Max Force	(μN)		-303.25	-151.62	7.36	-20.61	0	1
Holding Time (s)*Max For	ce (μ	N)	60.76	30.38	6.13	4.95	0	1.16

Regression Equation in Uncoded Units

Contact Depth (nm) = 259.4 + 0.497 Holding Time (s) + 0.39042 Max Force (μN)
- 0.000933 Holding Time (s)*Holding Time (s) - 0.000030 Max Force (μN)
*Max Force (μN) + 0.000071 Holding Time (s)*Max Force (μN)

Fits and Diagnostics for Unusual Observations

Obs	Contact Depth (nm)	Fit	Resid	Std Resid	
17	1580.77	1550.55	30.22	2.4	R

Response Surface Regression: Modulus (GPa) versus Holding Time (s), Max Force (µN) for 56% Stearate

Model Summary

S	R-sq	R-sq(adj)	R-sq(pred)
0.033925	84.21%	78.57%	66.31%

Coded Coefficients

Term	Effect	Coef	SE Coef	T-Value	P-Value	VIF
Constant		1.2505	0.0174	72.02	0	
Holding Time (s)	0.0915	0.0458	0.0107	4.29	0.001	1.01
Max Force (µN)	0.0893	0.0446	0.011	4.08	0.001	1.16
Holding Time (s)*Holding Time (s)	-0.0307	-0.0154	0.0198	-0.78	0.45	1.01
Max Force (µN)*Max Force (µN)	0.1553	0.0776	0.0171	4.55	0	1
Holding Time (s)*Max Force (µN)	-0.0722	-0.0361	0.0142	-2.54	0.024	1.16

Regression Equation in Uncoded Units

Modulus (GPa) = 1.2210 + 0.000694 Holding Time (s) - 0.000062 Max Force (µN)
- 0.000000 Holding Time (s)*Holding Time (s) + 0.000000 Max Force (µN)
*Max Force (µN) - 0.000000 Holding Time (s)*Max Force (µN)

Fits and Diagnostics for Unusual Observations

Obs	Modulus (GPa)	Fit	Resid	Std Resid	
13	1.32	1.2493	0.0707	2.25	R

Response Surface Regression: Hardness (MPa) versus Holding Time (s), Max Force (μN) for 56% Stearate

Model Summary

S	R-sq	R-sq(adj)	R-sq(pred)
0.718137	97.22%	96.22%	94.82%

Coded Coefficients

Term	Effect	Coef	SE Coef	T-Value	P-Value	VIF
Constant		35.029	0.368	95.31	0	
Holding Time (s)	-6.932	-3.466	0.226	-15.34	0	1.01
Max Force (μN)	5.641	2.82	0.232	12.17	0	1.16
Holding Time (s)*Holding Time (s)	4.643	2.322	0.418	5.55	0	1.01
Max Force (μN)*Max Force (μN)	3.623	1.811	0.361	5.01	0	1
Holding Time (s)*Max Force (μN)	-1.834	-0.917	0.301	-3.04	0.009	1.16

Regression Equation in Uncoded Units

Hardness (MPa) = 39.937 - 0.03828 Holding Time (s) - 0.000622 Max Force (μN)

+ 0.000064 Holding Time (s)*Holding Time (s) + 0.000000 Max Force (μN) *Max Force (μN) - 0.000002 Holding Time (s)*Max Force (μN)

Fits and Diagnostics for Unusual Observations

Obs	(MPa)	Fit	Resid	Std	Resid	
6	41.2	39.772	1.428		2.28	R
17	43.1	44.568	-1.468		-2.38	R

Response Surface Regression: Contact Depth (nm) versus Holding Time (s), Max Force (μN) for 53% Stearate

Model Summary

S	R-sq	R-sq(adj)	R-sq(pred)
30.559	99.37%	99.14%	98.01%

Coded Coefficients

Term	Effect	Coef	SE Coef	T-Value	P-Value	VIF
Constant		1217.8	15.6	77.86	0	
Holding Time (s)	125.74	62.87	9.62	6.54	0	1.01
Max Force (μN)	863.67	431.83	9.87	43.77	0	1.16
Holding Time (s)*Holding Time (s)	-35.4	-17.7	17.8	-1	0.337	1.01
Max Force (μN)*Max Force (μN)	-181.8	-90.9	15.4	-5.91	0	1
Holding Time (s)*Max Force (μN)	78.8	39.4	12.8	3.07	0.008	1.16

Regression Equation in Uncoded Units

Contact Depth (nm) = 376.1 + 0.237 Holding Time (s) + 0.2893 Max Force (μN)
- 0.000490 Holding Time (s)*Holding Time (s) - 0.000018 Max Force (μN)
*Max Force (μN) + 0.000092 Holding Time (s)*Max Force (μN

Fits and Diagnostics for Unusual Observations

Obs	Contact Depth (nm)	Fit	Resid	Std Resid	
15	1358.7	1409.9	-51.3	-2.06	R
20	1688.1	1643.3	44.9	2.59	R

Response Surface Regression: Modulus (GPa) versus Holding Time (s), Max Force (μN) for 53% Stearate

Model Summary

S	R-sq	R-sq(adj)	R-sq(pred)
0.05449	82.67%	76.49%	58.41%

Coded Coefficients

Term	Effect	Coef	SE Coef	T-Value	P-Value	VIF
Constant		1.649	0.0279	59.13	0	
Holding Time (s)	0.1388	0.0694	0.0171	4.05	0.001	1.01
Max Force (μN)	0.21	0.105	0.0176	5.97	0	1.16
Holding Time (s)*Holding Time (s)	-0.1215	-0.0607	0.0317	-1.91	0.076	1.01
Max Force (μN)*Max Force (μN)	-0.0765	-0.0382	0.0274	-1.4	0.185	1
Holding Time (s)*Max Force (μN)	-0.0381	-0.019	0.0229	-0.83	0.419	1.16

Regression Equation in Uncoded Units

Modulus (GPa) = 1.2362 + 0.001217 Holding Time (s) + 0.000105 Max Force (μN)
- 0.000002 Holding Time (s)*Holding Time (s) - 0.000000 Max Force (μN)
*Max Force (μN) - 0.000000 Holding Time (s)*Max Force (μN)

Fits and Diagnostics for Unusual Observations

Obs	Modulus (GPa)	Fit	Resid	Std Resid
12	1.49	1.592	-0.102	-2.02

Response Surface Regression: Hardness (MPa) versus Holding Time (s), Max Force (µN) for 53% Stearate

Model Summary

S	R-sq	R-sq(adj)	R-sq(pred)
1.67591	92.99%	90.49%	80.77%

Coded Coefficients

Term	Effect	Coef	SE Coef	T-Value	P-Value	VIF
Constant		40.831	0.858	47.6	0	
Holding Time (s)	-7.838	-3.919	0.527	-7.43	0	1.01
Max Force (µN)	10.166	5.083	0.541	9.39	0	1.16
Holding Time (s)*Holding Time (s)	3.344	1.672	0.976	1.71	0.109	1.01
Max Force (µN)*Max Force (µN)	-3.87	-1.935	0.843	-2.29	0.038	1
Holding Time (s)*Max Force (µN)	-2.992	-1.496	0.703	-2.13	0.052	1.16

Regression Equation in Uncoded Units

Hardness (MPa) = 33.44 - 0.0287 Holding Time (s) + 0.00548 Max Force (µN)
+ 0.000046 Holding Time (s)*Holding Time (s) - 0.000000 Max Force (µN)
*Max Force (µN) - 0.000003 Holding Time (s)*Max Force (µN

Fits and Diagnostics for Unusual Observation

Obs	Hardness (MPa)	Fit	Resid	Std Resid		
20	38.2	40.24	-2.04		-2.14	R

Response Surface Regression: Contact Depth versus Percent ZnSt, Holding Time, Max Force (μN)

Model Summary

S	R-sq	R-sq(adj)	R-sq(pred)
35.6946	99.03%	98.91%	98.74%

Coded Coefficients

Term	Effect	Coef	SE Coef	T-Value	P-Value	VIF
Constant		1317.8	11.4	115.79	0	
Percent ZnSt	24.14	12.07	5.4	2.24	0.029	1.16
Holding Time (s)	123.26	61.63	5.84	10.56	0	1.09
Max Force (μN)	897.42	448.71	5.96	75.3	0	1.24
Percent ZnSt*Percent ZnSt	-71.35	-35.67	9.77	-3.65	0.001	1
Holding Time (s)*Holding Time (s)	-62.8	-31.4	10.4	-3.02	0.004	1.01
Max Force (μN)*Max Force (μN)	-259.28	-129.64	8.98	-14.44	0	1
Percent ZnSt*Holding Time (s)	-3.49	-1.74	7.01	-0.25	0.804	1.24
Percent ZnSt*Max Force (μN)	8.65	4.33	6.73	0.64	0.522	1.08
Holding Time (s)*Max Force (μN)	43.74	21.87	7.49	2.92	0.005	1.16

Regression Equation in Uncoded Units

Contact Depth (nm) = -143 + 12.34 Percent ZnSt + 0.556 Holding Time (s)
+ 0.3484 Max Force (μN) - 0.0809 Percent ZnSt*Percent ZnSt
- 0.000869 Holding Time (s)*Holding Time (s) - 0.000026 Max Force (μN)
*Max Force (μN) - 0.00044 Percent ZnSt*Holding Time (s)
+ 0.000092 Percent ZnSt*Max Force (μN) + 0.000051 Holding Time (s)
*Max Force (μN)

Fits and Diagnostics for Unusual Observations

Obs	Contact Depth (nm)	Fit	Resid	Std Resid	
34	1306.8	1400	-93.2	-2.73	R
35	1358.7	1443.1	-84.4	-2.56	R
57	1580.8	1509.9	70.8	2.08	R

Response Surface Regression: Modulus (GPa versus Percent ZnSt, Holding Time, Max Force (μN)

Model Summary

S	R-sq	R-sq(adj)	R-sq(pred)
0.124978	70.10%	66.20%	62.38%

Coded Coefficients

Term	Effect	Coef	SE Coef	T-Value	P-Value	VIF
Constant		1.3871	0.0399	34.81	0	
Percent ZnSt	0.2299	0.1149	0.0191	6.02	0	1.15
Holding Time (s)	0.1815	0.0908	0.0205	4.43	0	1.1
Max Force (μN)	0.31	0.155	0.0212	7.3	0	1.25
Percent ZnSt*Percent ZnSt	0.4007	0.2004	0.0344	5.83	0	1
Holding Time (s)*Holding Time (s)	-0.0577	-0.0288	0.0365	-0.79	0.432	1.01
Max Force (μN)*Max Force (μN)	0.0532	0.0266	0.0317	0.84	0.404	1
Percent ZnSt*Holding Time (s)	0.0843	0.0422	0.0246	1.71	0.091	1.23
Percent ZnSt*Max Force (μN)	0.1987	0.0993	0.0243	4.09	0	1.11
Holding Time (s)*Max Force (μ N)	-0.0449	-0.0225	0.0263	-0.85	0.396	1.15

Regression Equation in Uncoded Units

Modulus (GPa) = 3.800 - 0.0708 Percent ZnSt + 0.000202 Holding Time (s)
- 0.000110 Max Force (μN) + 0.000454 Percent ZnSt*Percent ZnSt
- 0.000001 Holding Time (s)*Holding Time (s) + 0.000000 Max Force (μN)
*Max Force (μN) + 0.000011 Percent ZnSt*Holding Time (s)
+ 0.000002 Percent ZnSt*Max Force (μN) - 0.000000 Holding Time (s)
*Max Force (μN)

Fits and Diagnostics for Unusual Observations

Obs	Modulus (GPa)	Fit	Resid	Std Resid	
35	1.74	1.5063	0.2337	2.02	R

Response Surface Regression: Hardness (MP versus Percent ZnSt, Holding Time, Max Force (μN)

Model Summary

S	R-sq	R-sq(adj)	R-sq(pred)
1.97699	84.98%	83.04%	80.32%

Coded Coefficients

Term	Effect	Coef	SE Coef	T-Value	P-Value	VIF
Constant		34.999	0.63	55.53	0	
Percent ZnSt	-1.535	-0.767	0.299	-2.57	0.012	1.16
Holding Time (s)	-7.244	-3.622	0.323	-11.21	0	1.09
Max Force (μN)	8.495	4.247	0.33	12.87	0	1.24
Percent ZnSt*Percent ZnSt	4.701	2.351	0.541	4.34	0	1
Holding Time (s)*Holding Time (s)	4.348	2.174	0.575	3.78	0	1.01
Max Force (μN)*Max Force (μN)	0.759	0.38	0.497	0.76	0.448	1
Percent ZnSt*Holding Time (s)	0.076	0.038	0.388	0.1	0.922	1.24
Percent ZnSt*Max Force (μN)	-0.572	-0.286	0.373	-0.77	0.445	1.08
Holding Time (s)*Max Force (μ N)	-0.906	-0.453	0.415	-1.09	0.278	1.16

Regression Equation in Uncoded Units

Hardness (MPa) = 66.18 - 0.808 Percent ZnSt - 0.0416 Holding Time (s)
+ 0.002071 Max Force (μN) + 0.00533 Percent ZnSt*Percent ZnSt
+ 0.000060 Holding Time (s)*Holding Time (s) + 0.000000 Max Force (μN)
*Max Force (μN) + 0.000010 Percent ZnSt*Holding Time (s)
- 0.000006 Percent ZnSt*Max Force (μN) - 0.000001 Holding Time (s)
*Max Force (μN)

Fits and Diagnostics for Unusual Observations

Obs	Hardness (MPa)	Std Fit	Resid	Std Resid		
	3	41	35.542	5.458	3	R
	34	44.4	39.877	4.523	2.39	R
	36	53	49.317	3.683	2.02	R

REFERENCES

1. Kishi, Y., *Lubricant applying device and image forming apparatus*. 2010, Google Patents.
2. Watanabe, K., et al., *Image forming apparatus using a contact or a proximity type of charging system including a protection substance on a moveable body to be charged*. 2008, Google Patents.
3. Nakayama, N., et al., *Analysis of a Blade Cleaning System for Reduction in Wear Rate Variation of the Photoreceptor.* NIP & Digital Fabrication Conference, 2010. **2010**(1): p. 234-237.
4. Molongoski, M. and J. Maher, *Measuring Cleaning Performance in an Electrophotographic Process.* NIP & Digital Fabrication Conference, 1999. **1999**(2): p. 601-603.
5. Deacon, R.F. and J.F. Goodman, *Lubrication by Lamellar Solids.* Proceedings of the Royal Society of London A: Mathematical, Physical and Engineering Sciences, 1958. **243**(1235): p. 464-482.
6. Donnet, C. and A. Erdemir, *Solid Lubricant Coatings: Recent Developments and Future Trends.* Tribology Letters, 2004. **17**(3): p. 389-397.
7. Ali, E., *Solid Lubricants and Self-Lubricating Films*, in *Modern Tribology Handbook, Two Volume Set*. 2000, CRC Press.
8. Bossert, R.G., *The metallic soaps.* Journal of Chemical Education, 1950. **27**(1): p. 10.
9. Robinet, L. and M.-C. Corbeil, *The Characterization of Metal Soaps.* Studies in Conservation, 2003. **48**(1): p. 23-40.

10. Corbeil, M.-C. and L. Robinet, *X-ray powder diffraction data for selected metal soaps.* Powder Diffraction, 2002. **17**(01): p. 52-60.

11. *OTHER APPLICATIONS OF METAL SOAPS.* Industrial Lubrication and Tribology, 1991. **43**(1): p. 3-4.

12. Barman, S. and S. Vasudevan, *Melting of saturated fatty acid zinc soaps.* J Phys Chem B, 2006. **110**(45): p. 22407-14.

13. Vold, R.D. and G.S. Hattiangdi, *Characterization of Heavy Metal Soaps by X-Ray Diffraction.* Industrial & Engineering Chemistry, 1949. **41**(10): p. 2311-2320.

14. Whitmore, W.F. and M. Lauro, *Metallic Soaps—Their Uses, Preparation, and Properties.* Industrial & Engineering Chemistry, 1930. **22**(6): p. 646-649.

15. Gönen, M., et al., *Zinc Stearate Production by Precipitation and Fusion Processes.* Industrial & Engineering Chemistry Research, 2005. **44**(6): p. 1627-1633.

16. Barman, S. and S. Vasudevan, *Mixed saturated-unsaturated alkyl-chain assemblies: solid solutions of zinc stearate and zinc oleate.* J Phys Chem B, 2007. **111**(19): p. 5212-7.

17. Sawada, K. and M. Konaka, *Characterization of Fine Metallic Soap Particles by X-Ray Diffraction, Differential Scanning Calorimetry, and Specific Surface Area Analysis.* Journal of Oleo Science, 2004. **53**(12): p. 627-640.

18. Ishioka, T., A. Kiritani, and T. Kojima, *Infrared study on annealing effect on conformation of zinc stearate.* Spectrochimica Acta Part A: Molecular and Biomolecular Spectroscopy, 2007. **66**(4–5): p. 1048-1051.

19. Stachowiak, G.W. and A.W. Batchelor, *Engineering tribology*. 4. ed. 2014, Amsterdam u.a.: Butterworth-Heinemann. XXVIII, 852 S.

20. Stachowiak, G.W. and A.W. Batchelor, *4 - Hydrodynamic Lubrication*, in *Engineering Tribology (Third Edition)*, G.W.S.W. Batchelor, Editor. 2006, Butterworth-Heinemann: Burlington. p. 103-204.

21. Clauss, F.J., *Solid Lubricants and Self-Lubricating Solids*. 1972, Elsevier Science: Burlington. p. 1 online resource (279 pages).

22. van Geffen, V., *A study of friction models and friction compensation.* DCT, 2009. **118**: p. 24.

23. Dickson, P., *Friction,* in *Shock Wave Science and Technology Reference Library, Vol. 5*, B.W. Asay, Editor. 2010, Springer Berlin Heidelberg. p. 537-554.

24. Matsuo, Y., D. Clarke, and S. Ozeki, *Friction*, in *Phenolic Resins: A Century of Progress*, L. Pilato, Editor. 2010, Springer Berlin Heidelberg. p. 345-361.

25. Popov, V., *Contact mechanics and friction: physical principles and applications*. 2010: Springer Science & Business Media.

26. Carkner, C., *Modeling Friction, Wear and Lubrication of Sliding Polyurethane and Polycarbonate Surfaces Representing Printer Components with Molecular Dynamics.* 2013.

27. Amiri, M. and M.M. Khonsari, *On the Thermodynamics of Friction and Wear—A Review.* Entropy, 2010. **12**(5): p. 1021-1049.

28. Smart, R.F. and J.C. Moore, *Materials selection for wear resistance.* Wear, 1979. **56**(1): p. 55-67.

29. Persson, B.J., *Contact Mechanics for Randomly Rough Surfaces: On the Validity of the Method of Reduction of Dimensionality.* Tribology Letters, 2015. **58**(1): p. 1-4.

30. Greenwood, J.A. and J.B.P. Williamson, *Contact of Nominally Flat Surfaces.* Proceedings of the Royal Society of London A: Mathematical, Physical and Engineering Sciences, 1966. **295**(1442): p. 300-319.

31. Bush, A.W., R.D. Gibson, and T.R. Thomas, *The elastic contact of a rough surface.* Wear, 1975. **35**(1): p. 87-111.

32. Fischer-Cripps, A.C. and I. Mustafaev, *Introduction to contact mechanics*. 2000: Springer.

33. Li, X. and B. Bhushan, *A review of nanoindentation continuous stiffness measurement technique and its applications.* Materials characterization, 2002. **48**(1): p. 11-36.

34. Fischer-Cripps, A.C., *Nanoindentation*. 2011: Springer Science & Business Media.

35. Feng, G. and A.H.W. Ngan, *Effects of Creep and Thermal Drift on Modulus Measurement Using Depth-sensing Indentation.* Journal of Materials Research, 2002. **17**(03): p. 660-668.

36. Bennett, J., *Characterization of Surface Roughness*, in *Light Scattering and Nanoscale Surface Roughness*, A. Maradudin, Editor. 2007, Springer US. p. 1-33.

37. Luk, F., V. Huynh, and W. North, *Measurement of surface roughness by a machine vision system.* Journal of physics E: Scientific instruments, 1989. **22**(12): p. 977.

38. Whitehouse, D.J., *Surface metrology.* Measurement Science and Technology, 1997. **8**(9): p. 955.

39. West, P.E., *Introduction to Atomic Force Microscopy: Theory, Practice, Applications*. 2006: P. West.

40. Podgorkov, V., O. Drobysheva, and V. Semenov, *Measuring the surface roughness of soft metals.* Measurement Techniques, 1973. **16**(7): p. 1070-1070.

41. Al-Nawas, B., et al., *Validation of three-dimensional surface characterising methods: scanning electron microscopy and confocal laser scanning microscopy.* Scanning, 2001. **23**(4): p. 227-31.

42. Paddock, S.W., *Confocal laser scanning microscopy.* Biotechniques, 1999. **27**: p. 992-1007.

43. Conroy, M. and J. Armstrong. *A comparison of surface metrology techniques*. in *Journal of Physics: Conference Series*. 2005. IOP Publishing.

44. Leach, R., *Optical measurement of surface topography*. 2011: Springer.

45. Amaral, M.M., et al. *Roughness measurement methodology according to DIN 4768 using optical coherence tomography (OCT)*. in *SPIE Europe Optical Metrology*. 2009. International Society for Optics and Photonics.

46. Menčík, J., *Uncertainties and errors in nanoindentation.* Nanoindentation in Materials Science, InTech, Rijeka, 2012: p. 53-86.

47. Byakova, A., S. Gnyloskurenko, and T. Nakamura, *The role of foaming agent and processing route in the mechanical performance of fabricated aluminum foams.* Metals, 2012. **2**(2): p. 95-112.

VITA

The author, George A. Nimick, attended Florida State University (FSU) where he completed a Bachelor of Science in Mechanical Engineering. Following the completion the completion of this degree, he attended the University of Kentucky (UK) to pursue a Master of Science in Material Science and Engineering while working part time at Lexmark International, Inc. The topic for this thesis was industry inspired through Lexmark in conjunction with UK to investigate an industry related topic while satisfying the requirements for the degree.